Fall 2011

Multimodal 3-D segmentation of optic nerve head structures from spectral domain Oct volumes and color fundus photographs

Zhihong Hu
University of Iowa

MULTIMODAL 3-D SEGMENTATION OF OPTIC NERVE HEAD STRUCTURES FROM SPECTRAL DOMAIN OCT VOLUMES AND COLOR FUNDUS PHOTOGRAPHS

by

Zhihong Hu

An Abstract

Of a thesis submitted in partial fulfillment of the
requirements for the Doctor of Philosophy degree
in Electrical and Computer Engineering
in the Graduate College of
The University of Iowa

December 2011

Thesis Supervisor: Assistant Professor Mona K. Garvin

ABSTRACT

Standard structural methods for the assessment of glaucoma, such as the planimetry of stereo color photographs of the optic disc, involve a subjective component either by the patient or examiner and suffer from poor reproducibility. Spectral-domain optical coherence tomography (SD-OCT) provides a 3-D, cross-sectional, microscale depiction of biological tissues. Given the wealth of volumetric information at microscale resolution available with SD-OCT volumes of the back of the eye, it is likely that better parameters can be obtained for measuring glaucoma changes that move beyond what is possible using fundus photography.

The neural canal opening (NCO) is a 3-D single anatomic structure in SD-OCT volumes. It is proposed as a basis for a stable reference plane from which various optic nerve morphometric parameters can be derived. The overall aim of this Ph.D. project is to develop a framework to segment the 3-D NCO and retinal vessels using information from SD-OCT volumes and fundus photographs to aid in the management of glaucoma.

Based on the mutual positional relationship of the NCO and vessels, a multimodal 3-D scale-learning-based framework is developed to iteratively identify these structures in SD-OCT volumes by incorporating each other's pre-identified positional information. The algorithm first applies a 3-D wavelet-transform-learning-based layer segmentation and pre-segments the NCO using a graph-theoretic approach. To improve the NCO segmentation, the vessels are identified either using an OCT vessel segmentation approach by incorporating the pre-segmented NCO positional informa-

tion to the vessel classification or a multimodal concurrent classification approach by combining the complementary features from SD-OCT volumes and fundus photographs (or a registered-fundus approach based on the original fundus vessel segmentation). The obtained vessel positional information is then used to help enhance the NCO segmentation by incorporating this information in the cost function of graph search.

The major contributions of this work include: 1) extending the 3-D graph-based segmentation to the use of 3-D scale-learning-based cost function, 2) developing a graph theoretic approach for segmenting the NCO in SD-OCT volumes, 3) developing a 3-D wavelet-transform-learning-based graph theoretic approach for segmenting the NCO in SD-OCT volumes by iteratively utilizing the pre-identified NCO and vessel positional information, 4) developing a vessel classification approach in SD-OCT volumes by incorporating the pre-segmented NCO positional information to the vessel classification to suppress the NCO false positives, and 5) developing a multimodal concurrent classification and a registered-fundus approach for better identifying vessels in SD-OCT volumes using additional fundus information.

Abstract Approved: _____

Thesis Supervisor

_____

Title and Department

_____

Date

MULTIMODAL 3-D SEGMENTATION OF OPTIC NERVE HEAD STRUCTURES FROM SPECTRAL DOMAIN OCT VOLUMES AND COLOR FUNDUS PHOTOGRAPHS

by

Zhihong Hu

A thesis submitted in partial fulfillment of the
requirements for the Doctor of Philosophy degree
in Electrical and Computer Engineering
in the Graduate College of
The University of Iowa

December 2011

Thesis Supervisor: Assistant Professor Mona K. Garvin

Graduate College
The University of Iowa
Iowa City, Iowa

CERTIFICATE OF APPROVAL

PH.D. THESIS

This is to certify that the Ph.D. thesis of

Zhihong Hu

has been approved by the Examining Committee for the thesis requirement for the Doctor of Philosophy degree in Electrical and Computer Engineering at the December 2011 graduation.

Thesis Committee: _____
Mona K. Garvin, Thesis Supervisor

_____
Michael D. Abràmoff

_____
Joseph M. Reinhardt

_____
Milan Sonka

_____
Xiaodong Wu

ACKNOWLEDGEMENTS

I would like to thank my adviser, Dr. Mona K. Garvin, for the guidance and support throughout this work and also appreciate her carefulness for editing my papers; thank Dr. Milan Sonka for bringing me to the field of the medical image processing and also appreciate his teaching and discussions in the class of Advanced Digital Image Processing and in this work; thank Dr. Michael D. Abràmoff for his enthusiastic and informative discussions and significant help both in image processing and in ophthalmology and also appreciate his help for the ground truth of the vessel segmentation; and thank Dr. Young H. Kwon for his great interest and informative discussions especially related to the ophthalmology and also appreciate his help for the ground truth of the NCO segmentation of human subjects.

Special thanks go to Dr. Meindert Niemeijer for the discussions in retinal vessel segmentation and for providing the vessel segmentation results of fundus photographs; go to Dr. Gwénolé Quellec for the discussions and providing the original code of wavelet transform; go to Dr. Kyungmoo Lee for providing the layer segmentation of human scans and the 3-D OCT viewer; go to Qi Song, Dr. Yin Yin, and Shanhui Sun for the discussions and providing the original graph search libraries etc.

I would like to thank Dr. Xiaodong Wu for the teaching of Graph Algorithm and Combinatorial Optimization and the help when I served as his Teaching Assistant in that class; thank Dr. Joseph M. Reinhardt and Dr. Hans J. Johnson for the teaching of Multi-Dimensional Medical Imaging Process; thank Dr. Punam K. Saha for the teaching of Pattern Recognition; and thank all other related teachers. I also would like

to give my sincere thanks to Dr. Karl E. Lonngren for providing me the opportunity working on the solution manual of his text book. I am deeply moved by his humorous and optimistic attitude to everything.

I would appreciate our department secretary Catherine Kern and the administrative assistant Dina Blanc for setting up the paper work and their patient assistance; appreciate Dr. Sudhakar M. Reddy and Dr. Jon G. Kuhl for their teaching and help as the graduate student advisor; appreciate Travis Wendling and other CSS stuffs for their support and maintenance of the computer; and appreciate all our labmates Bhavna Antony, Qiao Hu, Jui-Kai Wang, Mohammad S. Miri, Dr. Li Tang etc., for their friendship.

Sincere thanks go to Dr. Claude F. Burgoyne, Dr. Hongli Yang, Dr. Nicholas G. Strouthidis, and their other colleagues from Devers Eye Institute for providing the SD-OCT data and manual tracings of non-human primate eyes and for the discussions about the neural canal opening; go to Mari Long for the help of acquiring the glaucoma SD-OCT data of human scans; go to our funding support of NIH grant EY018853, RPB, Department of Veterans Affairs, Marlene S. and Leonard A. Hadley Glaucoma Research Fund, and AGS Mid-Career Physician Scientist Award etc.

Deep thanks go to my parents, brother, sister, and all the family in China for their understanding for me to pursuit the Ph.D. study; go to my husband for his encouragement; and more importantly, go to my intelligent and cute son for his wonderful mental support.

ABSTRACT

Standard structural methods for the assessment of glaucoma, such as the planimetry of stereo color photographs of the optic disc, involve a subjective component either by the patient or examiner and suffer from poor reproducibility. Spectral-domain optical coherence tomography (SD-OCT) provides a 3-D, cross-sectional, microscale depiction of biological tissues. Given the wealth of volumetric information at microscale resolution available with SD-OCT volumes of the back of the eye, it is likely that better parameters can be obtained for measuring glaucoma changes that move beyond what is possible using fundus photography.

The neural canal opening (NCO) is a 3-D single anatomic structure in SD-OCT volumes. It is proposed as a basis for a stable reference plane from which various optic nerve morphometric parameters can be derived. The overall aim of this Ph.D. project is to develop a framework to segment the 3-D NCO and retinal vessels using information from SD-OCT volumes and fundus photographs to aid in the management of glaucoma.

Based on the mutual positional relationship of the NCO and vessels, a multimodal 3-D scale-learning-based framework is developed to iteratively identify these structures in SD-OCT volumes by incorporating each other's pre-identified positional information. The algorithm first applies a 3-D wavelet-transform-learning-based layer segmentation and pre-segments the NCO using a graph-theoretic approach. To improve the NCO segmentation, the vessels are identified either using an OCT vessel segmentation approach by incorporating the pre-segmented NCO positional information to the vessel classification or a multimodal concurrent classification approach

by combining the complementary features from SD-OCT volumes and fundus photographs (or a registered-fundus approach based on the original fundus vessel segmentation). The obtained vessel positional information is then used to help enhance the NCO segmentation by incorporating this information in the cost function of graph search.

The major contributions of this work include: 1) extending the 3-D graph-based segmentation to the use of 3-D scale-learning-based cost function, 2) developing a graph theoretic approach for segmenting the NCO in SD-OCT volumes, 3) developing a 3-D wavelet-transform-learning-based graph theoretic approach for segmenting the NCO in SD-OCT volumes by iteratively utilizing the pre-identified NCO and vessel positional information, 4) developing a vessel classification approach in SD-OCT volumes by incorporating the pre-segmented NCO positional information to the vessel classification to suppress the NCO false positives, and 5) developing a multimodal concurrent classification and a registered-fundus approach for better identifying vessels in SD-OCT volumes using additional fundus information.

TABLE OF CONTENTS

LIST OF TABLES

Table

LIST OF FIGURES

Figure

CHAPTER 1
INTRODUCTION

Glaucoma is the second most common cause of blindness worldwide [1]. It is historically accepted that the glaucomatous change of the clinically visible optic disc margin, i.e. the clinical optic cupping, results from the degeneration of the retinal ganglion cell axons [2,3] in the optic nerve head (ONH) and may result in increasing visual field (VF) loss and eventual irreversible blindness.

The risk of visual loss due to glaucoma can be minimized by early diagnosis and careful monitoring of disease progression in the ONH. However, the latter requires a reproducible measurement of the disease state. Currently available methods such as the planimetry based on stereo disc photographs, on one hand, involve a subjective component either by the patient or examiner and on the other hand, a few anatomic structures might overlap together on the essential 2-D images. For instance, we and others [4, 5] recently found that the clinical optic disc margin seen on fundus photographs may consist of a few anatomic structures, i.e. the neural canal opening (NCO), border tissue, and/or the anterior scleral canal opening, which can decrease reproducibility [6, 7].

Spectral-domain optical coherence tomography (SD-OCT) is a noncontact, non-invasive imaging technique used to obtain high resolution 3-D images of the retina or ONH [8]. It is a powerful modality to qualitatively assess retinal and ONH features and pathologies. Given the wealth of volumetric information at microscale resolution available with SD-OCT, it is likely that better parameters can be obtained for measuring glaucomatous change that move beyond what is possible using stereo fundus

photography alone. However, it is currently unclear which ONH parameters derived from SD-OCT can be best used to quantify glaucomatous changes.

Thus, the overall aim of this Ph.D. project is to develop novel algorithms using the information from SD-OCT volumes and color fundus photographs to help detect and analyze multiple 3-D structures with mutual positional relationship in SD-OCT volumes to help the management of glaucoma progression.

A central requirement for the detection of the ONH structural change is a longitudinally stable zero reference plane [4]. The NCO is a three-dimensional anatomic structure in the ONH and is discernible and delineable in SD-OCT volumes. It is assumed stable during glaucoma progression and could be used as a basis for a stable reference plane [4,5], from which various optic nerve morphometric parameters can be derived. Thus, the core hypothesis motivating this study is that the segmentation of the 3-D NCO will enable more reproducible and objective glaucomatous parameters than what is currently possible from manual planimetry alone (even using a consensus of glaucoma experts).

Due to the crossing of the retinal vessels with the NCO in the ONH, it causes the NCO segmentation difficulty in some cases. We thus segment vessels to aid a better NCO segmentation. In addition, the segmentation of retinal vessels in SD-OCT volumes could lead to a more objective diagnosis of diseases and could be used for other applications such as OCT-to-OCT and OCT-to-fundus registration.

Based on the mutual positional relationship of the NCO and retinal vessels, a multimodal 3-D scale-learning-based framework is developed to iteratively identify these structures by incorporating the pre-identified NCO positional information in the

vessel classification and incorporating the pre-identified vessel positional information to the cost function of the final segmentation of the NCO. Fig. 1.1 is an overview of this framework.

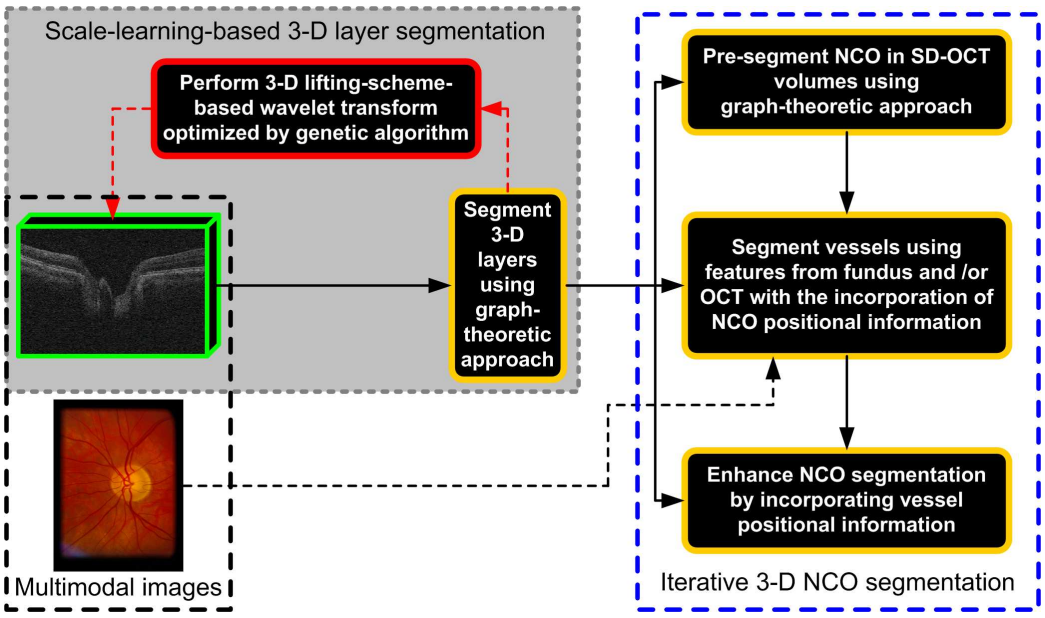

Figure 1.1: Overall framework of this Ph.D. project.

More specifically, a graph theoretic approach is applied to segment the 3-D retinal layers using the 3-D lifting-scheme-wavelet-transform-learning-based cost function. The NCO is then pre-segmented using a graph search approach. To help refine the NCO segmentation, we present three novel options for segmenting the retinal vessels: 1) a single modal OCT vessel segmentation approach by incorporating the pre-segmented NCO positional information to the vessel classification to suppress the NCO false positives, 2) a NCO-false-positive-suppression-based multimodal vessel segmentation approach based on the complementary features from SD-OCT volumes

and color fundus photographs, and 3) a registered-fundus vessel segmentation approach based on the original fundus vessel segmentation being registered to the OCT space. The obtained vessel positional information is then used to help enhance the NCO segmentation by incorporating this information in the cost function design for segmenting the NCO.

Note that the 3-D wavelet transform via lifting scheme has been recently reported by Quellec *et al.* [9] with the strong motivation to help remove high frequency noise and extract texture properties. The graph search approach aiming to find the optimal solution of single surface was initially reported by Wu and Chen [10]. Li *et al.* [11] extended it for finding the optimal solution of multiple surfaces in a low-polynomial time using edge information, and Garvin *et al.* [12] extended it using additionally regional information. In this work, the use of the 3-D wavelet-transform-learning-based cost function for the graph search reflects an extension in cost function design.

Thus in this work, in addition to the significance of the detection and analysis of the NCO and vessels to the ophthalmic community, the general image processing community will be interested in 1) the use of the scale-learning-based cost function for the graph-based 3-D layer segmentation, 2) the incorporation of the pre-segmented structures' positional information in the classification process (such as the positional information from the pre-segmented NCO) and in the cost function for use in the graph-based segmentation (such as the positional information from pre-segmented vessels), and 3) the multimodal concurrent classification by combining the complementary information from different modalities (such as SD-OCT volumes and color fundus photographs).

1.1 Specific aims

In particular, this work includes the following specific aims:

- **Aim 1:** Develop and validate a NCO segmentation approach using a graph theoretic approach with the application in SD-OCT volumes of human eyes.
- **Aim 2:** Develop and validate a 3-D wavelet-transform-learning-based graph theoretic approach for segmenting the NCO by iteratively using the pre-identified NCO and vessel positional information (from aim 3 or 4) with the application in SD-OCT volumes of non-human primate eyes.
- **Aim 3:** Develop and validate a single modal classification approach for identifying vessels in SD-OCT volumes by incorporating the pre-segmented NCO positional information to the vessel classification to suppress the NCO false positives.
- **Aim 4:** Develop and validate a NCO-false-positive-suppression-based multimodal concurrent classification and a registered-fundus approach for better identifying retinal vessels in SD-OCT volumes using additional fundus information.

1.2 Thesis overview

This dissertation is divided into 8 chapters including a general introduction in this chapter. An overview of each of the remaining chapters is as follows:

- Chapter 2 provides the overall clinical background and significance of this project, including an introduction of the stereo color photography and opti-

cal coherence tomography, glaucoma and glaucomatous structures, clinical optic disc margin and neural canal opening, and current clinical management of glaucoma.

- Chapter 3 provides an overview of the prior techniques related to the NCO/clinical optic disc margin and retinal vessel segmentation in SD-OCT volumes and color fundus photographs. A brief introduction of our initial graph-theoretic and 3-D wavelet-transform-learning-based NCO segmentation approaches and our single modal OCT, registered-fundus, and multimodal vessel segmentation approaches are also provided.
- Chapter 4 presents the algorithm details and results of our initial graph-theoretic NCO segmentation with the application in SD-OCT volumes of human eyes.
- Chapter 5 presents the algorithm details and results of our 3-D wavelet-transform-learning-based NCO segmentation with the application in SD-OCT volumes of non-human primate eyes.
- Chapter 6 presents the algorithm details and results of our single modal vessel segmentation in SD-OCT volumes.
- Chapter 7 presents the algorithm details, results of our registered-fundus and multimodal vessel segmentation in color fundus photographs and/or SD-OCT volumes and the comparison with two closest previous OCT vessel segmentation approaches (including our single modal OCT approach).
- Chapter 8 concludes this Ph.D. project and discusses some potential future directions.

CHAPTER 2
CLINICAL BACKGROUND AND SIGNIFICANCE

This chapter provides an overall introduction of the clinical background of this Ph.D. project. Section 2.1 introduces the anatomy of eye and optic nerve; Section 2.2 is an introduction of the stereo color photography and optical coherence tomography; Section 2.3 introduces the glaucoma and glaucomatous structures; Section 2.4 is an introduction of clinical optic disc margin and neural canal opening; and Section 2.5 briefly introduces the current clinical management of glaucoma.

2.1 Anatomy of eye and optic nerve

The eye is like a camera. Light enters the eye through a small hole, i.e. the pupil and is focused on the retina by the lens of the eye. The retina is the light-sensitive tissue consisting of several layers at the back of the eye. The layer of photoreceptors (rods and cones) of the retina absorbs the light and converts the light signal into the neural signal and the neural signal is transmitted to retinal ganglion cells (axons). The more than 1 million ganglion cell axons converge at the optic nerve head (ONH) and exit the eye through the neural canal opening, anterior (inner), and posterior (outer) scleral canal openings [13].

The ONH is a 3-D structure characterized by a peripheral "neuroretinal rim" formed by the nerve fibers and astrocytes and a central depression without nerve fibers called the "optic cup" or "excavation" consisting of supporting tissue [14]. There are no photoreceptors in the ONH and it cannot respond to light stimulation. The ONH is also known as the blind spot.

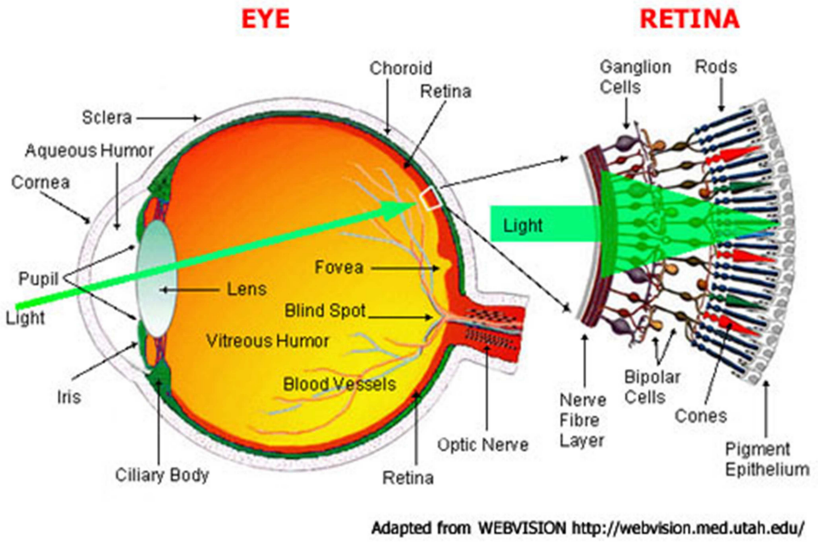

Figure 2.1: Schematic illustration of the cross sectional view of the right human eye with a highlight of retina. Copied with permission from http://www.astrosurf.com/re/eyepieces.html.

Within the scleral portion of the canal, the bundled axons (the nerve fibers) pass through the poles of the lamina cribrosa, a 3-D mesh-like structure in the ONH, and eventually connect to the visual cortex, the visual center of the brain where the brain processes and interprets the visual information. The lamina cribrosa is also a passage of the blood vessels. Fig. 2.1 and 2.2 are the schematic illustrations of the anatomy of human eye and optic nerve head respectively.

2.2 Stereo color photography and optical coherence tomography

Stereo color photography is a photographic technique to acquire stereo color photographs of the ONH. It is essentially a 2-D imaging technique and remains the most widely used approach for the ONH imaging due to the relatively less expensive price.

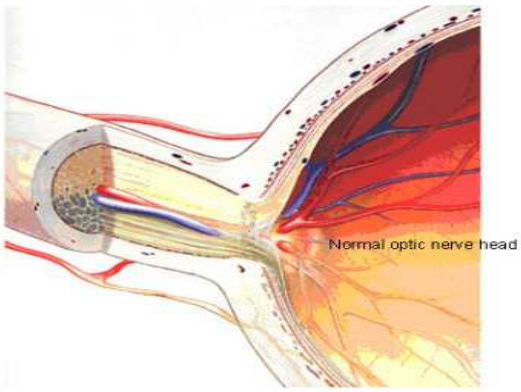

Figure 2.2: Illustration of the optic nerve head. Images courtesy of pharmainfo.net.

Optical coherence tomography (OCT) is a relatively new modality which provides a 3-D, cross-sectional, microscale depiction of the optical reflectance properties of biological tissues [8]. It is a powerful modality to qualitatively assess retinal and ONH features and pathologies.

OCT is an interference-based imaging technique. There are in general two types of OCT, time-domain (TD) and spectral-domain OCT (SD-OCT) [15]. Both of them utilize the low-coherence broadband light sources with the central wavelength range of 800 nm to 1100 nm approximately. It is the broadband light sources that result in the high resolution of the OCT volumes that makes the OCT attractive.

Recall that the axial spatial resolution of the SD-OCT can be defined as [15]:

$$\Delta z = \frac{\lambda_0^2}{2n\Delta\lambda} \tag{2.1}$$

where n is the refractive index of the tissue sample, λ_0 is the central wavelength of the light source, and $\Delta\lambda$ is the bandwidth at full width half maximum (FWHM).

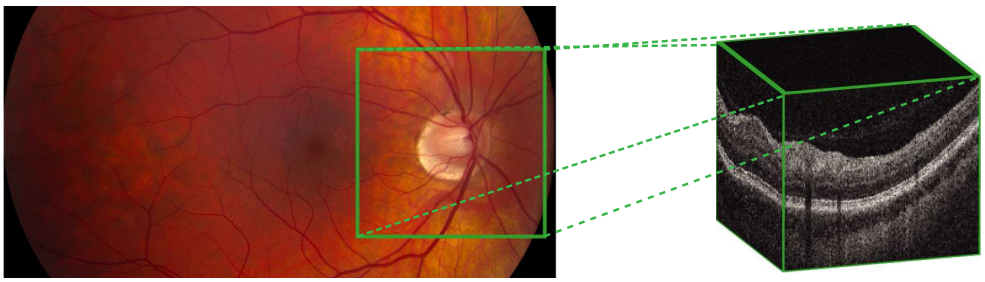

Figure 2.3: Typical region of the ONH in color fundus photograph and SD-OCT volume. Left image: color fundus photograph with a bounding box (green) of the ONH. Right image: the corresponding schematic SD-OCT volume (size $6 \times 6 \times 2$ mm^3) centered at the ONH of the human eye.

Thus, the broader and/or shorter the wavelength of light source, the higher the axial spatial resolution.

The SD-OCT is of special interest over TD-OCT in that it can directly access the spectrum and does not need the mechanical scanning. It hence provides a fast acquisition of the three-dimensional images of interest. Currently, the SD-OCT at the central wavelength of 800 nm range is commonly used in ophthalmology to image and visualize the three-dimensional ONH structure. Fig. 2.3 shows the typical region of the ONH in color fundus photographs and the corresponding schematic SD-OCT volume using a SD-OCT at the central wavelength of 800 nm range. A few example slices of the SD-OCT volume from a human eye are provided in Fig. 2.4.

However, the central wavelengths around 800nm are not the most suitable light source range for opthalmic imaging. This is due to the fact of the highly scattering and absorption of the retinal pigment epithelium (RPE) at shorter wavelengths, reducing the penetration depth. The selection of the central wavelength must be accorded with the application, where scattering and absorption losses should be considered,

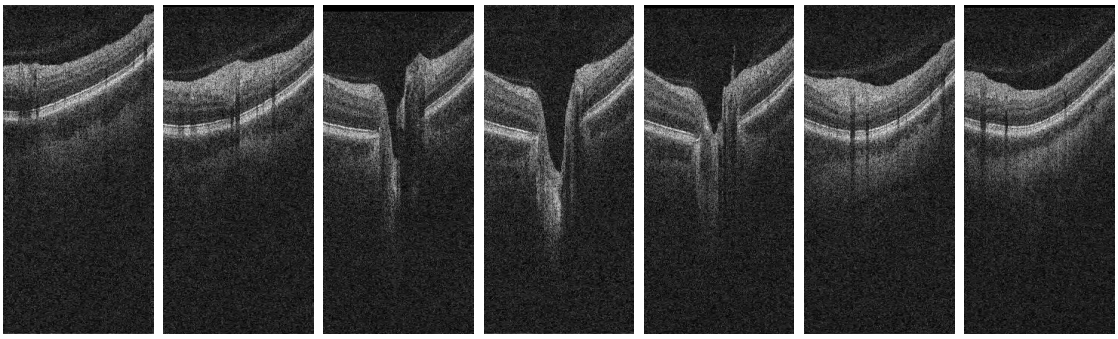

(a) Slice 0 (b) Slice 55 (c) Slice 88 (d) Slice 99 (e) Slice 110 (f) Slice 165 (g) Slice 198

Figure 2.4: Example slices from ONH-centered SD-OCT volume of human eye.

especially when the axial penetration depth is of importance. It has been reported that the central wavelengths in the 1-1.1 μm range demonstrate a deeper penetration into the choroid below the RPE [16], making the SD-OCT more attractive for looking into the deeper structure of the intraocular and further help the detection and follow-up treatment of the retinal and optic nerve pathologies.

2.3 Glaucoma and glaucomatous structures

Glaucoma is a chronic optic neurodegenerative disease of the optic nerve that, if left untreated, may result in increasing visual field (VF) loss and blindness. It is characterized by the progressive damage of retinal nerve cells, nerve fibers, and astrocytes [14]. The clinical optic cup enlarging (optic cupping) and neuroretinal rim thinning resulted from the degeneration of the retinal ganglion cell axons [2, 3] are typical indication of glaucoma progression. Fig. 2.5 is a schematic illustration of the optic cupping in the color fundus photographs. A schematic illustration of the view of the glaucoma patient at different glaucoma stages is shown in Fig. 2.6.

However, glaucomatous cupping in the ONH is a complex phenomenon. It does

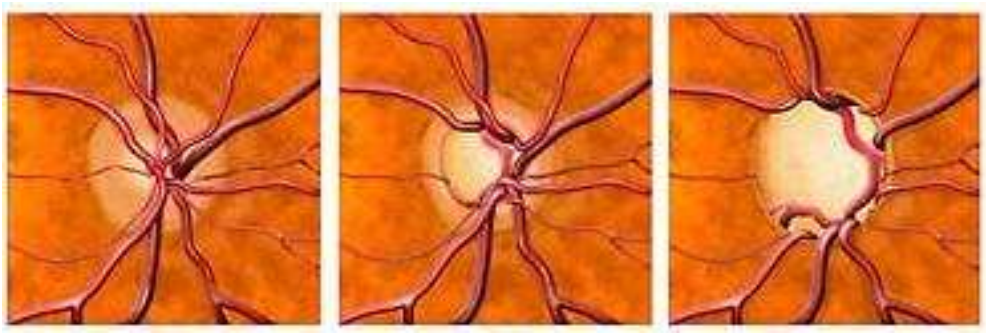

Figure 2.5: Schematic illustration of optic cupping. Left: normal eye, middle: moderate glaucoma, and right: advanced glaucoma. Images courtesy of Macula Center (http://www.maculacenter.com).

(a) (b) (c)

Figure 2.6: View of glaucoma patient with (a) normal eye, (b) moderate glaucoma, and (c) advanced glaucoma. Images courtesy of Eye Scan (http://www.eyescan.com.au).

not just involve axonal damage but also connective-tissue damage, although the axonal damage is likely the central factor of the vision loss of glaucoma. Yang *et al.* [17] has recently proposed that the glaucomatous cupping is resulted from two principal pathophysiologic phenomena: 1) prelaminar thinning, which results in a clinically shallow cupping from the loss of all forms of ganglion cell axons (corresponding to clinical optic cupping) and 2) laminar deformation, which results in a clinically deeper

cupping from the damage of the lamina cribrosa (LC), scleral flange, and peripapillary scleral connective tissues.

It is reported that the glaucomatous change is also involved in the blood vessels' changes [18]. With the diminishing visibility of the retinal nerve fiber layer, the decrease of the rim area, and the increase of the visual field defects in the glaucoma subjects, the diameters of the blood vessels have the tendency of narrowing and present larger variations over those of the normal subjects [18].

2.4 Clinical optic disc margin and neural canal opening

The clinical optic disc margin commonly refers to the clinically visible boundary of neural tissue within the optic nerve head on color fundus photographs. The change of the clinically visible optic disc margin has been historically utilized to help diagnose the presence and progression of glaucoma. However, as mentioned in Chapter 1, we recently found that the optic disc margin does not overlap with a single constant anatomic structure in volumetric SD-OCT, consistent with the recent comparison of clinical and SD-OCT optic disc margin anatomy by Strouthidis *et al.* [4, 5].

The neural canal opening (NCO) is a 3-D anatomic structure, through which and the scleral canal openings, the ganglion cell axons exit the eye. It is defined as the termination of the RPE/Bruch's membrane (BM) complex and the entrance to the neural canal at the level of the RPE and BM [4,5]. The NCO partially corresponds to the clinical optic disc margin and is indiscernible or only partially discernible in color fundus photographs. However, Strouthidis *et al.* [4] proposed that there is always a discernible NCO in SD-OCT volumes. The NCO is assumed a stable structure and

is not likely to change substantially with glaucomatous progression.

2.5 Current clinical management of glaucoma

Currently available methods to aid in the management of glaucoma include visual field tests, optic nerve planimetry based on stereo disc photographs, optic nerve head tomography using the Heidelberg Retina Tomograph (HRT), and peripapillary nerve fiber layer thickness analysis (using polarimetry or OCT) [6, 7, 19, 20]. Many of these modalities involve a subjective component either by the patient or examiner, which can decrease reproducibility. The optic nerve planimetry based on stereo disc photographs is the gold standard for diagnosis and treatment follow-up of glaucoma [19]. However, we and others have previously shown that manual planimetry is time-consuming and introduces substantial inter-observer variability due to the need for human interpretation [6, 7].

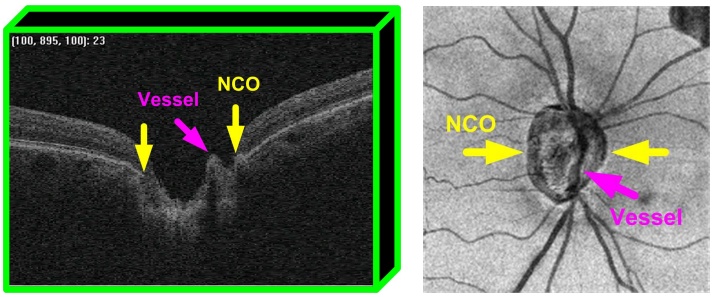

(a) (b)

Figure 2.7: Illustration of the NCO and retinal vessels. (a) Central SD-OCT slice and (b) SD-OCT projection image from glaucoma subject with the highlight of NCO (yellow arrows) and blood vessels (pink arrows) respectively.

Since the stability of the NCO during the glaucomatous progression, the identi-

fication of the NCO-based structures are expected to enable more reproducible and objective glaucomatous parameters. Note that the retinal vessels typically cross over with the NCO boundary in the SD-OCT projection images, causing the difficulty of the NCO detection in some cases. To help better identify the NCO, we also identify retinal vessels. Fig. 2.7 is an example illustration of the NCO and blood vessels in the central slice of a SD-OCT volume from a glaucoma subject. A brief overview of the technical background of the prior NCO and vessel segmentation and our developed approaches are provided in the next chapter.

CHAPTER 3
TECHNICAL BACKGROUND

Motivated by the clinical significance and the mutual positional relationship of the neural canal opening (NCO) and retinal vessels, in this Ph.D. project, we segment 1) the NCO to help provide a stable reference plane for the evaluation of other glaucomatous structural changes and 2) the retinal vessels with a focus on the region near and inside the NCO to help better identify the NCO and other anatomic structures, and potentially help the diagnosis of glaucoma. In addition, the segmentation of retinal vessels could also aid the registration between intra- and inter-modality images.

As the spectral-domain optical coherence tomography (SD-OCT) is relatively new, the automated detection of the NCO and retinal vessels has not yet been intensively investigated. However, many algorithms in the detection of the clinical optic disc margin (partially corresponding to the NCO) and retinal vessels on fundus photographs have been developed. This chapter provides an overall introduction of the technical background related to the NCO/clinical optic disc margin and retinal vessel segmentation in both SD-OCT volumes and color fundus photographs. Section 3.1 is a general overview of the prior and our NCO/clinical optic disc margin segmentation approaches and 3.2 is a general overview of the prior and our vessel segmentation approaches.

3.1 NCO segmentation in SD-OCT volumes

This section provides an overview of the prior and our NCO/clinical optic disc margin segmentation approaches in SD-OCT volumes and fundus photographs. More

specifically, Section 3.1.1 and 3.1.2 introduce the prior approaches of clinical disc margin segmentation on fundus photographs and in SD-OCT volumes respectively; Section 3.1.3 provides the prior approaches of the NCO segmentation. Section 3.1.4 is an introduction of the optimal graph search and our graph-theoretic NCO segmentation approach with the application in SD-OCT volumes of human eyes; and an introduction of our 3-D wavelet-transform-learning-based NCO segmentation approach with the application in SD-OCT volumes of non-human primate eyes is provided in Section 3.1.5.

3.1.1 Prior approaches of clinical disc margin segmentation on fundus photographs

Although the segmentation of the NCO in SD-OCT volumes has not yet been extensively investigated, the segmentation of the clinical disc margin on fundus photographs including the manual and automated approaches has been widely reported. For the manual approaches, it is known that they are time-consuming and introduce substantial inter-observer variability [6, 7]. For the automated approaches, several reported algorithms restrict the optic disc margin to a particular shape. For example, Zhu *et al.* [21] presented an automated approach to segment the clinical optic disc margin using Hough transform by imposing a circular shape. Wong *et al.* [22] reported a variational level-set based approach with the post-processing of elliptical fitting. Li *et al.* [23, 24] demonstrated an approach by utilizing the principal component analysis (PCA) to approximately locate the optic disc margin and then applying a parametrically deformable model - active shape model (ASM) - to refine the optic disc boundary. But the clinical visible optic disc margin in fundus photographs is a

complex of a few anatomic structures, rather than a single constant anatomic structure. Several shape models are not sufficient to represent the real changes of the optic disc margin due to various pathologies.

A few other algorithms allowed a higher variability of the shape of the optic disc margin. For example, Xu *et al.* [25] presented a free-form deformable (active contour) model - a variational snake - to detect the optic disc margin. However, the performance of the deformable model based approaches strongly relies on a proper initialization of the detected boundary. In addition, they involve converging to a local minimum and do not guarantee finding a globally optimal solution.

Abràmoff *et al.* [26] recently proposed a supervised pixel-classification-based approach to detect the optic disc margin. However, in some cases, such approach yielded fuzzy disjoint regions. Merickel *et al.* [27] presented an approach upon the combination of the graph search and pixel classification algorithms. Specifically, they utilized a soft pixel classification method to generate a probability map of the optic disc and segmented the disc margin using a graph search method applied on the probability map by maximizing the probability of the disc margin. As the optic disc margin segmentation strongly depends on the quality of the classification, the fuzzy disjoint region presented in some cases from the classification approach could cause the segmentation errors.

3.1.2 Prior approaches of clinical disc margin segmentation in SD-OCT volumes

With the increasing availability of SD-OCT volumes, the interest of identifying the optic disc margin in SD-OCT volumes is increasing. We [28, 29] have recently

described a voxel classification approach for automatically segmenting the clinically familiar glaucomatous parameters - the optic nerve head (ONH) rim and cup - directly from the SD-OCT volumes by extending our prior approach for automated planimetry on stereo fundus photographs [26,27]. However, this approach has the ultimate limitation that the algorithm essentially mimics the subjective assessment of 2-D parameters by human experts. It is not based on objective, anatomical landmarks within the 3-D volumes. As mentioned in previous chapters, we and others [4,5] have found that the optic disc margin does not overlap with a single constant anatomic structure in volumetric OCT. The varying combinations of the termination of Bruch's membrane, border tissue, or the anterior scleral canal opening may manifest as the 2-D disc margin seen on photographs, depending upon the border tissue architecture and anatomy.

3.1.3 Prior approaches of NCO segmentation in SD-OCT volumes

To the best of our knowledge, we are not aware of an automated algorithm to detect the NCO in SD-OCT volumes. Strouthidis *et al.* [4] recently developed a manual system for the detection of NCO and its characteristics within 3-D histomorphometric and 3-D SD-OCT reconstructions of the ONH from monkey eyes. The NCO was delineated within every section of each histomorphometric and 3-D spectral domain optical coherence tomography reconstruction. However, with the increasing availability of SD-OCT volumes, automatically identifying NCO is becoming increasingly relevant.

3.1.4 Optimal graph search and our NCO segmentation in SD-OCT volumes of human eyes

Graph-based automated surface/boundary segmentation approaches have been widely reported. The graph-based approaches, such as the "graph cut" approach for finding a single surface by Boykov *et al.* [30], the graph search approach for finding a single surface by Wu and Chen [10], the extension of the graph search approach for finding multiple surfaces by Li *et al.* [11] using edge information, the extension of graph search approach for finding multiple surfaces using additionally regional information by Garvin *et al.* [12, 31], etc. [32, 33], have been very attractive due to the ability of finding the globally optimal solution.

Based on Li's original graph search approach [11] [34], we develop a graph-theoretic algorithm for the identification of the NCO in SD-OCT volumes with the application on human eyes [35, 36]. The central advantage of the graph-theoretic approach over the above clinical optic disc margin segmentation approaches is that it guarantees finding a globally optimal solution with respect to the designed cost function. Chapter 4 provides the details of this approach.

3.1.5 Our 3-D wavelet-transform-learning-based NCO segmentation in SD-OCT volumes of non-human primate eyes

It is known that the globally optimal solution of the graph search is highly dependent on the designed cost function. As can be seen in Chapter 4, our prior graph-theoretic NCO segmentation approach in SD-OCT volumes of human eyes in general performs well. However, the cost function is simply a signed edge-based term in the original image space for both the involved retinal layer and NCO boundary

segmentation. The segmentation errors exist in some cases for both the surfaces and NCO when high frequency noise exists, interrupted objects such as large blood vessels are present, and/or strong edge information is missing.

Multiscale or multiresolution image analysis has been widely applied on various image modalities due to the ability to capture both the coarse and fine level details of the images [37, 38]. Various wavelet transforms have been used for the multiscale image processing due to the desirable properties such as the scale and frequency selectivity [37, 39].

Quellec *et al.* [40] reported a content-based approach to retrieve the similar 2-D images from different image databases based on the image signature derived from an adaptive nonseparable 2-D wavelet transform via a lifting scheme. Recently, they have extended their 2-D wavelet transform to 3-D version with the strong motivation to help remove the speckling and other high frequency noise and help extract texture properties in SD-OCT volumes [9].

Thus, we develop a 3-D wavelet-transform-learning-based NCO segmentation approach with the application in SD-OCT volumes of non-human primate eyes for the aim to enhance our prior NCO segmentation by a particular focus on the enhancement of the cost function design from the following aspects: 1) Enhance the NCO and layer segmentation using the 3-D wavelet-transform-learning-based cost function for the graph searching. The wavelet transform is performed based on Quellec's previous 3-D lifting-scheme-based wavelet transform [9, 40] approach tuned by the genetic algorithm. 2) Enhance the NCO segmentation by incorporating the pre-identified vessel positional information into the cost function design of the graph searching.

The further details of the 3-D wavelet-transform-learning-based NCO segmentation are presented in Chapter 5.

3.2 Retinal vessel segmentation

This section provides an overview of the prior and our retinal vessel segmentation approaches in SD-OCT volumes and fundus photographs. More specifically, the prior approaches of vessel segmentation on fundus photographs is provided in Section 3.2.1; Section 3.2.2 is an introduction of the classifiers and k-Nearest Neighbor (k-NN) classifier; Section 3.2.3 is an overview of prior vessel segmentation approaches in SD-OCT volumes; Section 3.2.4 introduces our single modal vessel segmentation in SD-OCT volumes; and an introduction of our registered-fundus and multimodal vessel segmentation in SD-OCT volumes and color fundus images using additional fundus image information is provided in Section 3.2.5.

3.2.1 Prior approaches of vessel segmentation on fundus photographs

Since the wide availability of the fundus photographs, many approaches have been developed to segment the blood vessels in fundus photographs. For instance, Chaudhuri *et al.* [41] reported a matched filter based approach using the oriented Gaussian filter and then thresholding the resulting image. Martínez-Pérez *et al.* [42] developed a posterior statistical region growing approach incorporating multiscale features. Zana *et al.* [43] provided a mathematical morphological approach which defined the vessel-like patterns by morphological properties and then used a cross-curvature evaluation to differentiate the vessels from analogous background patterns.

Jiang *et al.* [44] reported an adaptive thresholding approach by utilizing a verification-based multithreshold probing scheme. Niemeijer *et al.* [45] described a supervised pixel classification based method which extracted the pixel features using a Gaussian filter bank and then applied a k-NN classifier to classify the unseen pixel into either "vessel" or "non-vessel". Tolias *et al.* [46] presented a vessel tracking based approach with the tracking of a blood vessel driven by a fuzzy model of a 1-D vessel profile.

To investigate the performance of the above typical vessel segmentation approaches, Niemeijer *et al.* [45] compared the first five approaches based on a large database of retinal images using the criterion of the maximum average accuracy. Among them, the pixel classification based method provided a best segmentation accuracy. Although not been compared, the vessel tracking approach is known to have its limitations. 1) It requires human intervention to find each vessel. 2) It has the tendency to terminate at branching and crossover points.

3.2.2 Classifiers and k-NN classifier

Machine learning has been a very active research area recently with the increasing availability of various classifiers, such as the Support Vector Machine (SVM), k-NN, Neural Networks (NNs), Quadratic Discriminant Classifier (QDC), and Linear Discriminant Classifier (LDC), etc. The choice of the classifiers is not a trivial task. Niemeijer *et al.* [47] has recently compared a few classifiers, i.e., the SVM, k-NN, QDC, and LDC, based on investigation of the image structure clustering for image quality verification of color retina images in diabetic retinopathy screening. The results showed that the performance of the SVM and k-NN were similar and better

than the QDC and LDC. However, SVM was relative slow in the training stage and required a lot of tuning of multiple parameters. It is known that the NNs have even more parameters and are more difficult to tune. The k-NN classifier has been an attractive classifier due to the the ease of tuning. Arya *et al.* [48] developed an Approximate Nearest Neighbor (ANN) searching approach which allows a tolerance of a small amount of error when searching the nearest neighbor training samples for each query (test) sample, which can reduce the running time. In addition, as mentioned above, Niemeijer *et al.* [47] has shown the good performance of k-NN classifier on vessel segmentation. Thus in this work we use the k-NN classifier with the real implementation of using the ANN approach to classify the vessels.

3.2.3 Prior vessel segmentation in SD-OCT volumes

Due to the fact that the retinal blood vessels absorb the wavelengths of light used in SD-OCT, the vessels in these volumes are mostly not directly visible. However, vessel silhouettes appear below the position of the vessels. As reported by Wehbe *et al.* [49], the retinal vessels are located right above the vessel silhouettes in the z-direction of the OCT volumes and these silhouettes can be used to detect the location of the vessels.

The blood vessel segmentation in SD-OCT volumes of the ONH is not a trivial problem for a number of reasons. 1) The vessel silhouettes have a weak visibility in OCT due to the 3-D structure of the ONH. 2) Many vessels can overlap in regions, especially the region inside the neural canal opening, where the individual vessels cannot be discerned. 3) The presence of the NCO boundary, which crosses with the

vessels, causes false positives for the vessel segmentation. 4) The vessel silhouettes have a decreased contrast with the background within the NCO, due to more variable tissue properties in the ONH.

With the increasing interest of the high resolution, three-dimensional SD-OCT volumes, a few retinal blood vessel segmentation algorithms performed in SD-OCT volumes of ONH were recently presented [50, 51]. For example, Niemeijer *et al.* [50] recently applied their pixel-classification-based approach on fundus photographs to the vessel segmentation in ONH-centered SD-OCT volumes. However, typical vessel segmentation approaches for SD-OCT volumes of the ONH, such as the one from Niemeijer, focus on the region outside the NCO due to the difficulties associated with the relatively low visibility in the ONH center and the similar projective appearance of the NCO contour to the vessels, which causes false positives near the NCO as indicated by the red arrow in Fig. 3.1.c.

3.2.4 Our single modal OCT vessel classification approach in SD-OCT volumes

To suppress the above mentioned false positive tendency in the vessel segmentation due to the presence of the NCO contour, we develop a single modal supervised, pixel-classification-based retinal vessel segmentation approach performed in SD-OCT volumes [52], which pre-segments the NCO in SD-OCT volumes using the method presented in Chapter 4 and then incorporates the pre-segmented NCO positional information into the vessel classification process to suppress the false positives near the NCO boundary. The further details of this approach are presented in Chapter 6.

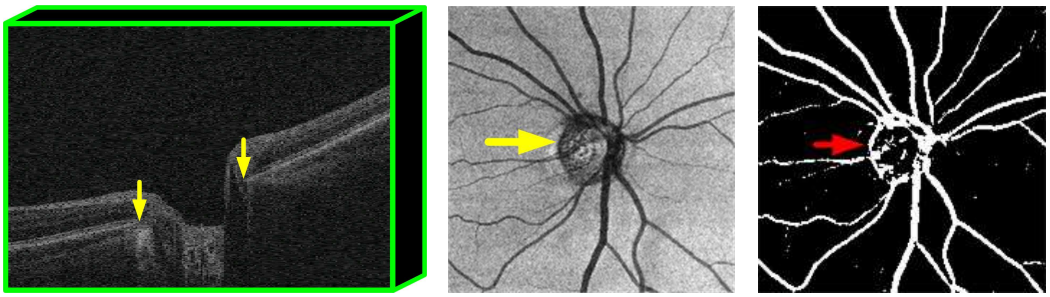

(a) (b) (c)

Figure 3.1: Illustration of the NCO false positives from Niemeijer's [50] previous vessel segmentation approach in SD-OCT volumes of ONH. (a) Central slice of raw SD-OCT volume with the highlight of NCO location (yellow arrows). (b) OCT projection image used for Niemeijer's vessel segmentation with the highlight of NCO location (yellow arrow). (c) Vessel segmentation from Niemeijer's previous approach in SD-OCT volumes of ONH. Note the typical false positives near the NCO boundary (red arrow).

3.2.5 Our vessel classification approaches in SD-OCT volumes using additional fundus image information

As shown in Chapter 6, our single modal vessel classification approach in SD-OCT volumes provides an obvious improvement over Niemeijer's [50] previous approach. However, the relative low visibility of the ONH center in SD-OCT volumes remains a problem for the vessel identification in some scans. Color fundus images, however, provide a high vessel visibility in the ONH center. We thus develop a registered-fundus vessel segmentation approach which first segments the vessels on fundus images [45] and then registers the segmented vessels to OCT [53]. Such approach also has some limitations, such as the similar false positives around the optic disc margin on fundus images.

With the fast development of advanced technology and new modalities, developing

image analysis techniques to utilize the rich and complementary information from multiple image sets of the same modality, such as the brain imaging sequences of magnetic resonance imaging (MRI) [54], or from multiple modalities, such the lung images of positron emission tomography (PET) and computed tomography (CT) and the prostate images of CT and MRI [55], is becoming more attractive.

Recently, a few algorithms of the multimodal image segmentation on the retinal images have been reported [56, 57]. For example, Li *et al.* [57] presented a ridge-branch-based blood vessel detection algorithm in multimodal retinal images such as color fundus photographs, fluorescein angiograms, fundus autofluorescence images, and scanning laser ophthalmoscopy (SLO) fundus images. To the best of our knowledge, there is no such a multimodal blood vessel segmentation approach applied on multimodal images of SD-OCT volumes and color fundus photographs and particularly focused on the region near and inside the NCO.

The SD-OCT volumes and color fundus photographs provide some complementary features that could help better identify the blood vessels near and inside the NCO. Simultaneously segmenting the vessels in both modalities could take advantage of their complementary features such as the 3-D retinal layer and NCO information from SD-OCT volumes [36] and the better vessel visibility in the ONH center from fundus photographs.

Thus, we further develop a multimodal concurrent classification approach [58] with a focus on the ability to better segment the blood vessels near and inside the NCO in SD-OCT volumes by simultaneously using the information from SD-OCT volumes and color fundus photographs. Chapter 7 provides the details of the registered-fundus

and multimodal vessel segmentation approaches.

CHAPTER 4
GRAPH-BASED NEURAL CANAL OPENING SEGMENTATION IN SD-OCT VOLUMES OF HUMAN EYES

4.1 Chapter abstract

The neural canal opening (NCO) is of interest due to its use for the help of detecting and managing glaucoma. In this work, we develop a method for segmenting the NCO of the optic nerve head (ONH) in spectral-domain optical coherence tomography (SD-OCT) volumes using a graph-theoretic approach with the application in human eyes. More specifically, four 3-D intraretinal surfaces are first segmented in SD-OCT volumes and a small number of slices surrounding the NCO plane is taken and used for creating planar NCO-aimed OCT projection images. An edge-based cost function - a signed edge-based term favoring a dark-to-bright transition in the vertical direction of polar projection images (corresponding to the radial direction in Cartesian coordinates) - is obtained. A graph-theoretic approach is used to simultaneously identify the NCO and optic cup at the retinal pigment epithelium/Bruch's membrane (RPE/BM) plane. Two datasets are used in this study. First, 68 SD-OCT volumes (Cirrus ^{TM} HD-OCT) and corresponding stereo fundus photographs (Nidek 3Dx) of the ONH are obtained from 68 eyes of 34 patients with glaucoma or glaucoma suspicion. Manual planimetry is performed by three glaucoma experts to delineate a reference standard (RS) for cup and disc margins from 3Dx images. In addition, 232 SD-OCT volumes from 58 subjects with glaucoma or glaucoma suspicion on two separate visits are also obtained. The algorithm segmentation is first validated by comparing the performance to that of the clinical disc margin defined from the man-

ual planimetry from 34 subjects. The mean unsigned and signed border positioning differences of the algorithm with the RS are 2.81 ± 1.48 pixels (84.3 ± 44.4 μm) and -0.99 ± 2.02 pixels (-29.7 ± 60.6 μm) respectively. The correlations of the linear cup-to-disc (NCO) area ratio, disc (NCO) area, rim area, and cup area of the algorithm with the RS are 0.85, 0.77, 0.69, and 0.83, respectively. In most eyes, the NCO-based 2-D metrics correlate well with RS. However, a small discrepancy exists in the NCO-based anatomic structures and the clinical disc margin of the RS in some eyes. The algorithm is further validated based on the repeatability analysis from additional 58 subjects. The mean unsigned and signed border positioning differences between visits are 1.21 ± 0.57 pixels (36.41 ± 17.06 μm) and 0.02 ± 0.81 pixels (0.58 ± 24.21 μm) respectively. The correlation of the NCO area between visits is 0.95 (0.93-0.97). The area and border positioning measurements of the NCO are robust across repeated visits. The NCO may serve as a stable reference landmark for describing structural changes that occur in glaucoma.

4.2 Introduction

As mentioned previously (Chapter 1), the core hypothesis motivating this overall Ph.D. study is that the segmentation of a stable three-dimensional structure - the NCO - from SD-OCT will enable more reproducible and objective glaucomatous parameters than that which is currently possible from manual planimetry alone (even using a consensus of glaucoma experts). This is fundamentally different from our prior voxel classification method (Chapter 3.1.2) [29] which, by construction (using training data), attempts to obtain parameters as close as possible to that which would

be obtained using manual planimetry of stereo fundus photographs.

The purpose of this specific study is to describe a graph-theoretic algorithm for automatic delineation of the NCO from SD-OCT volumes and optic disc metrics derived from the NCO (and cup boundaries) and to compare these with the reference standard (disc and cup margins) obtained from human expert planimetry of stereo photographs of the same eye [35, 36, 59].

While the present study does not directly test our hypothesis, it sets the necessary underlying framework for being able to automatically detect the NCO and better understand its relationship with the widely accepted optic disc margin from manual planimetry.

4.3 Patients

Two datasets with the first one of 34 consecutive patients [29] and the other one of 58 consecutive patients with the diagnosis of glaucoma suspect, open-angle glaucoma, angle closure glaucoma, or combined mechanism glaucoma from the Glaucoma Clinic at the University of Iowa are included in this study. Non-glaucomatous optic neuropathy is excluded. The patient cohort has been described in detail in a previous report [29]. The diagnoses are made by the treating glaucoma specialist. The study is approved by the Institutional Review Board of the University of Iowa, and adheres to the tenets of the Declaration of Helsinki, and all subjects give written informed consent.

4.4 Image acquisition

4.4.1 Image acquisition of 34 consecutive patients

Sixty eight ONH-centered SD-OCT scans of 34 consecutive study subjects are acquired using a Cirrus^{TM} HD-OCT (Carl Zeiss Meditec, Inc., Dublin, CA, USA) device. The OCT scans are exported in an uncompressed raw format (40Mb per scan), preserving the voxel intensities. Each SD-OCT scan consists of 200 $\times$ 200 $\times$ 1024 voxels and the physical dimensions are $6 \times 6 \times 2$ mm^3. Thus the voxel resolution is 30 $\times$ 30 $\times$ 2 μm [29]. The voxel depth is 8 bits in grayscale. 68 corresponding stereo color fundus photographs of the optic disc are also acquired on the same day using a Nidek 3Dx stereo retinal camera with a fixed stereo base with a digital camera back (Nidek, Newark, NJ). The size of the stereo color fundus disc photographs is 4096 $\times$ 4096 pixels and the pixel depth is 3 $\times$ 8-bit in red, green, and blue channels.

4.4.2 Image acquisition of 58 consecutive patients

Two hundred and thirty two more ONH-centered SD-OCT scans of 58 consecutive study subjects with glaucoma or glaucoma suspicion are further acquired from the same SD-OCT machine as that for the 34 patients for the measurement of repeatability. Each subject has OCT scans for both eyes done on 2 separate visits within a 3 month period. Multiple images are taken during each visit.

4.5 Methods

Overall, we approach the automatic segmentation of the NCO in SD-OCT volumes by first segmenting four 3-D intraretinal surfaces in the raw SD-OCT volumes and the raw OCT volumes are flattened [12, 28, 31]. This allows that a small number of

slices surrounding the NCO plane are taken and used for creating a planar NCO-aimed OCT projection image. The projection image is then transformed to polar coordinates. The optimal graph search is performed in the polar cost images to find two boundaries simultaneously [35, 36]. Fig. 4.1 is the flowchart of the major steps of our graph-based NCO segmentation in SD-OCT volumes of human eyes.

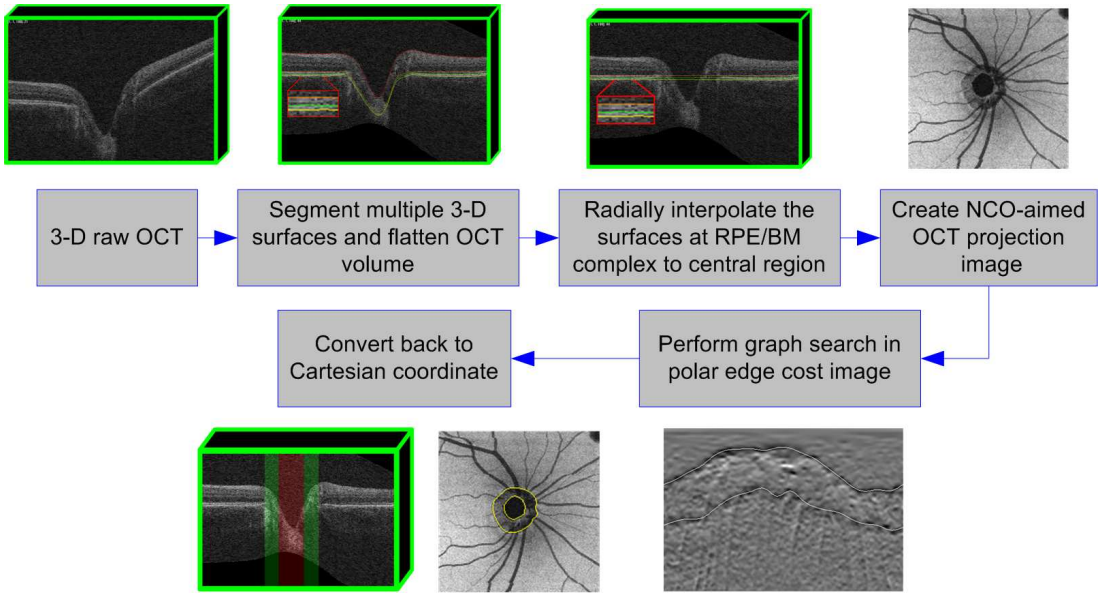

Figure 4.1: Flowchart of major steps of the graph-based NCO segmentation in SD-OCT volumes of human eyes.

4.5.1 OCT volume flattening

Because of the shape of the globe, the scanner position relative to the patients' pupil, and the eye movement, the original raw OCT image is deformed elastically. Thus four intraretinal surfaces are segmented in 3-D and the raw OCT volume is flattened [12, 31] based on the second segmented surface as described previously [28].

The four segmented surfaces are also translated by applying the same transformation. From the top to bottom (Fig. 4.2.b and Fig. 4.2.e), surface 1 corresponds to the internal limiting membrane (ILM). Surface 2 is located between the inner and outer segments of the photoreceptors. Surface 3 is the inner boundary of the RPE/BM complex and surface 4 is the outer boundary of the RPE/BM complex. Surface 2 is chosen as the flattening surface (in this stage) for consistency with our prior work [28]; however, surface 3 would have worked equally well in this flattening stage as one of its major purposes is only to remove the motion artifacts across B-scans to make the NCO and cup segmentation easier. As shown in Fig. 4.2.c and Fig. 4.2.f, the geometrical distortion across B-scans is improved after the flattening, though not perfect. The flattening also provides a possibility to create an OCT projection image from a thin layer at the RPE/BM complex for correspondingly comparing the NCO-based parameters to those of fundus photographs.

4.5.2 NCO-aimed OCT projection image creation

Due to the large variations in the surface of the ONH, intraretinal layer segmentation differences could occur and cause a non-optimal flattening problem, i.e., the NCO points do not lie on a plane after flattening. Therefore we first establish an estimated NCO region, a circular region centered on the geometric center of the OCT volume with a radius certain to be larger than the estimated NCO boundary (Fig. 4.3.a). A projection image is formed by taking the thin layer between surface 2 (orange) and surface 4 (yellow), by extrapolating the average position outside the estimated NCO region for surface 2, 3, and 4 to the inside region radially (Fig. 4.3.b). Thus the 3-D

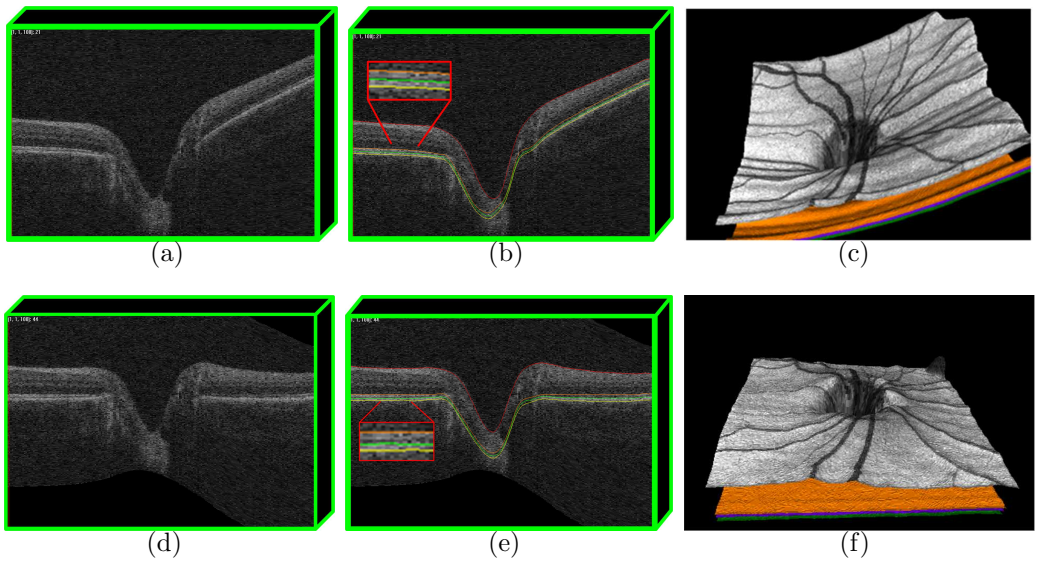

Figure 4.2: Illustration of SD-OCT volume flattening. (a,d) Central slice of the original and flattened SD-OCT volume respectively. (b,e) Four surface segmentation of original and flattened SD-OCT volume respectively. (c,f) 3-D rendering of the surface segmentation of the original and flattened SD-OCT volume respectively by mapping the OCT projection image texture onto the top surface.

NCO segmentation problem is converted to a 2-D problem. The projection image is referred to as the "NCO-aimed" OCT projection image (Fig. 4.3.c).

4.5.3 NCO and optic cup segmentation at the RPE/BM plane

In NCO-aimed OCT projection images, the outer boundary corresponds to the NCO and the inner boundary corresponds to the cup at the level of the NCO reference plane (Fig. 4.3.c). A two-dimensional graph search is applied to simultaneously segment the optimal NCO and cup boundaries [35].

More specifically, in order to perform the two-boundary graph search, the NCO-aimed OCT projection image in the Cartesian coordinates is transformed to polar

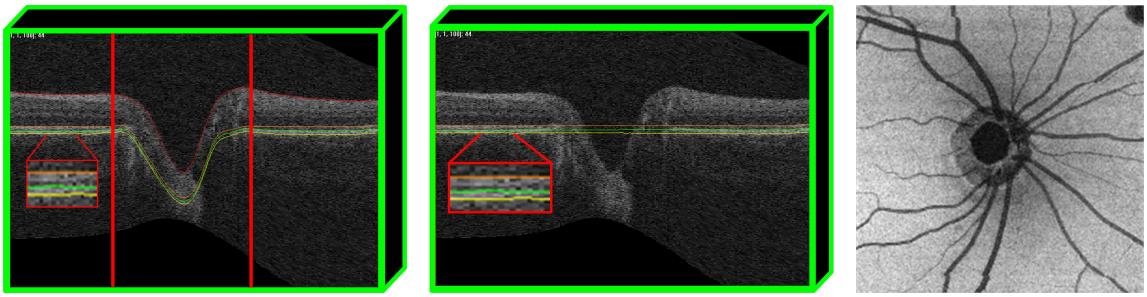

(a) (b) (c)

Figure 4.3: Illustration of NCO-aimed projection image creation. (a) Estimated NCO region indicated by the red lines. (b) Planar surfaces near RPE/BM complex obtained by extrapolating the average position outside the estimated NCO region for surface 2, 3, and 4 to the inside region radially. (c) NCO-aimed OCT projection image.

coordinates and is sampled from the center point radially outward with certain rays (corresponding to the angles) and certain samples per ray (corresponding to the radii). The center point must be within the optic cup for the transformation to be valid.

The cost function is a signed edge-based term favoring a dark-to-bright transition in the vertical direction (corresponding to the radial direction in Cartesian coordinates) in the transformed NCO-aimed OCT projection image. In our case, the cost image in polar coordinates is modeled as a weighted, directed graph similar to the one described by Li *et al.* [11] but reduced to a two-dimensional problem. More specifically, the unwrapped cost image is treated as a graph $G = (V, E)$ with a collection of vertices V and edges E. In the 2-D unwrapped cost image of $I(x, z)$ of size $X \times Z$, the boundary segmentation problem is transformed to a multi-column graph search problem with $X \times Z$ vertices (corresponding to $X \times Z$ pixels). For simplicity, any boundary in I is considered to intersect with exactly one pixel (vertex) in each column of pixels (vertices) parallel to the z-axis. Each column associated with x also has two

adjacent neighbor columns associated with $x+1$ and $x-1$. We also add a circularity neighbor relationship for the two edge columns in the x direction, i.e., the column associated with $x = 0$ is considered to be a neighbor to the column associated with $x = X - 1$.

To segment the two boundaries simultaneously, the graph G consists of two disjoint subgraph $\{G = (V_i, E_i | i = 1, 2)\}$. Each subgraph contains $X \times Z$ vertices.

Two kinds of feasibility constraints - intraboundary (smoothness) constraints and interboundary (interaction) constraints - are enforced on the constructed multi-column graph. The two boundaries are considered feasible if each individual boundary in the subgraph satisfies the given smoothness constraints and the two boundaries satisfy the boundary interaction constraints. More specifically, for each single boundary $z = f(x)$, the smoothness feasibility constraint Δ_x is enforced to define the allowed change in the boundary height when moving from one neighboring boundary point to the next in the x-direction, i.e. if $(x_1, f(x_1))$ and $(x_2, f(x_2))$ are two neighboring vertices on a feasible boundary, the smoothness feasibility constraint requires that $|f(x_1) - f(x_2)| \leq \Delta_x$. For two boundaries of $z_1 = f_1(x)$ and $z_2 = f_2(x)$, the boundary interaction constraints δ^l and δ^u are enforced to define the allowed minimum and maximum changes in boundary height between the surface pair, i.e. if $(x, f_1(x))$ and $(x, f_2(x))$ are two vertices on two feasible boundaries, the interaction constraints require that $\delta^l \leq |f_1(x) - f_2(x)| \leq \delta^u$. Both δ^l and δ^u are positive in our case as the two boundaries do not intersect or overlap. The actual values of Δ^x, δ^l, and δ^u are chosen based on the observation and the prior knowledge. Fig. 4.4 is an illustrative example of the intra-boundary and inter-boundary feasibility constraints.

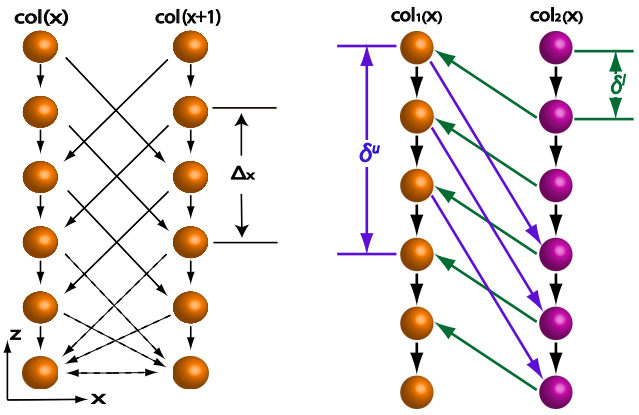

(a) (b)

Figure 4.4: Graph representation of feasibility constraints. (a) Intra-boundary smoothness constraint with $\Delta_x = 2$. (b) Inter-boundary interaction constraints with $\delta^l = 1$ and $\delta^u = 3$.

The two-boundary segmentation problem is an optimization problem with the goal being to find the two boundaries with the minimum cost. Finding two optimal boundaries is transformed to find a minimum-cost closed set. The minimum-cost closed set is found by computing a minimum $s-t$ cut in a closely-related graph [11].

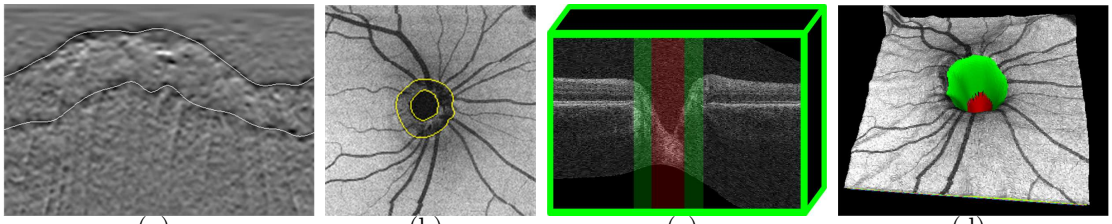

(a) (b) (c) (d)

Figure 4.5: Illustration of the NCO and optic cup segmentation overlapping with different images. (a-c) Segmented NCO and cup overlapping with (a) unwrapped cost image, (b) projection image, (c) a cross-sectional slice of OCT volume, and (d) 3-D rendering of the NCO and cup segmentation overlapping with the mapping of the projection image texture onto the top surface.

The (optimal) NCO and cup boundaries are thus simultaneously segmented by the graph search approach. In shallow cups (or if the cup is absent), the deepest point of the top surface does not extend below the level of the RPE/BM plane (the green line indicated surface in Fig. 4.3.b). When this occurs, the algorithm automatically switches from using a two-boundary graph search to using a one-boundary graph search so that the NCO is determined using the single-boundary graph search method. The NCO and cup boundaries are finally smoothed using a B-spline. Fig. 4.5 shows an example of the segmented NCO and optic cup overlapping with the cost function, OCT projection image, and OCT image respectively.

4.6 Validation

4.6.1 Comparison of algorithm to expert planimetry stereo color photographs

Computer-aided planimetry is performed by three fellowship-trained glaucoma experts on stereo color photographs of the optic disc, as described previously [29]. A reference standard (RS) is obtained from three expert segmentations on the color fundus images in a "majority-win" manner, i.e., each pixel is assigned a class that receives the majority of votes. For example, if two votes are for a pixel to be rim and one vote for a pixel to be cup, the pixel is assigned to rim [28, 29]. The linear cup-to-disc area ratio, or LCDR, is defined as the square root of the cup area over disc area.

In order to determine the transformation necessary to convert the expert segmentations on the stereo color fundus images to the SD-OCT space, manual registration is performed as described previously [29]. More specifically, a projection image is cre-

ated by averaging the voxels between the second and fourth intraretinal surfaces (i.e. the surfaces indicated by the orange and yellow lines in (Fig. 4.3.a). Note that this projection image is different from the NCO-aimed OCT projection images created for finding the NCO. The goal of creating this projection image is to obtain the RS for OCT scans and so the projection image is referred to as "RS-aimed projection image". The manual registration is performed by matching blood vessels between the stereo retinal fundus images and the corresponding RS-aimed projection images. The RS and the three expert segmentations from the stereo fundus images are also converted to the SD-OCT space by applying the same transformation [28, 29].

The segmented NCO boundary is compared to the RS disc margin, using mean unsigned and signed border positioning differences, i.e., the closest Euclidean distances between the segmented NCO points from our algorithm and those from the RS and vice versa. The signed difference is measured in terms of the disc center of the RS. If the distance of the NCO points to the disc center of the RS is greater than that of the optic disc margin of the RS to its center, the signed difference is positive, and vice versa.

The algorithm is also compared to the RS in terms of the correlations of linear cup-to-NCO/cup-to-disc area ratio, cup area, rim area and also NCO/disc area. The inter-observer correlations of the same parameters are investigated.

4.6.2 Repeatability study

The repeatability [59] is first measured using mean unsigned and signed border positioning differences based on the aligned NCO centers between the first and second

visits. If the distance of the NCO points of the first visit to the aligned NCO center is greater than that of the second visit, the signed difference is positive, and vice versa. The repeatability is also measured in terms of the difference and correlation of the NCO area between the two visits. If the NCO area of the first visit is greater than that of the second visit, the signed difference is positive, and vice versa.

4.7 Results

4.7.1 Segmented NCO vs. reference standard

Table 4.1 shows the mean border positioning differences of the NCO with the optic disc from the reference standard for the 68 eyes of the 34 patients. The mean unsigned and signed difference of the algorithm with the RS for 68 eyes are 2.81 ± 1.48 pixels (84.3 ± 44.4 μm) and -0.99 ± 2.02 pixels (-29.7 ± 60.6 μm) respectively.

Table 4.1: NCO border positioning differences from the 68 eyes

Difference	Algo. vs. RS	Exp. 1 vs. 2	Exp. 1 vs. 3	Exp. 2 vs. 3
Mean unsigned, pixel	2.81 ± 1.48	3.82 ± 1.48	3.39 ± 1.65	2.06 ± 0.95
Mean unsigned, μm	84.3 ± 44.4	114.6 ± 44.4	101.7 ± 49.5	61.8 ± 28.5
Mean signed, pixel	-0.99 ± 2.02	-2.52 ± 1.40	-1.18 ± 1.14	1.36 ± 1.42
Mean signed, μm	-29.7 ± 60.6	-75.6 ± 42	-35.4 ± 34.2	40.8 ± 42.6

Col 1: mean unsigned and signed border positioning differences between the automated NCO segmentation and the optic disc segmentation of the RS.

Col 2, 3, and 4: interobserver variability.

Table 4.2 compares the segmentation results of the 68 eyes with the RS in terms of the correlations with the confidence intervals (CIs) for the linear cup-to-NCO/cup-

to-disc area ratio, NCO/disc area, rim area, and cup area. The correlations of the linear cup-to-NCO/cup-to-disc area ratio, NCO/disc area, rim area, and cup area of the algorithm with the RS for the 68 eyes are 0.85, 0.77, 0.69, and 0.83 respectively.

Table 4.2: Correlations of algorithm with expert segmentation from the 68 scans

Correlation	Algo. vs. RS	Exp. 1 vs. 2	Exp. 1 vs. 3	Exp. 2 vs. 3
LCDR	0.85 (0.76-0.90)	0.88 (0.82-0.93)	0.92 (0.87-0.95)	0.88 (0.81-0.93)
Disc area	0.77 (0.64-0.85)	0.86 (0.79-0.92)	0.91 (0.87-0.95)	0.88 (0.81-0.92)
Rim area	0.69 (0.55-0.80)	0.78 (0.66-0.86)	0.84 (0.75-0.90)	0.80 (0.69-0.87)
Cup area	0.83 (0.73-0.89)	0.93 (0.88-0.95)	0.95 (0.91-0.97)	0.90 (0.85-0.94)

Col 1: correlations of segmented NCO, rim, and cup at RPE/BM plane with disc, rim, and cup from RS (values in parentheses are 95% confidence intervals).

Col 2, 3, and 4: correlations between different expert segmentations (values in parentheses are 95% confidence intervals).

The scatter-plots of the NCO/disc area, rim area, and cup area are illustrated in Fig. 4.6. The scatter-plots of the LCDR and the inter-observer variability are illustrated in Fig. 4.7, with the perfect correlation line indicated as a reference. From Fig. 4.6, the algorithm NCO area is similar to the disc area of the RS, the rim tends to run slightly greater than that of the RS, and the cup tends to run slightly smaller than the RS cup. Correspondingly the algorithm LCDR is slightly smaller than that of the RS (Fig. 4.7).

While the 68-eye analysis are performed to obtain additional statistical power, we also computed the border positioning differences and the correlations of the measured metrics by randomly choosing one eye from each of the 34 patients. The mean border

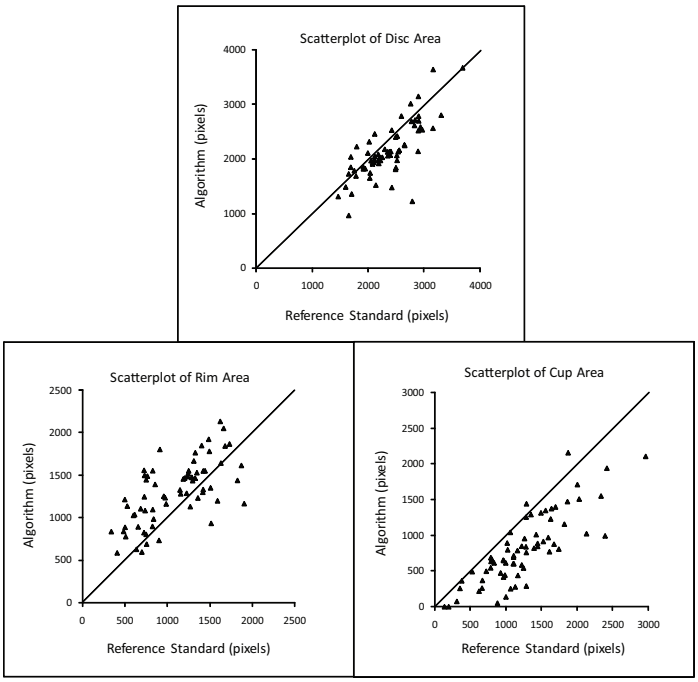

(a)

Figure 4.6: Scatterplots of the NCO, rim, and cup area at RPE/BM plane from the algorithm to disc, rim, and cup area from RS for the 68 eyes. The diagonal line indicates a perfect correlation of 1.0.

positioning differences are 2.68 ± 1.14 pixels (80.4 ± 34.2 μm) and -0.74 ± 1.76 pixels (-22.2 ± 52.8 μm), which are similar to the 68-eye results. The correlations of measured metrics for the 34 eyes are also similar to those of the 68 eyes.

Fig. 4.8 shows the algorithm segmentation from 7 right eyes of 7 randomly chosen patients. The right eye is chosen simply for ease of display (the left eye shows similar results). Each row corresponds to an eye. Fig. 4.9, Fig. 4.10, and Fig. 4.11 visually demonstrate three example segmentation comparisons of our present algorithm, previous algorithm [29], and the RS overlapping with the transformed fundus image and the SD-OCT volume. More specifically, Fig. 4.9 is an example demonstrating a

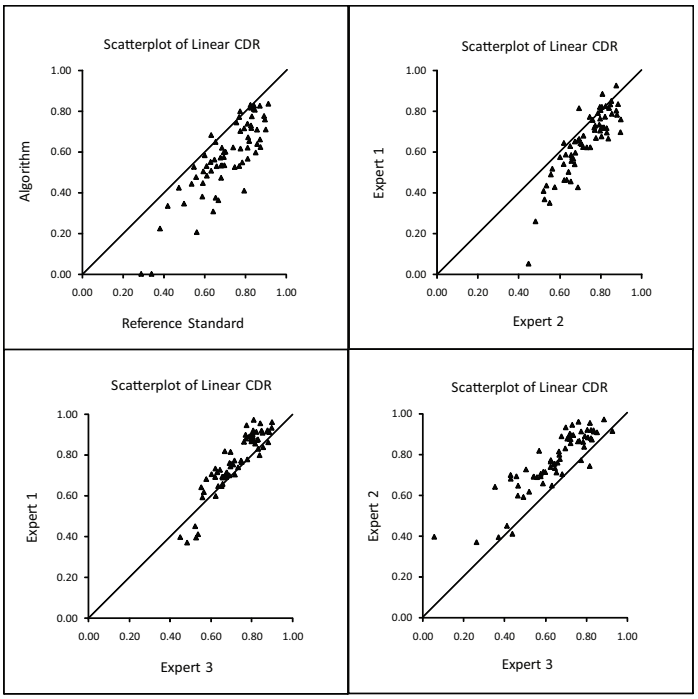

(a)

Figure 4.7: Scatterplots of linear cup-to-NCO (Section 4.6.1) of algorithm to LCDR of RS for 68 eyes. The diagonal line indicates a perfect correlation of 1.0.

good match between the three approaches. Fig. 4.10 and Fig. 4.11 are two examples demonstrating a discrepancy between the present algorithm and the RS, as well as the previous algorithm. The previous algorithm and the RS segment the clinically appreciable defined optic disc margin. The present algorithm instead segments the "true" SD-OCT-based anatomic structures - NCO and optic cup at the RPE/BM complex. From these examples, one can clearly see the sources of the small discrepancies of the NCO and the clinical optic disc, although in most scans, the NCO demonstrates a good match with the clinically appreciable defined optic disc margin obtained by planimetry.

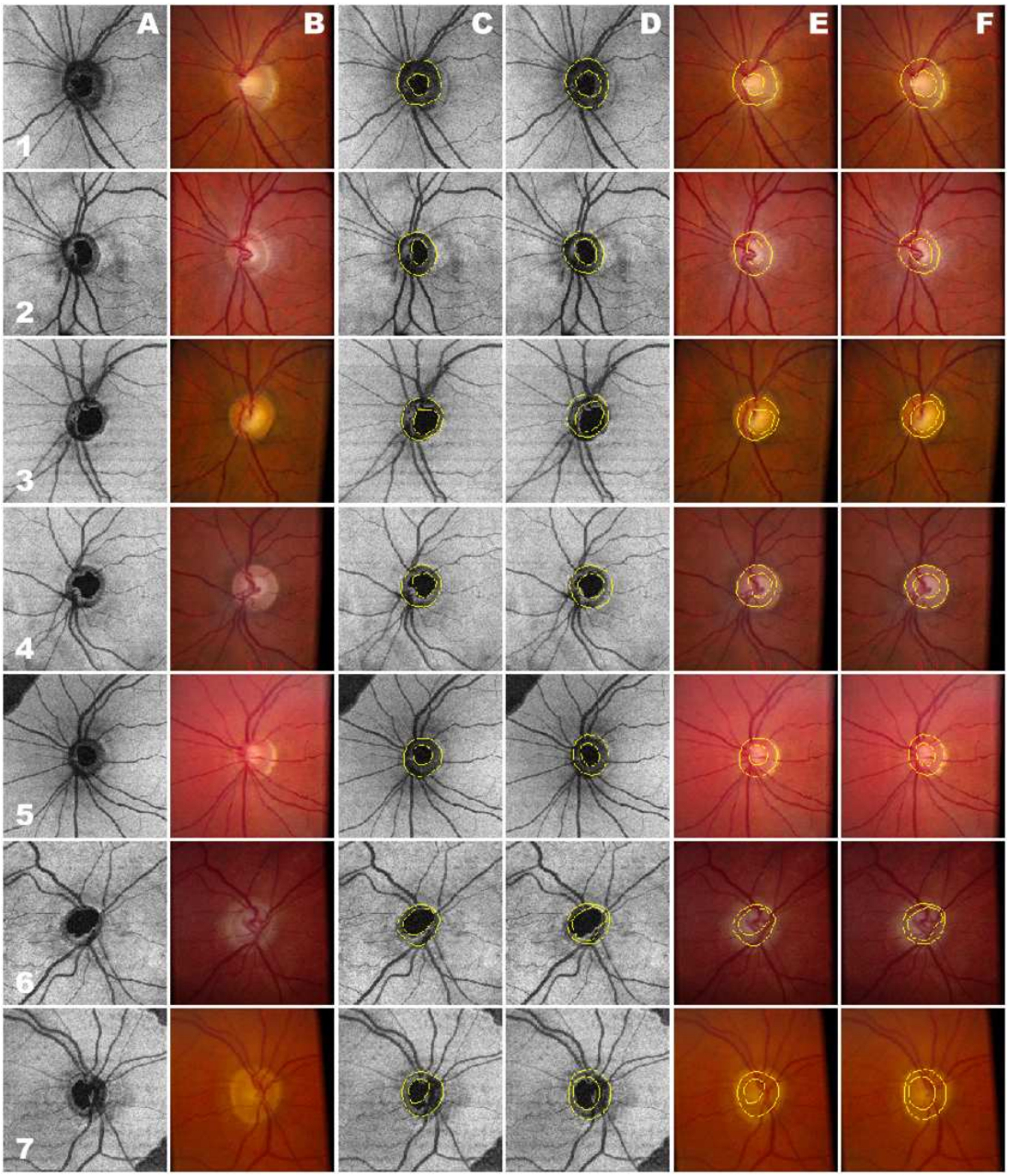

(a)

Figure 4.8: Random selection of example NCO segmentations. (A) NCO-aimed OCT projection image. (B) Corresponding fundus image. (C, D) NCO and cup at RPE/BM plane from present algorithm and disc and cup from RS transposed to NCO-aimed OCT projection image, respectively. (E, F) NCO and cup at RPE/BM plane from present algorithm and disc and cup from RS transposed to fundus image, respectively.

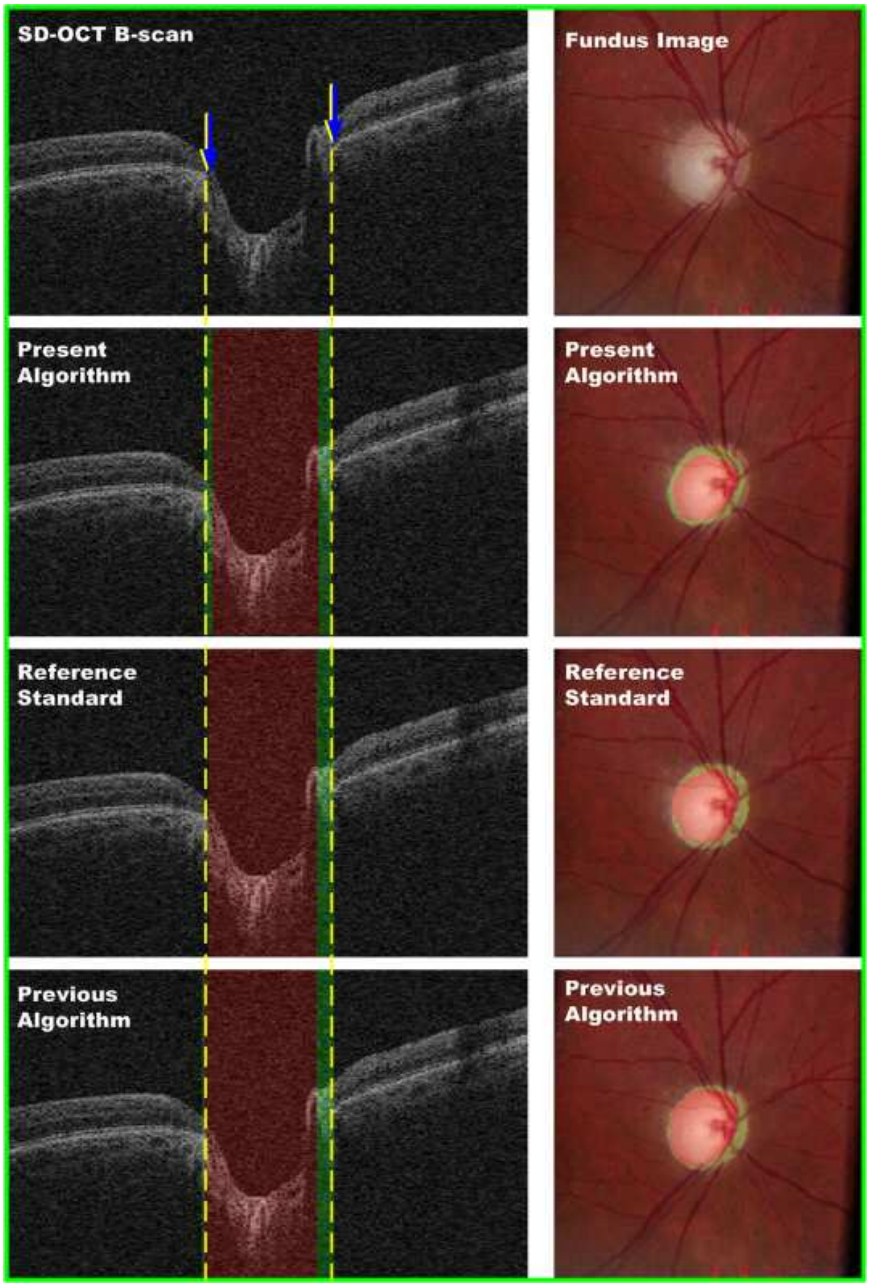

(a)

Figure 4.9: Comparison of present algorithm, expert, and previous algorithm segmentations with a good match. Raw SD-OCT and corresponding fundus image (row 1), present algorithm (row 2), RS (row 3), and previous algorithm (row 4) segmentations overlapping with raw SD-OCT and corresponding fundus image. SD-OCT central B-scan (left). Fundus image (right). Yellow arrows: position of the NCO from the algorithm (dashed yellow line indicates the projected NCO position). Blue arrows: clinical disc from the RS. Green, red: each method's projected rim and cup regions, respectively.

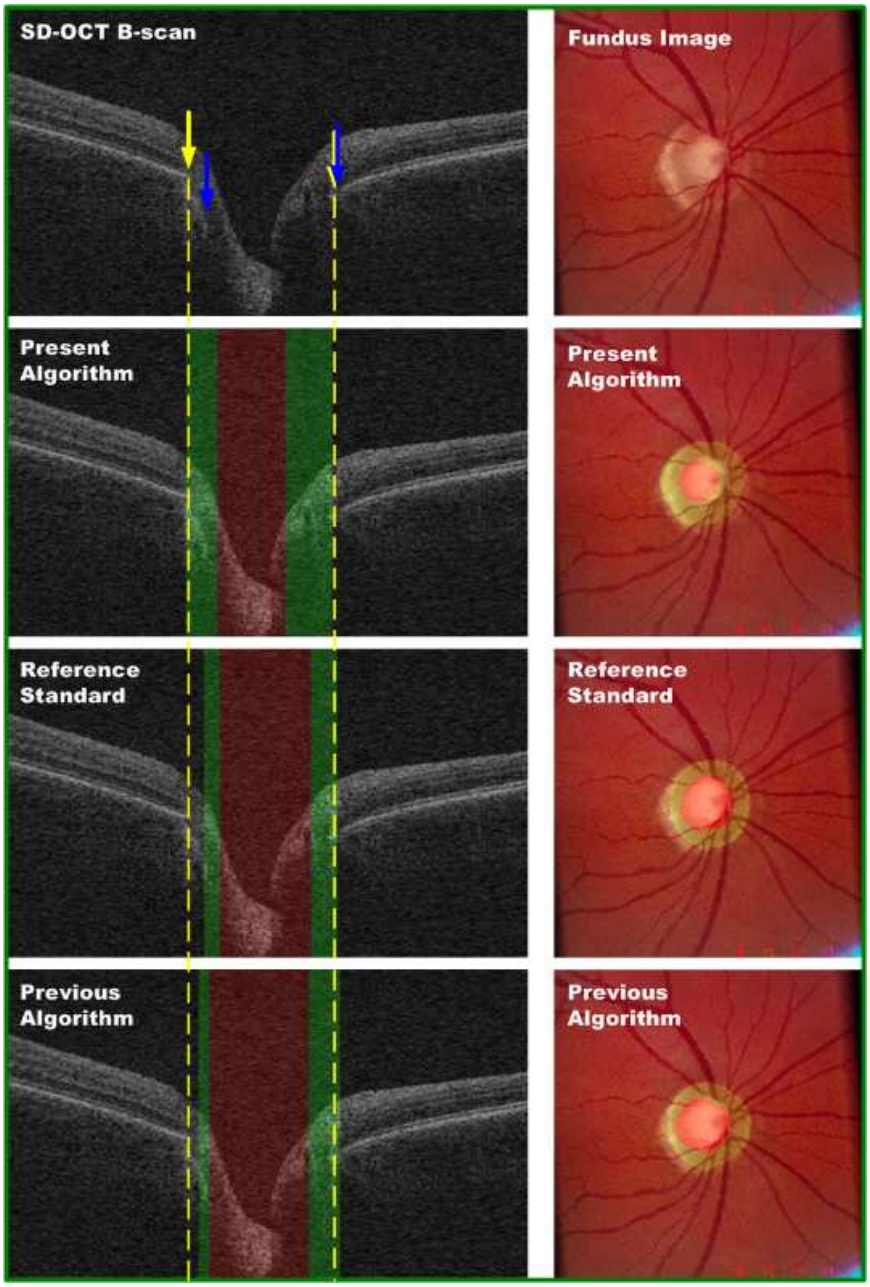

(a)

Figure 4.10: Comparison of present algorithm, expert, and previous algorithm segmentations with discrepancy. Raw SD-OCT and corresponding fundus image (row 1), present algorithm (row 2), RS (row 3), and previous algorithm (row 4) segmentations overlapping with raw SD-OCT and corresponding fundus image. SD-OCT central B-scan (left). Fundus image (right). Yellow arrows: position of the NCO from the algorithm (dashed yellow line indicates the projected NCO position). Blue arrows: clinical disc from the RS. Green, red: each method's projected rim and cup regions, respectively.

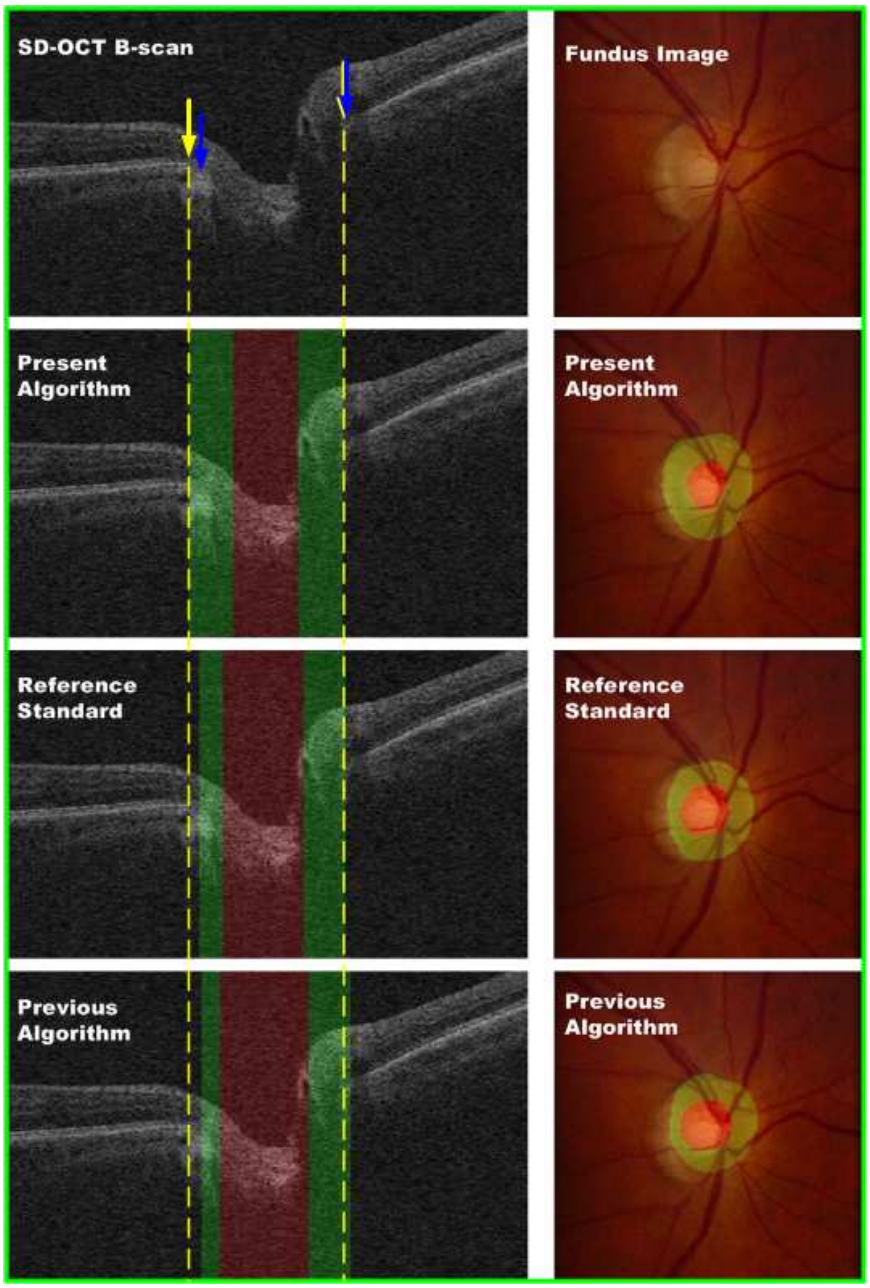

(a)

Figure 4.11: Comparison of present algorithm, expert, and previous algorithm segmentations with discrepancy. Raw SD-OCT and corresponding fundus image (row 1), present algorithm (row 2), RS (row 3), and previous algorithm (row 4) segmentations overlapping with raw SD-OCT and corresponding fundus image. SD-OCT central B-scan (left). Fundus image (right). Yellow arrows: position of the NCO from the algorithm (dashed yellow line indicates the projected NCO position). Blue arrows: clinical disc from the RS. Green, red: each method's projected rim and cup regions, respectively.

4.7.2 Repeatability

Table 4.3: NCO border positioning differences between visits from the 232 scans

Differences	Mean unsigned	Mean signed
(pixels)	1.21 ± 0.57	0.02 ± 0.81
(μm)	36.41 ± 17.06	0.58 ± 24.21

Note: the border positioning differences are measured based on the aligned NCO centers between the two visits.

Table 4.4: NCO area comparison between visits from the 232 scans

	Mean areas				Correlation
	1st visit	2nd visit	Mean signed diff.	Mean unsigned diff.	r
(pixels)	2135 ± 441	2132 ± 433	3.67 ± 134	96.97 ± 92	0.95
(mm^2)	1.92 ± 0.04	1.92 ± 0.39	0.003 ± 0.12	0.087 ± 0.08	(0.93-0.97)

r: Pearson correlation coefficient of the area between the first and second visit (values in parentheses are 95% confidence intervals).

Table 4.3 shows the mean border positioning differences of the NCO between the first and second visits (Section 4.4.2) for the 232 eyes of the 58 patients. The mean unsigned and signed differences are 1.21 ± 0.57 pixels (36.41 ± 17.06 μm) and 0.02 ± 0.81 pixels (0.58 ± 24.21 μm) respectively. Table 4.4 compares the area of the segmented NCO between the two visits. The mean unsigned and signed area differences are 96.97 ± 92 pixels (0.087 ± 0.08 mm^2) and 3.67 ± 134 pixels (0.003 ± 0.12 mm^2) respectively. The area correlation is 0.95 (0.93-0.97).

The scatter and Bland-Altman plots of the NCO area between the two visits are

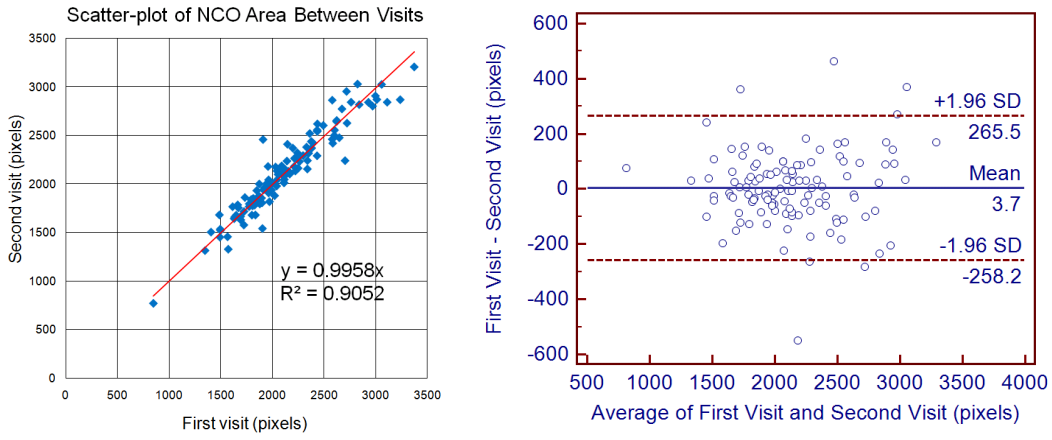

(a) (b)

Figure 4.12: Scatter and Bland-Altman plots of NCO area between visits. (a) Scatter-plot with the linear fitted line (red). (b) Bland-Altman plot. Note: the CR is 262 (1.96*SD) pixels.

illustrated in Fig. 4.12, where the Coefficient of Repeatability (CR) is 262, calculated as 1.96 times the standard deviations (SD) of the differences of the two visits.

4.8 Discussion and conclusions

In this study, 1) we present an algorithm to automatically segment the NCO and optic cup at the RPE/BM plane in SD-OCT volumes. 2) Using human expert planimetry on the stereo photographs as reference standard, we show that the NCO border positioning differences (Table 4.1) between the algorithm and RS for the 68 eyes are as good as inter-observer differences. The linear cup-to-NCO area ratio (Table 4.2) for the 68 eyes correlates reasonably well with the LCDR of the RS (r = 0.85). Other objectively derived 2-D SD-OCT metrics (Table 4.2) correlate reasonably well with those of the RS (r = 0.69-0.83). In addition, we qualitatively (Fig. 4.8 and Fig. 4.9) demonstrate the good match of the present algorithm and RS. We conclude

that in most eyes the NCO in SD-OCT is consistent with the clinically appreciable defined optic disc margin obtained by planimetry. 3) From the repeatability analysis (Table 4.4), a NCO area correlation of 0.95 between visits is obtained. Area and border positioning measurements (Table 4.3 and 4.4) of the NCO are robust across repeated visits and indicate that the NCO may serve as a stable reference landmark for describing structural changes that occur in glaucoma.

However, even though the NCO boundary and clinical disc margin correspond reasonably well in most eyes, it is interesting to note the example discrepancies as well (Fig. 4.10 and Fig. 4.11). These example discrepancies are consistent with the findings reported by Strouthidis *et al.* [4, 5]. In particular, we also find that the clinical disc margin may sometimes correspond to the varying combinations of different structures other than the NCO, such as the border tissue of Elschnig. For instance, in the example SD-OCT B-scan shown in Fig. 4.10, the RS defines the innermost termination of the border tissue as the temporal optic disc margin (blue arrow) and in Fig. 4.11, the RS defines the border tissue as the temporal optic disc margin (blue arrow), which are obviously different from the NCO (yellow arrow) of the algorithm.

Because of such underlying differences, compared with the parameter correlations by planimetry between different experts, the relatively smaller correlations of the NCO-based metrics with those of the RS (Table 4.2) are not surprising. However, the fact that the algorithm demonstrates smaller unsigned border positioning differences than that between the experts (Table 4.1), yet has lower correlations (Table 4.2) is perhaps surprising. This may in part be due to the fact that correlation (measuring the direction and noisiness of linear relationships) does not take into account any bias

(e.g., a consistent over- or under-estimation of a parameter), while the unsigned border positioning errors are influenced by any bias between the measurements. Because the experts tend to have a larger bias than that between the algorithm and RS (as indicated by the signed errors in Table 4.1), this may have contributed to the larger unsigned errors as well. In addition, it is important to note that the definition of the algorithm's "cup boundary" is different from the traditional clinical definition of cup margin. The algorithm simply defines cup as the crossing point of the reference plane with the retinal surface, while the human experts tend to delineate the cup margin at the inflection point of the surface slope of the cup as seen in stereo photographs [60]. This may also explain our observation the cup area at the level of the RPE/BM plane are often smaller than the clinically visible cup area on stereo fundus photographs as seen by human experts (Fig. 4.6).

There are several advantages of the current automated segmentation approach over manual planimetry. 1) Although planimetry is the current gold standard for quantifying glaucoma progression, it introduces a great inter-observer variability [7]. Its subjective nature is one of the potential sources of the inter-observer variability. However, the present automatic algorithm based on SD-OCT is completely objective and therefore, should be more reproducible (assuming the NCO is relatively stable landmark), compared to subjective, manual segmentation by human experts, though this has yet to be rigorously demonstrated. 2) As reported [7], manual segmentation by planimetry is cumbersome and time-consuming and remains as a research tool. However, the algorithm when properly implemented should take just a few minutes to produce the analysis and would be compatible with routine clinical use. 3) As found

by our automated and others' [4,5,61] manual studies, the clinical optic disc margin seems to be the projection of a number of different recognizable anatomic landmarks, introducing a greater variability between experts depending on the landmarks they appreciate to define "their" rim, and thus a great variability for the quantification of glaucoma progression. The landmarks of the NCO will remain the same and therefore are expected to be relatively stable throughout the course of the glaucoma. An ideal reference plane based on a stable structure is critical in longitudinal imaging, glaucomatous and neuropathy analysis of the optic nerve head. The NCO-based reference plane has the potential to more sensitively detect specific glaucomatous ONH changes - such as the alterations in the anterior laminar surface and prelaminar neural tissue internal limiting membrane [4,5]. Although NCO-based metrics cannot replace the clinically appreciated optic disc margin, because the NCO is expected to be stable, it has the potential to provide a basis for other 2-D and/or 3-D ONH parameter quantification and this would aid clinicians to more easily and better interpret the progression of glaucoma. Thus, one of the major advantages of our present approach over our previous voxel classification approach [29] is that the present approach is able to segment natural ONH anatomic structures of NCO and optic cup at the RPE/BM complex to enable all of the advantages such structures may provide (such as the ability to compute 3-D parameters based on a reference plane). In the previous approach, the RS from fundus photographs was used as the ground truth in the training phase for the voxel classification and this resulted in mimicking the subjective assessment of the clinical defined optic disc margin and optic cup seen on photographs. As shown in the examples of Fig. 4.10 and Fig. 4.11, although the segmentation of the

previous approach closely corresponds to that of the RS, it does not overlap with a single constant structure in SD-OCT volumes. However, our core hypothesis, i.e., that segmentation of NCO will allow a better estimation of glaucoma progression, than the voxel-classification based approach needs to be tested and this is only possible in a prospective study of sufficient duration.

There are several limitations in this study. 1) Close-to-isotropic SD-OCT volumes are used in this study. Potentially, a fully isotropic SD-OCT can lead to more accurate segmentation and corresponding parameter measurements. The 2-D measurements of this work are not substantially influenced because they are computed on an isotropic XY plane. However, for future volumetric measurements, if applicable, it may be desirable to compute the volumetric parameters in the isotropic OCT space. 2) The flattening of the raw SD-OCT greatly improves the motion artifacts and also provides an ability to correspondingly compare the NCO-based 2-D metrics to those 2-D metrics of the clinical optic disc margin. However due to the layer segmentation errors, it is not perfect as shown in Fig. 4.2. For the 2-D measurements on the NCO-aimed OCT projection image, we correct the non-optimal flattening problem by extrapolating the average radial positions outside the estimated NCO to those of inside NCO (Section 4.5.2). But for the volumetric measurements, it might be necessary to transform the NCO-based reference plane back to the original raw SD-OCT space and compute the volumetric parameters in the non-flattened isotropic space. 3) As reported [17], with the glaucomatous damage of the lamina cribrosa and peripheral scleral connective tissue, the cup enlarges and the NCO position may change relative to the peripheral sclera. Strouthidis *et al.* has suggested an alternative

reference plane that is further away from the "center" of the NCO boundary [4]. This alternative reference plane can be obtained in a fixed distance from the segmented NCO and is less likely to deform posteriorly. Such change in reference plane position can be readily implemented in our algorithm, if desired. 4) The large vessels crossing the NCO boundary could cause the NCO segmentation errors.

In summary, in this work, we develop a novel automated graph-search-based machine algorithm to segment the NCO and optic cup at the level of RPE/BM complex in 3-D OCT volumes of the ONH. In most eyes, the algorithm parameters correlate well with the RS parameters from manual planimetry. However, a small discrepancy exists between the NCO and the clinical disc margin in some eyes. Based on the reproducibility analysis, the algorithm segmentation is robust across repeated visits. Because of the relative stability of the NCO reference plane and objective nature of the automated algorithm, we predict that the measurements of the NCO-based 2-D and/or 3-D glaucomatous parameters in volumetric OCT would be more reproducible than those of the RS parameters based on fundus photographs or even the OCT parameters of the previous generation time-domain OCT.

However, as mentioned above, our NCO segmentation approach is not perfect. To further improve our algorithm, we develop a 3-D wavelet-transform-learning-based NCO segmentation approach by focusing on the enhancement of the cost function design for graph searching of the intraretinal layers and NCO as presented in the next chapter (Chapter 5) and extend our algorithm to the application on the non-human primate eyes.

CHAPTER 5
3-D WAVELET-TRANSFORM-LEARNING-BASED NEURAL CANAL OPENING SEGMENTATION IN SD-OCT VOLUMES OF NON-HUMAN PRIMATE EYES

5.1 Chapter abstract

The neural canal opening (NCO) is a three-dimensional anatomic structure marking the end of the retinal pigment epithelium/Bruch's membrane (RPE/BM) complex of the optic nerve head (ONH) in spectral-domain optical coherence tomography (SD-OCT) volumes. Prior automated NCO segmentation approaches have only been validated via comparison with manual tracings of the clinical disc margin from fundus photographs rather than via direct comparison of the structure within SD-OCT volumes. Furthermore, the algorithms have only been applied to human eyes, but it is important that segmentation approaches are developed for use within non-human primate eyes as well. In addition, because of the dependence of NCO segmentation algorithms upon the ability to accurately segment the layers of the RPE/BM complex near the NCO, existing approaches will sometimes fail if these layers are not segmented accurately. The retinal vessels crossing the NCO can also cause NCO segmentation errors. Thus, in this work, we develop a 3-D graph-theoretic approach for segmenting the NCO in SD-OCT volumes of non-human primate eyes based on the 3-D wavelet-transform-learning-based layer segmentation. More specifically, a lifting scheme wavelet transform is applied on the SD-OCT volumes and the wavelet transform is learned using a genetic algorithm based on three segmented surfaces around the RPE/BM complex. Based on the learned layer segmentation, an OCT projection image around the RPE/BM complex is created and the 2-D NCO is pre-segmented

using a graph theoretic approach. A supervised pixel-classification-based approach is applied to segment the vessels by incorporating the pre-segmented NCO locational information. The pre-segmented vessel information is iteratively incorporated to the cost function of the graph searching of the NCO to obtain a better NCO segmentation. The segmented 2-D NCO is projected to a surface at the RPE/BM complex to obtain the 3-D NCO points. The developed algorithm is tested on two types of SD-OCT volumes by comparing the segmented 3-D NCO points with the manual delineation directly from the SD-OCT volumes. The 3-D mean unsigned and signed border positioning differences for the 9 test scans of the first type SD-OCT volumes are 5.30 $\pm$ 1.42 voxels (60.74 $\pm$ 11.52 μm) and 1.17 $\pm$ 0.97 voxels (19.25 $\pm$ 14.61 μm) respectively and that of 2-D are 3.33 $\pm$ 0.51 pixels (57.10 $\pm$ 11.88 μm) and 1.02 $\pm$ 0.58 pixels (19.24 $\pm$ 14.25 μm) respectively; for the 8 test scans of the second type SD-OCT volumes, the 3-D mean unsigned and signed border positioning differences are 5.38 $\pm$ 1.91 voxels (43.11 $\pm$ 15.60 μm) and 2.69 $\pm$ 1.68 voxels (24.51 $\pm$ 17.61 μm) respectively and that of 2-D are 3.68 $\pm$ 1.21 pixels (39.00 $\pm$ 14.68 μm) and 2.19 $\pm$ 1.41 pixels (23.42 $\pm$ 17.37 μm) respectively. Both the quantitative and visual results demonstrate a great agreement between the automated segmentation and the manual delineation.

5.2 Introduction

In Chapter 4, we presented an automated 3-D NCO segmentation approach in SD-OCT volumes of human eyes [35, 36], in which we found that the clinical optic disc margin on fundus images may correspond to a few anatomic structures, consistent

with the findings of Strouthidis *et al.* [4]. The NCO, however, was a single constant anatomic structure and is detectable in SD-OCT volumes.

However, due to the limitation of availability of the ground truth directly from the volumetric SD-OCT scans of human eyes, in the previous NCO segmentation, the algorithm was validated by comparing the automated segmentation with the expert tracings of the clinical disc margin from the manual planimetry. Ideally, a direct comparison of the automated NCO segmentation with the manual delineation of the NCO directly from SD-OCT volumes is desirable because of the discrepancy of the NCO and the clinical optic disc margin.

In addition, our previous NCO segmentation utilized a graph search approach finding the optimal solution for the multiple retinal surface and NCO segmentation in a low-polynomial time [11]. It in general performed well. However, it is known that the optimal solution of the graph search is highly dependent on the designed cost function. The cost function was simply a signed edge-based term in the original image space for both the involved 3-D retinal layer and NCO boundary segmentation. The surface and NCO segmentation errors occurred in some scans when high frequency noise exists, interrupted objects (such as large vessels) are present, and/or strong edge information is missing.

This work is a subsequent study of the previous NCO segmentation with a few aims as follows: 1) to compare our automated algorithm to the manual delineation directly from SD-OCT volumes, 2) to adapt it to work with non-human primate eyes, 3) to enhance the algorithm to more robustly deal with potential retinal layer segmentation issues, and 4) to further verify the constant anatomic nature of the

NCO structure.

As mentioned in Chapter 3, the wavelet transform provides a great ability to selectively utilize the desired coarse or fine image features. Quellec *et al.* [40] reported an adaptive nonseparable 2-D lifting-scheme-based wavelet transform and recently, they extended their 2-D wavelet transform to 3-D [9].

Thus, in this specific work, we propose to use the 3-D lifting-scheme-based wavelet transform to select the desired frequency subbands by an optimization approach of genetic algorithm [62, 63] to improve the 3-D retinal layer segmentation and hence to improve the 3-D NCO segmentation because the NCO segmentation is highly dependent on the layer segmentation.

In addition, the NCO segmentation errors could occur in the cases that the large vessels cross over with it. We thus pre-segment the retinal vessels using our single modal OCT vessel segmentation approach (Chapter 6) [52] and incorporate the pre-identified vessel positional information to the cost function design of the graph searching of the NCO to remedy the NCO segmentation difficulty due to the presence of large vessels [64].

5.3 Data

23 optic nerve head centered non-human primate normal eyes are used in this study. All animals were treated in accordance with the ARVO statement for the use of animals in ophthalmic and vision research. All eyes were imaged in vivo using a raster pattern from Heidelberg Spectralis 3-D SD-OCT at Devers Eye Institute (Legacy Health System, Portland, Oregon). Among the 23 SD-OCT scans, 12 of

them consist of 768 (A-scans) × 145 (B-scans) × 469 voxels (referred to as the first type SD-OCT volumes) from 12 non-human primates with 11 left and one right eyes. 11 of them consist of 768 (A-scans) × 290 (B-scans) × 469 voxels (referred to as the second type SD-OCT volumes) from 11 non-human primates with 6 left and 5 right eyes. The data of each type is further split into the training set and test set. For each type, three of them with two left eyes and one right eye are utilized for the training of the retinal layer segmentation and the remaining scans are used as the test set. Thus the first type has 9 and the second type has 8 test scans.

5.4 Methods

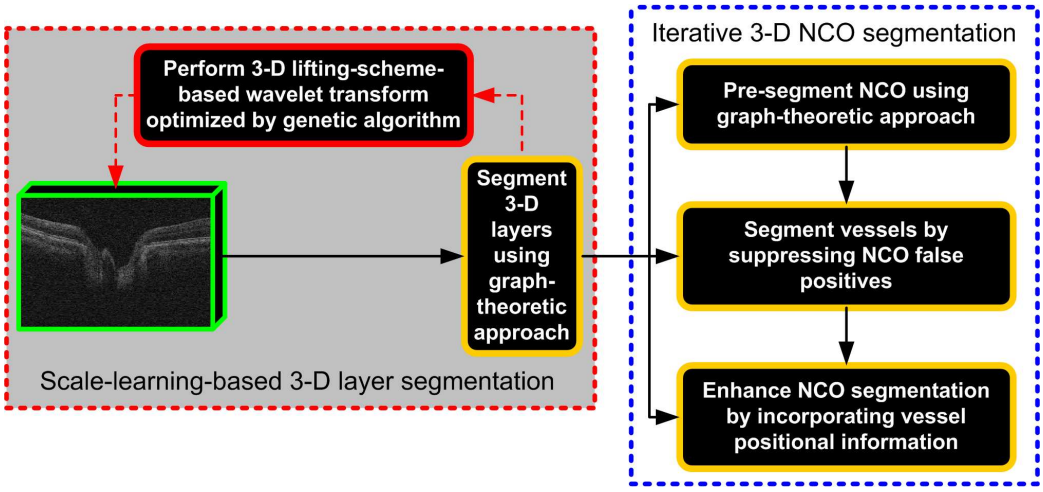

Figure 5.1: Flowchart of the major steps of the 3-D wavelet-transform-learning-based NCO segmentation.

As illustrated in Fig. 5.1, the algorithm starts from the 3-D retinal layer segmentation in the volumetric SD-OCT scans using a graph search approach. To obtain

a better retinal layer segmentation at the RPE/BM complex, we learn the wavelet transform tuned by the genetic algorithm (Section 5.4.1). Based on the segmented layers around the RPE/BM complex, an OCT projection image is created and the 2-D NCO is pre-segmented on the OCT projection image using a graph theoretic approach. To suppress the segmentation errors due to the presence of the large blood vessels on the OCT projection image, we segment them using our single modal OCT vessel segmentation approach (Chapter 6) [52]. The 2-D NCO is then obtained based on the vessel-suppressed cost function [64] and projected to a segmented surface at the RPE/BM complex to obtain the 3-D NCO points (Section 5.4.2). Fig. 5.1 illustrates the major processing steps of the developed approach with the further details provided in the following paragraphs.

5.4.1 3-D wavelet-transform-learning-based layer segmentation

The NCO segmentation is highly dependent on the accurate layer segmentation at the RPE/BM complex as the NCO is located at the end of the RPE/BM complex. To obtain a better solution of the 3-D layer segmentation at the RPE/BM complex, we iteratively learn the wavelet transform to minimize the distance between the segmented and manually traced retinal layers as illustrated in Fig. 5.2.

More specifically, the learning process starts from applying a set of randomly assigned wavelet transform coefficients on the original SD-OCT volume. An edge cost function is obtained from the wavelet transformed image using a Sobel operator. The graph search is applied for multiple layer segmentation. By optimizing (minimizing) the fitness criterion based on the layers around the RPE/BM complex using a genetic

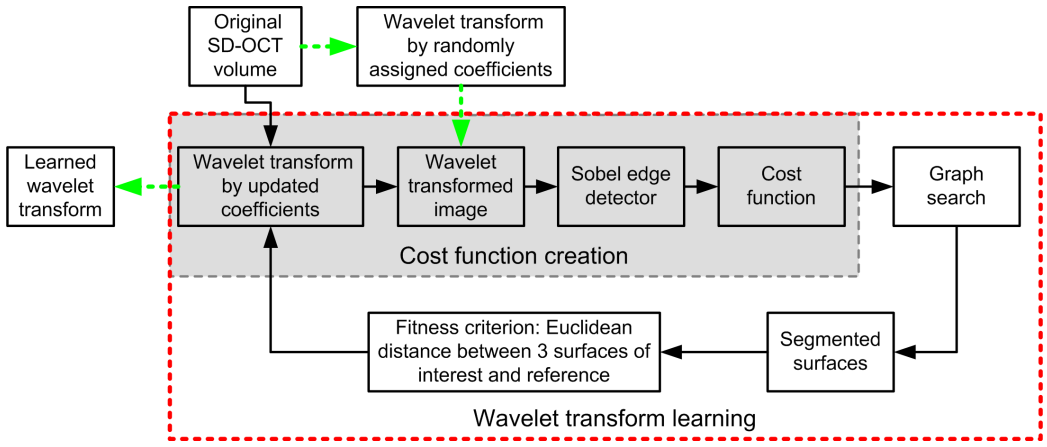

Figure 5.2: Major steps of the wavelet transform learning process.

algorithm, in the next generation, the wavelet transform coefficients are updated and continuously applied on the original SD-OCT volume to obtain a new wavelet transformed image for the multiple layer segmentation. Iteratively, a better layer segmentation is obtained.

To make the whole process clearer, the major steps of the layer segmentation are separately described in Section 5.4.1.1. The details of the wavelet transform learning are provided in Section 5.4.1.2.

5.4.1.1 Major steps of layer segmentation

For computational efficiency, the 3-D retinal layer segmentation is performed by the graph searching based on a multi-stage approach.

1) The wavelet-transformed SD-OCT volumes (the wavelet transform optimized as described in Section 5.4.1.2) are downsampled by two in x-direction for the first type scans and by two in both x- and y-direction for the second type scans. 2) To find the layers of interest around the RPE/BM complex, the SD-OCT volumes are

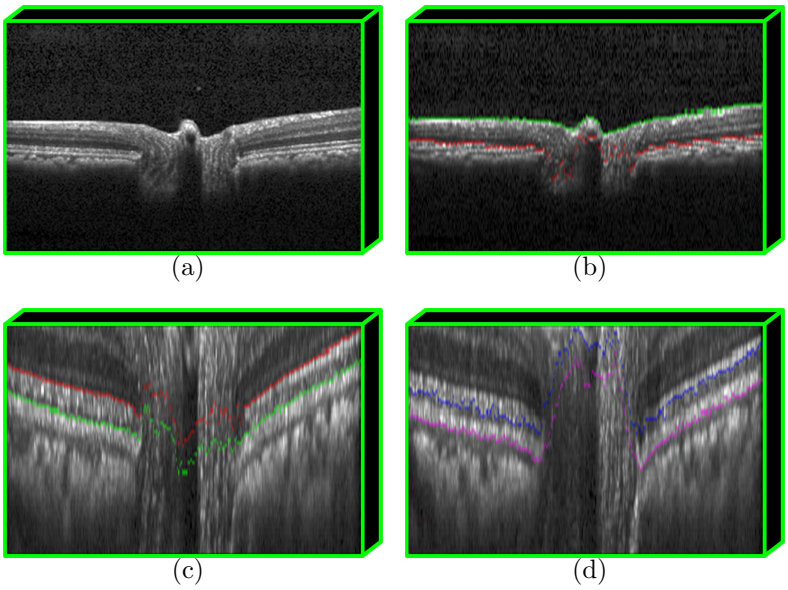

Figure 5.3: Illustration of 3-D retinal layer segmentation. (a) Original raw SD-OCT volume. (b) two segmented surfaces on the downsampled SD-OCT volume in z-direction (also in x direction) overlapping with the central slice of the SD-OCT volume. Four surfaces segmentation at the RPE/BM complex with c) two segmented surfaces with the edge cost function favoring the black to white transition, and d) two segmented surfaces with the edge cost function favoring white to black transition, overlapping with the central slice of the SD-OCT ROI subvolume, respectively.

further downsampled in z-direction. Two surfaces, i.e. the internal limiting membrane (green line indicated surface in Fig. 5.3.b) and the surface between the inner and outer segments of the photoreceptors (red line indicated surface in Fig. 5.3.b), are simultaneously segmented using the edge cost function favoring a black to white transition. A region of interest (ROI) of the RPE/BM complex is then defined in the x- and/or y-downsampled SD-OCT volumes but with the full z resolution (referred as the full-z-resolution-downsampled SD-OCT volumes) based on the segmented second surface. More specifically, the ROI is defined as that from a horizontal flat surface with a few voxels above the highest point of the second surface to a horizontal flat surface

with 80 voxels below the upper surface in the full-z-resolution-downsampled SD-OCT volumes. Note that when computing the highest point, an estimated central region is excluded due to the large variation of the layer segmentation. 3) In the extracted ROI subvolume around the RPE/BM complex, two surfaces, i.e. the surface between the inner and outer segments of the photoreceptors (red line indicated surface in Fig. 5.3.c) and the inner boundary of the RPE/BM complex (green line indicated surface in Fig. 5.3.c) with the edge cost function favoring a black to white transition, and two surfaces, i.e. the outer segments of the photoreceptors (blue line indicated surface in Fig. 5.3.d) and the outer boundary of the RPE/BM complex (purple line indicated surface in Fig. 5.3.d) with the edge cost function favoring a white to black transition are further simultaneously segmented. 4) The segmented four surfaces at the RPE/BM complex are then interpolated to the original SD-OCT space using the thin plate spline [12]. Fig. 5.3 is an example illustration of the 3-D retinal layer segmentation.

5.4.1.2 Learning of wavelet transform

The 3-D wavelet transform provides a 3-D multi-resolution analysis which decomposes the input signal x (volumetric SD-OCT image $I(x, y, z)$) into L ($L = 4$ in this work) levels. The wavelet transform used in this work is based on the lifting scheme [9, 40]. More specifically, the filter bank consists of a set of linear prediction (P_i) and update (U_i) filters with $i = 1...M$. In each level, the wavelet transform involves downsampling the signal by a three-dimensional dilation matrix D with $M = |det(D)|$. The input lattice $\mathbb{Z}^3$ is mapped to M sub-lattices $T_i = D \cdot \mathbb{Z}^3 + t_i$,

$t_i \in \mathbb{Z}^3$, $t_0 = 0$, $i = 0...M-1$, where T_0 contains the approximation a of the signal and T_i, $i = 1...M-1$, contain its details d_i along direction t_i. For the aim of computational efficiency, the diagonal matrix $D = 2 \cdot I$ $(M = 2^3)$ is used to generate the separable lattices of $T_0, ..., T_{M-1}$.

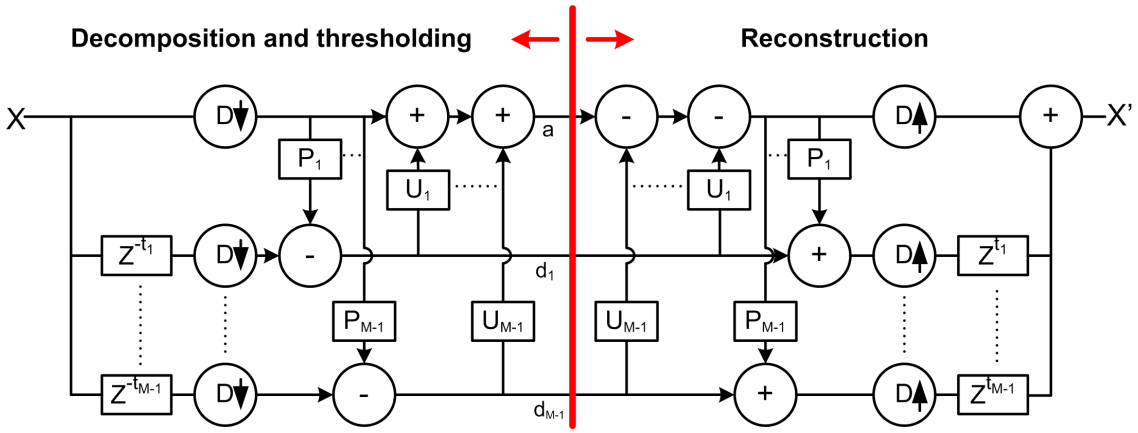

Figure 5.4: Illustration of M-band lifting scheme filter bank with $t_0 = 0$. Adapted from [9, 40].

For the recursive signal analysis, the approximation a is further decomposed using the same filter bank until the desired scale L is reached. More specifically, the initial wavelet transform coefficients at level $L = 1$ with the resolution of M^j $(j = 0)$ lie in the lattice $T_0^{(0)} = \mathbb{Z}^3$. The coefficients of the approximation at the resolution of M^j lie in the lattice $T_0^{(j)} = D^j \cdot \mathbb{Z}^3$. The coefficients of the approximation at the resolution of M^{j+1} lie in the lattice $T_0^{(j+1)} = D^{j+1} \cdot \mathbb{Z}^3$ and the details lie in the lattice $T_i^{(j+1)} = D^{j+1} \cdot \mathbb{Z}^3 + D^j \cdot t_i$, $i = 0...M-1$. The left side of Fig. 5.4 illustrates the decomposition of the wavelet transform via the lifting scheme.

Three surfaces around the RPE/BM plane are utilized for the learning of the

wavelet transform. More specifically, the surface between the inner and outer segment of the photoreceptors, the inner, and outer boundary of the RPE/BM complex, are manually traced by the author (*Z. Hu*) from three randomly chosen SD-OCT volumes of each image type and are used as the reference. The region inside the estimated NCO is excluded to the learning process due to the large variation of the layer segmentation in that region (Fig. 5.5.a).

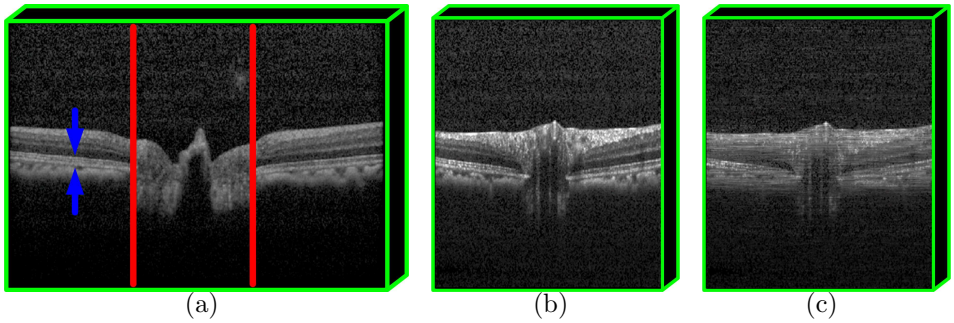

Figure 5.5: Illustration of the learning of wavelet-transform-based layer segmentation. (a) Learning region around the RPE/BM complex as indicated by the blue arrows. Note that the central estimated NCO region (inside the red line) is excluded from the computation of the fitness criterion due to the large variation of layer segmentation. (b-c) The full-z-resolution-downsampled SD-OCT volume without and with applying the learned wavelet transform respectively.

The genetic algorithm is utilized because it is a quick and popular optimization approach for finding the rough estimations of the best solutions. Jones *et al.* [62] have proposed to use the genetic algorithm to find the predict and update filters of the lifting-scheme-based wavelet transform. The major advantage of the genetic algorithm over the descent optimization algorithm is that it does not need an initial

solution.

The fitness criterion is the summation of the Euclidean distance between the segmented and manually traced surfaces along z-direction for all the three surfaces. The genetic algorithm optimizes (minimizes) the Euclidean distance summation by thresholding the undesirable high frequency content (e.g. the speckle noise) and low frequency information (e.g. small details) of the input signal based on tuned wavelet coefficients. In each of the decomposed level, each transformed coefficient c that is smaller than the learned threshold t is set to 0, the others are updated as follows: $c = c - t$. After removing the undesirable frequency content, the output signal x' (volumetric SD-OCT image $I'(x, y, z)$) is reconstructed using the thresholded coefficients as illustrated in the right side of Fig. 5.4. The learning-based edge cost function is obtained from the reconstructed image and the graph-based multilayer segmentation is applied. Iteratively a better layer segmentation is obtained.

After the learning process, the obtained wavelet transform for each type of SD-OCT volumes is then applied on the remaining test scans. Fig. 5.5.a illustrates the learning region of the wavelet-transform-based layer segmentation and Fig. 5.5.b and c provide an example of a SD-OCT volume and its reconstructed image after applying the wavelet transform.

5.4.1.3 OCT projection image creation

Based on the wavelet-transform-learned retinal layer segmentation, a small number of slices around the inner boundary of the RPE/BM complex (light green line indicated surface in Fig. 5.6.a and d) with three voxels above and seven voxels be-

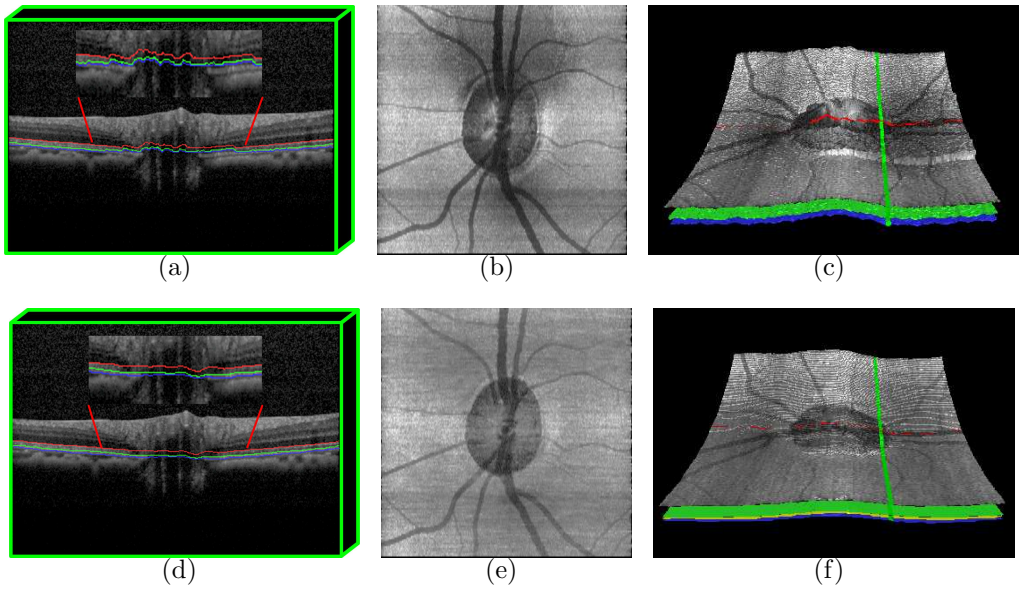

Figure 5.6: Example illustration of the wavelet-transform-learning-based layer segmentation and OCT projection image. (a,d) Three segmented surfaces at the RPE/BM complex without and with applying the wavelet transform overlapping with the original full resolution SD-OCT volume respectively. (b,e) Isotropic SD-OCT projection images without and with applying the wavelet transform respectively. (c,f) 3-D rendering of the surface segmentation without and with applying the wavelet transform by mapping the OCT projection image texture onto the top surfaces. Especially note the layer segmentation errors at the highlighted region in a, the fuzzy region at the upper side of the OCT projection image in b, and the layer segmentation errors illustrated by the 3-D surface rendering at the right side of c (rotating the projection image about 90 degree clockwise) without applying the wavelet-transform-learning-based edge cost function and the improvement in the corresponding figures of d, e, and f with applying the wavelet-transform-learning-based edge cost function.

low it are taken to create the OCT projection images. The OCT projection images are used for the 2-D NCO segmentation. Thus the wavelet-transform-learning-based OCT projection images provide an ability to better define the NCO. Note that the OCT projection images are anisotropic for both the first type and second type SD-OCT volumes. To perform the graph searching of the NCO boundary, the anisotropic images are rescaled to isotropic images. An example comparison of the layer segmen-

tation and consequent OCT projection images without and with applying the wavelet transform is shown in Fig. 5.6.

5.4.2 3-D NCO segmentation

The 3-D NCO is segmented as follows. First, the 2-D NCO is pre-segmented on the OCT projection images using a graph theoretic approach. The retinal vessels are segmented using the vessel segmentation approach with the incorporation of the pre-segmented NCO positional information as presented in Chapter 6 [52]. Based on the segmented vessel profiles, a vessel-suppressed edge cost function is then utilized to improve the 2-D NCO segmentation. The segmented 2-D NCO points are then projected to a surface at the RPE/BM complex to obtain the 3-D NCO position.

More specifically, to perform the 2-D NCO segmentation, the isotropic OCT projection images are first transformed from Cartesian coordinates to polar coordinates. The edge-based cost function favoring a dark-to-bright transition in the vertical direction (corresponding to the radial direction in Cartesian coordinates) is obtained from the transformed polar projection images. The 2-D NCO is pre-segmented from the polar cost function using a single boundary graph search approach.

The vessel distribution near the NCO causes difficulties for the segmentation of the NCO. To remedy this problem, a pixel-classification-based segmentation method as described in Chapter 6 is used to segment the vessels on the isotropic OCT projection images in Cartesian coordinates by incorporating the pre-segmented NCO positional information into the classification process. The segmented vessel images are then transformed to polar coordinates. The polar edge cost function is modified according

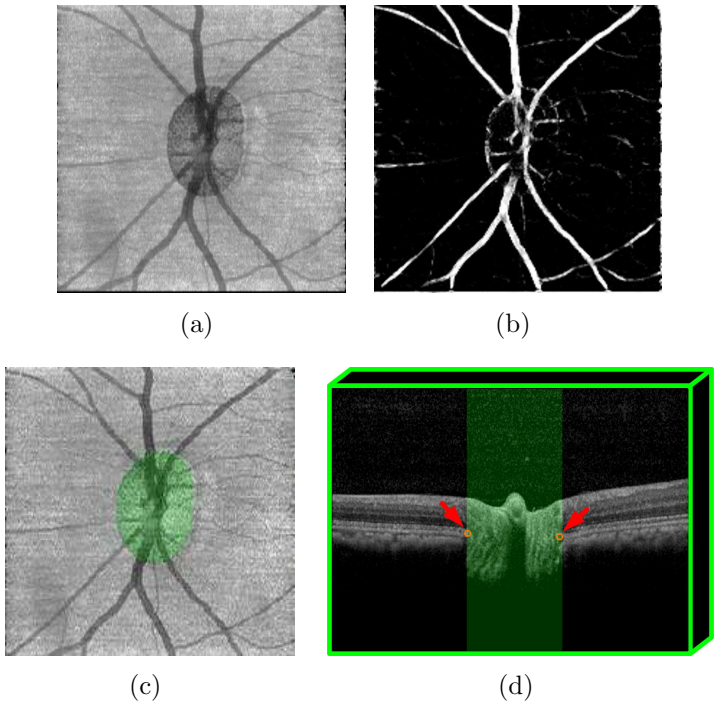

Figure 5.7: Illustration of the NCO segmentation. (a) Isotropic wavelet-transform-learning-based OCT projection image. (b) Vessel segmentation. (c) 2-D NCO segmentation (border of the green color ellipse) overlapping with the OCT projection image. (d) 3-D NCO segmentation (projected green strip) and manual delineation (orange circles indicated by the red arrows) overlapping with the central slice of the SD-OCT volume.

to the vessel location information, i.e. the costs of vessel locations in the polar OCT projection images are interpolated by the mean value of the surrounding non-vessel costs in the horizontal direction. The more accurate 2-D NCO is identified based on the modified polar edge cost function using the graph search and transformed back to the Cartesian coordinates and rescaled to anisotropic space. The 3-D NCO are obtained by projecting the transformed 2-D NCO points to a surface at the RPE/BM complex by averaging the z values of the segmented inner and outer boundary at the RPE/BM complex. Fig. 5.7 is an example illustration of the segmented retinal vessels,

2-D NCO, and 3-D NCO boundary.

5.5 Validation

The manual delineation of the 3-D NCO points were performed at Devers Eye Institute using the radially interpolated B-scans at 4.5 degree intervals generated from "grid" B-scan acquisitions of the SD-OCT volumes [4]. Within each radial section, the delineator marked the NCO on either side of the neural canal. Totally 80 3-D NCO points were delineated for each volume and the Cartesian coordinates for each delineated point were saved.

The segmented 3-D NCO boundary is compared to the manual delineation using three measures: 1) 3-D mean unsigned and signed border positioning differences, i.e. the 3-D closest Euclidean distances between the manually delineated and segmented 3-D NCO points. The 3-D signed difference is measured with respect of the center of the manually delineated points in the x- and y-direction. If the Euclidean distance of the segmented NCO points in x- and y-direction to the center of the manually delineated points is greater than that of the manually delineated point to its center, the 3-D signed difference is positive, and vice versa; 2) 2-D mean unsigned and signed border positioning differences, i.e. the 2-D Euclidean distance in x- and y-direction between the manually delineated and segmented 3-D NCO points with the closest 3-D Euclidean distances. The 2-D signed difference is defined in the same way as the 3-D signed difference, i.e. if the 2-D Euclidean distance of the segmented NCO points in x- and y-direction to the center of the manually delineated points is greater than that of the manually delineated point to its center, the 2-D signed difference is positive,

and vice versa; and 3) mean unsigned and signed border positioning differences in z-direction, i.e. the distance of z-direction between the manually delineated and the segmented NCO points with the closest 3-D Euclidean distances. For the signed difference, if the z-value of the segmented NCO point is greater than the z-value of the center of the manually delineated points, i.e. the segmented NCO point is below the center of the manually delineated points, the signed difference is positive, and vice versa.

5.6 Results

Table 5.1: Mean border positioning differences of the wavelet-transform-learning-based 3-D NCO segmentation and manual delineation for all the test SD-OCT scans

	3-D 2-D, z	Mean unsigned (voxels) (pixels)	Mean signed (voxels) (pixels)	Mean unsigned (μm) (μm)	Mean signed (μm) (μm)
First type (9 scans)	3-D	5.30 ± 1.42	1.17 ± 0.97	60.74 ± 11.52	19.25 ± 14.61
	2-D	3.33 ± 0.51	1.02 ± 0.58	57.10 ± 11.88	19.24 ± 14.25
	z-direction	3.49 ± 1.49	-2.12 ± 2.26	13.51 ± 5.77	-8.19 ± 8.75
Second type (8 scans)	3-D	5.38 ± 1.91	2.69 ± 1.68	43.11 ± 15.60	24.51 ± 17.61
	2-D	3.68 ± 1.21	2.19 ± 1.41	39.00 ± 14.68	23.42 ± 17.37
	z-direction	3.23 ± 1.63	-0.67 ± 2.37	12.49 ± 6.31	-2.61 ± 9.18

3-D: 3-D NCO border positioning differences.

2-D: 2-D NCO border positioning differences in x- and y-direction.

z-direction: NCO border positioning differences in z-direction.

Table 5.1 shows the 3-D and 2-D mean border positioning differences and mean border positioning differences in z-direction between the wavelet-transform-learning-based NCO segmentation and the manual delineation for both the first type and

second type SD-OCT volumes.

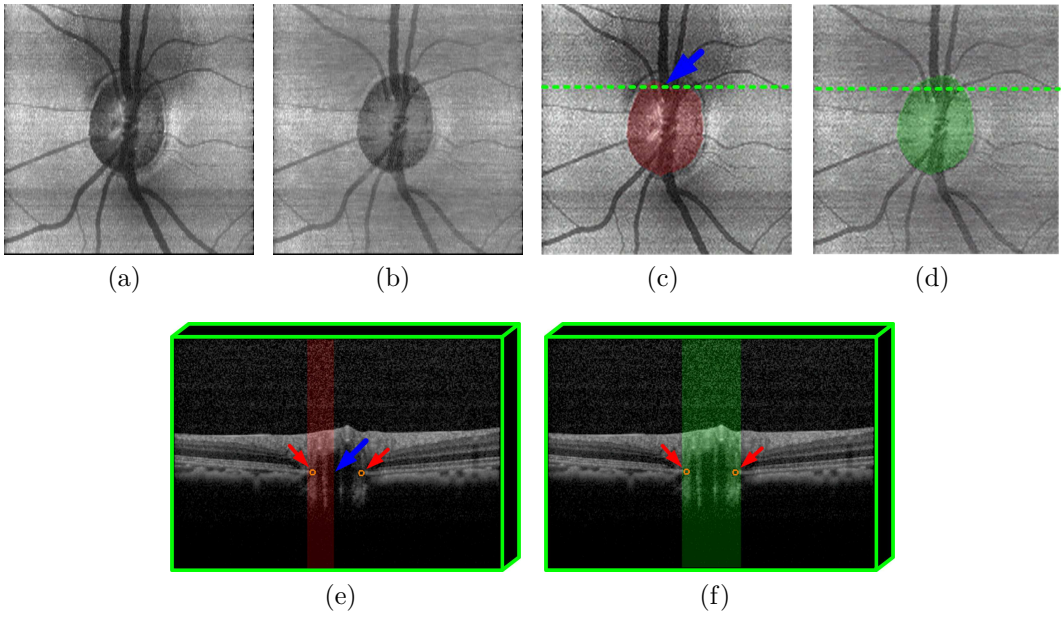

Figure 5.8: Comparison of the 3-D NCO segmentation without and with applying wavelet transform. (a-b) Isotropic OCT projection image obtained from the segmented layers without and with wavelet transform respectively. (c-d) 2-D non-wavelet-transform-based NCO segmentation (border of the red color ellipse) and wavelet-transform-learning-based NCO segmentation (border of the green color ellipse) overlapping with their OCT projection images respectively. (e-f) 3-D non-wavelet-transform-based NCO segmentation (red strip), wavelet-transform-learning-based NCO segmentation (green strip), and manually delineated NCO points (orange circles indicated by the red arrows) overlapping with an OCT slice located at the position indicated by the green lines in c and d. Especially note the segmentation errors of the non-wavelet-transform-based NCO segmentation as shown in c and e, for instance, at the position indicated by the blue arrows and the improvement by the wavelet-transform-learning-based NCO segmentation in d and f.

Fig. 5.8 is a visual example comparison of the algorithm segmentation of the NCO without and with application of the wavelet transform. Especially note the NCO segmentation errors as shown in Fig. 5.8.c and e without applying the wavelet

transform and the improvement with applying the learning-based wavelet transform as shown in Fig. 5.8.d and f.

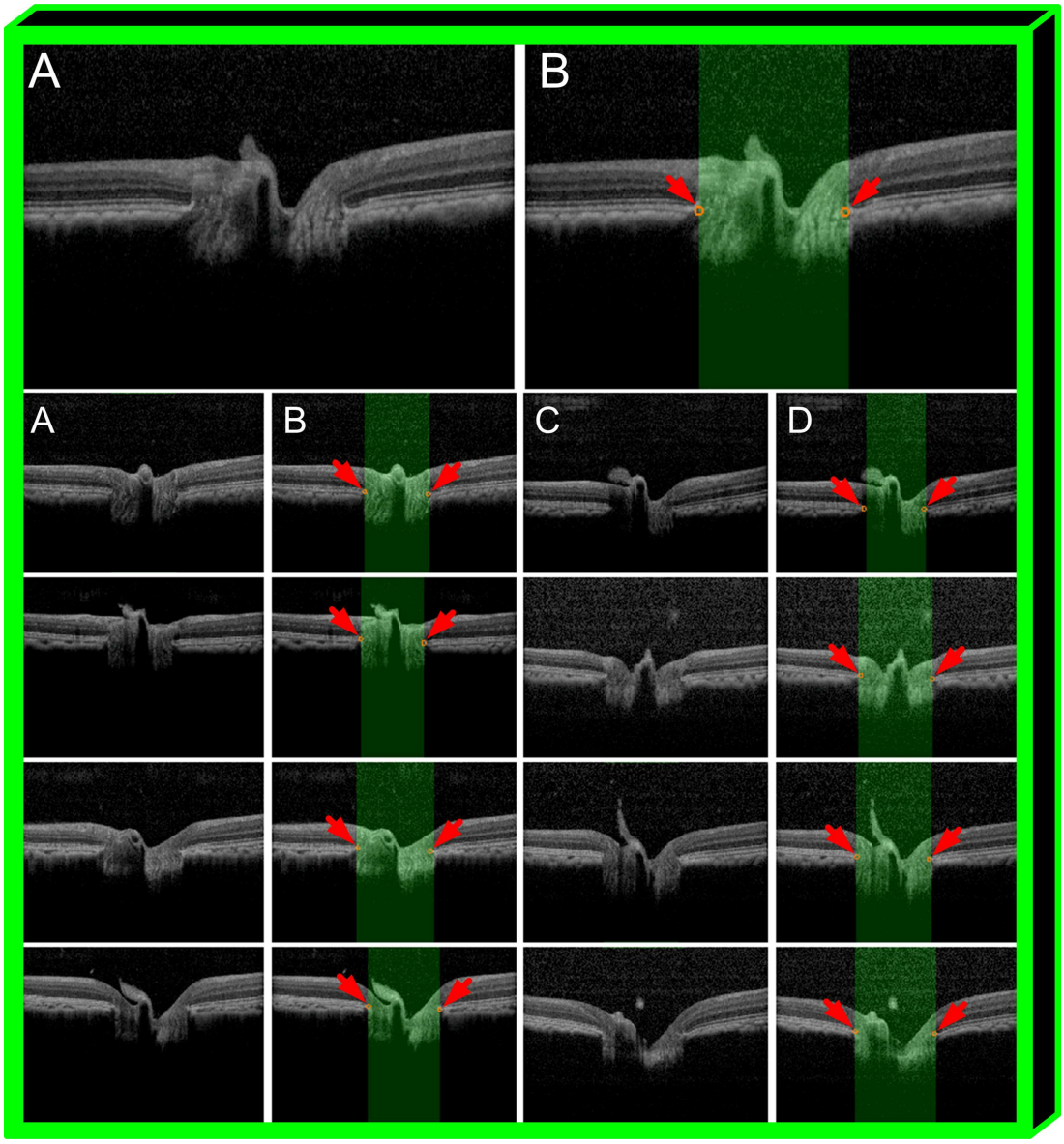

Figure 5.9: 3-D wavelet-transform-learning-based NCO segmentation for the 9 test scans of the first type SD-OCT volumes. (A,C) Original SD-OCT scans. (B,D) Comparison of 3-D wavelet-transform-learning-based NCO segmentation (projected green strip) and manual delineation points (orange circles indicated by the red arrows). Note that the 3-D green box for the overall figure is to address that the NCO segmentation is a 3-D segmentation performed in each volumetric SD-OCT scan.

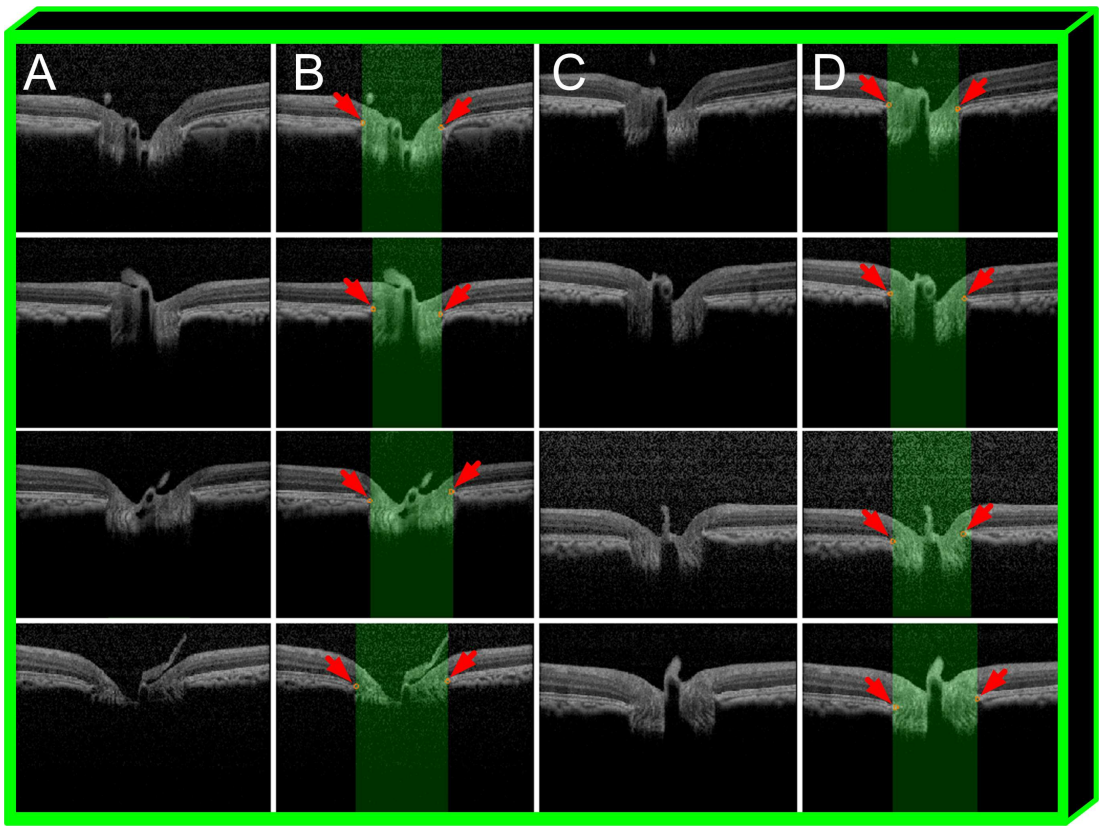

Figure 5.10: 3-D wavelet-transform-learning-based NCO segmentation for the 8 test scans from the second type SD-OCT volumes. (A,C) Original SD-OCT scans. (B,D) Comparison of 3-D wavelet-transform-learning-based NCO segmentation (projected green strip) and manual delineation points (orange circles indicated by the red arrows). Note that the 3-D green box for the overall figure is to address that the NCO segmentation is a 3-D segmentation performed in each volumetric SD-OCT scan.

Fig. 5.9 is a visual comparison of the wavelet-transform-learning-based NCO segmentation (projected green strip in column B and D) with the manual delineation (orange circles in column B and D indicated by the red arrows) of the 9 test scans from the first type SD-OCT volumes and Fig. 5.10 is that of the 8 test scans from the second type SD-OCT volumes.

5.7 Discussion and conclusions

In this study, we present an automated 3-D wavelet-transform-learning-based graph theoretic approach to segment the NCO in SD-OCT volumes with the application on non-human primate eyes. To our knowledge, this is the first such algorithm to utilize the scale-learning-based edge cost function for obtaining a better 3-D layer segmentation and hence a better OCT projection image for the segmentation of the 3-D NCO boundary in SD-OCT volumes. In addition, the pre-segmented vessel location information is incorporated in the edge cost function of the NCO segmentation to remedy the segmentation difficulties due to the presence of large vessels.

The advantages of the current 3-D wavelet-transform-learning-based NCO segmentation over the non-wavelet-transform-based NCO segmentation can be seen in Fig. 5.8. As shown in Fig. 5.8.c and e, the NCO segmentation without applying the wavelet transform presents some segmentation errors. This is mainly due to the layer segmentation errors (Fig. 5.6.a) which causes the "non-optimal" OCT projection image creation (Fig. 5.6.b). With the wavelet-transform-learning-based edge cost function, a better layer segmentation (Fig. 5.6.d) and hence a better OCT projection image is obtained (Fig. 5.6.e). As can be seen in Fig. 5.8.d and f, thus the NCO segmentation is greatly improved.

Table 5.1 provides the quantitative results of the 3-D and 2-D mean border positioning differences and mean border positioning differences in z-direction between the wavelet-transform-learning-based NCO segmentation and the 3-D manual delineation. Overall, the automated segmentation performs well when compared to the

manual delineation.

Fig. 5.9 and Fig. 5.10 show the comparison of the 3-D NCO segmentation and the manual delineation for the 9 test scans of the first type and 8 test scans of the second type respectively. The green strips are the projected segmented NCO location and the orange circles indicated by the red arrows are the manually delineated NCO points. As can be seen, the visual comparison demonstrates a great agreement between the wavelet-transform-learning-based NCO segmentation and the manual delineation.

In the previous study in human SD-OCT scans, due to the limitation of the availability of the manual delineation from 3-D SD-OCT volumes, we evaluated the robustness of our algorithm based on the inter-visit repeatability which presented a good correlation ($r = 0.95$) in terms of the NCO area. In this subsequent study, we are capable to compare our improved 3-D NCO segmentation with the 3-D NCO manual delineation directly performed on the SD-OCT volumes of non-human primate eyes. As can be seen, both the quantitative and visual comparison demonstrate a good agreement between them.

Note that as mentioned in Chapter 3, the graph search approach for finding the optimal solution of single surface was initially reported by Wu and Chen [10]. Li *et al.* [11] extended it for finding the optimal solution of multiple surfaces in a low-polynomial time using edge information, and Garvin *et al.* [12] extended it to use additional regional information. This work extends an ability to design the scale-learning-based cost function for use in the graph-theoretic approach.

Thus the major contributions of our current study can be concluded as: 1) This study further enhances the retinal layer and NCO segmentation using the learned

wavelet transform by specifically minimizing the distance between the segmented layers and manual tracings at the RPE/BM complex. 2) This study further extends the 3-D graph-based multiple layer segmentation with the use of scale-learning-based edge cost function. 3) This study further verifies our ability to automatically detect the 3-D NCO in SD-OCT volumes with the further enhancement and application of our automated NCO segmentation algorithm on non-human primate SD-OCT volumes. 4) The good agreement of our automated NCO segmentation with the manual delineation directly from 3-D SD-OCT scans shows the robustness of our algorithm. 5) This study further implies that the NCO is a single constant anatomic structure and is detectable in SD-OCT volumes, which, to a certain extent, verifies our hypothesis in our previous study that due to the stability of the NCO structure during the glaucoma progression, it may enable more reproducible and objective glaucomatous parameters than that which is currently possible from manual planimetry alone.

The developed algorithm in general performs well, however, some limitations exist. 1) For computational efficiency, when performed the layer segmentation, the original SD-OCT volumes are downsampled by two in x- and/or y-direction depending on the image type. Ideally, the layer segmentation performs on the full resolution SD-OCT volumes would be desirable. Although the "perfect" layer segmentation is not a necessary requirement for this work as the layer segmentation only serves the creation of the OCT projection images, a better layer segmentation will result in a better OCT projection image and hence a better NCO segmentation. 2) The vessel segmentation utilizes the training set from the previous NCO segmentation based on the Cirrus SO-OCT scans (Cirrus ^{TM} HD-OCT) from human subjects. Ideally, a training based

on the current data of non-human primate subjects would be expected having better performance.

In conclusion, we present an automated 3-D wavelet-transform-learning-based NCO segmentation approach with the application in volumetric SD-OCT scans of non-human primate eyes Compared to the 3-D manual delineation directly performed on the SD-OCT volumes, the automated approach demonstrates a good performance both quantitatively and visually. Because of the constant landmark nature of the NCO structure and the objective nature of the automated algorithm, along with our previous study, we expect that 2-D and/or 3-D glaucomatous parameters in volumetric SD-OCT would be more reproducible than those derived from the manual planimetry on fundus photographs or even on the time-domain OCT. Additional work will be necessary to further test our core hypothesis and explore novel, objective, reproducible NCO-based parameters that correlate well with disease stage and progression.

CHAPTER 6
SINGLE MODAL RETINAL VESSEL SEGMENTATION IN SD-OCT VOLUMES

6.1 Chapter abstract

We present a method for automatically segmenting the blood vessels in spectral-domain optical coherence tomography (SD-OCT) volumes, with a particular focus on the suppression of the false positives near the neural canal opening (NCO) boundary. The algorithm first pre-segments the NCO using a graph-theoretic approach in SD-OCT volumes. The pre-identified NCO positional information is incorporated to the pixel classification process of the blood vessels. More specifically, oriented Gabor wavelets rotated around the center of the NCO are applied to extract features in 2-D vessel-aimed OCT projection images. Corresponding oriented NCO-based templates are utilized to help suppress the false positive tendency near the NCO boundary. The vessels are classified using a k-nearest neighbor (k-NN) classifier on the 2-D vessel-aimed OCT projection images. Based on the 2-D vessel profiles, 3-D vessel segmentation is performed by a triangular-mesh-based graph search approach in SD-OCT volumes. The segmentation method is trained on 5 and tested on 10 randomly chosen independent optic nerve head (ONH) centered SD-OCT volumes from 15 subjects with glaucoma. Using receiver operating characteristic (ROC) curve analysis, for the 2-D vessel segmentation, we demonstrate an improvement over the closest previous work with an area under the curve (AUC) of 0.81 (0.72 for a previously reported approach) for the region around the NCO and 0.84 for the region outside the NCO (0.81 for a previously reported approach).

6.2 Introduction

As mentioned in the previous chapters, the large retinal vessels crossing over with the NCO in the ONH center of SD-OCT volumes cause the NCO segmentation difficulty in some scans. Segmenting vessels in SD-OCT volumes could aid a better NCO segmentation. In addition, the identification of vessels could lead to a more objective diagnosis of diseases, could be used for OCT-to-OCT and OCT-to-fundus registration, and could help remove the influence of vessels (when desirable).

However, typical vessel segmentation approaches, such as the one by Niemeijer *et al.* [50], mainly segmented the vessels in the region outside the NCO and the vessels inside the NCO were excluded from the analysis due to the similar high contrast projective appearance of the NCO contour to the vessels, causing false positives as presented in Fig. 3.1.c of Chapter 3.

Thus in this specific work, we present a 2-D pixel classification algorithm to segment the retinal vessels in the ONH-centered SD-OCT volumes, with a special focus on better identifying the retinal vessels near the NCO by incorporating the pre-identified NCO positional information to the vessel classification process [52]. Based on the segmented 2-D vessel profiles, the 3-D vessels in the SD-OCT volumes are obtained by a triangular-mesh-based graph search approach.

6.3 Methods

Overall, we approach the 2-D automatic segmentation of the blood vessels using a pixel classification algorithm (Section 6.3.2.2) by incorporating pre-segmented NCO location (Section 6.3.1) information into the classification process to suppress the false

positives near the NCO. We then utilize these 2-D vessel profiles to segment the 3-D vessels in the SD-OCT volumes [65] (Section 6.3.2.3). Fig. 6.1 is the flowchart of the major steps of our OCT vessel segmentation approach.

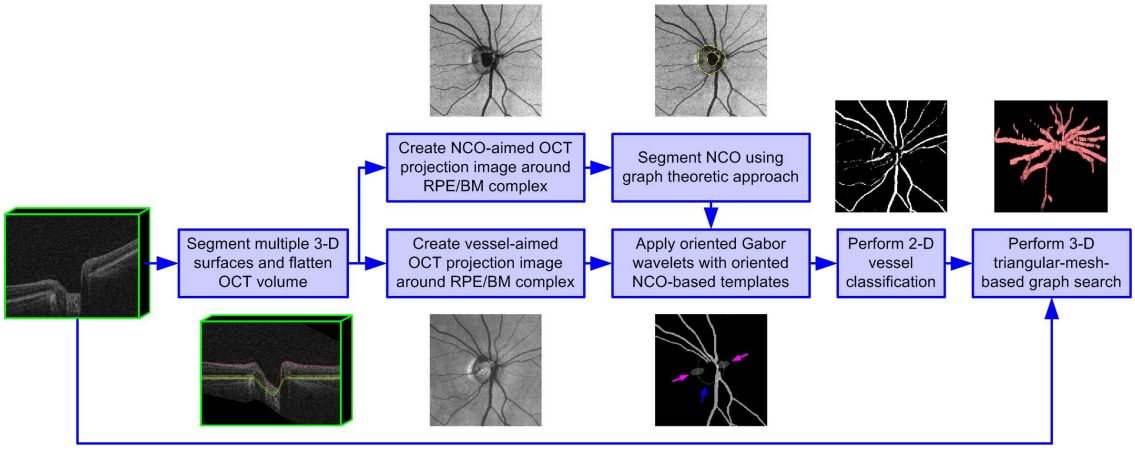

Figure 6.1: Flowchart of major steps of our OCT vessel segmentation approach.

6.3.1 Neural canal opening pre-segmentation

In order to incorporate the NCO information into the 2-D vessel classification process, the NCO is pre-segmented using the approach as described in Chapter 4 [35,36]. In this work, the NCO is the boundary of interest. However, the optic cup is also detected. Simultaneously segmenting two boundaries can take advantage of the interaction constraints between them to help better segment the NCO. Having the NCO segmentation enables the projected position of this 3-D structure to be utilized in the computation of features for the classification. Fig. 6.2 is an example illustration of NCO pre-segmentation.

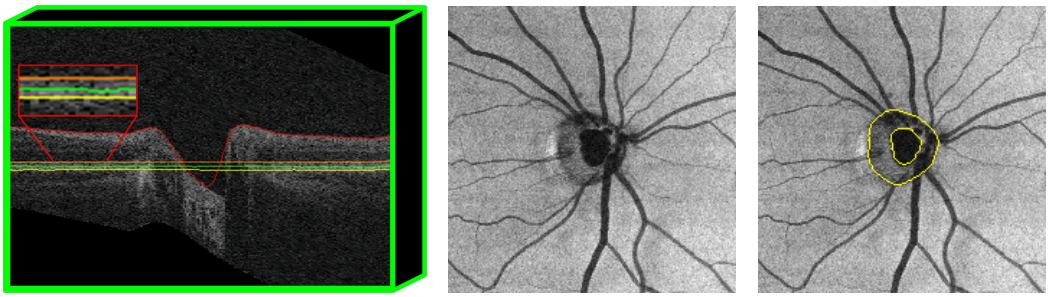

(a) (b) (c)

Figure 6.2: Illustration of the NCO segmentation. (a) 3-D four surface segmentation with the interpolation of the radial average positions outside the estimated NCO to inside the NCO for surface 2 (orange), 3 (green), and 4 (yellow). (b) NCO-aimed projection image from the layer between the interpolated surface 2 and 4. (c) Segmented NCO and cup overlapping with the projection image.

6.3.2 Retinal vessel segmentation

For the 2-D vessel segmentation, oriented Gabor wavelets around the center of the NCO are utilized to extract features in a 2-D vessel-aimed OCT projection image. The corresponding oriented NCO-based templates are utilized along with the Gabor wavelets to suppress the false positive tendency near the NCO boundary. A supervised pixel classification algorithm is applied to automatically segment the blood vessels in the vessel-aimed OCT projection image. Based on the 2-D vessel location information, the 3-D vessels are detected by applying a triangular-mesh-based graph search to the isotropic SD-OCT volume [65]. These steps are described in more detail below.

6.3.2.1 Vessel-aimed OCT projection image creation

The main difficulty of vessel segmentation within SD-OCT volumes is the weak visibility of the vessel pattern. In Niemeijer's previous approach [50], they proposed to use a 2-D projection of the vessel pattern from the 3-D volume to segment ves-

sels. They compared two different projection images: the "naive" projection image computed by averaging the whole OCT volume which decreased the contrast between the vessels and background and the "smart" projection image computed by averaging the layer between surface 2 and 4 which provided a good contrast. However, the "smart" projection image also had some disadvantages. For example, near and inside the NCO, the layer between surface 2 and 4 would frequently become very thin (and be subject to layer segmentation errors) and thus the projection image would not necessarily demonstrate an optimal contrast between vessels and background in this region.

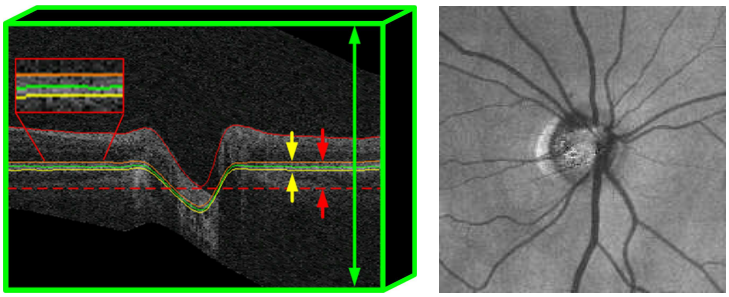

(a) (b)

Figure 6.3: Illustration of the vessel-aimed OCT projection image creation. (a) The bounding surfaces used for the creation of three potential projection images: "naive" (bounding surfaces of whole volume as indicated with green arrows), "smart" (orange surface 2 and yellow surface 4 as indicated by yellow arrows), and vessel-aimed OCT projection image (orange surface 2 and dashed red surface where possible as indicated with red arrows; same as "smart" where the red dashed surface is above the interpolated surface 4). (b) Vessel-aimed OCT projection image as used in this work.

In this work, we create a new type of projection image by averaging the layer between surface 2 and an under planar surface defined by the deepest position of

the top surface. In columns for which the deepest position is above the interpolated surface 4, the projection image is created as that used for the "smart" projection image . The created new projection image is referred to as the "vessel-aimed" OCT projection image. Compared with the "naive" and "smart" projection images [50], the vessel-aimed OCT projection image relies less on the surface segmentation and can take advantage of the vessel information inside the NCO. An illustration of the bounding surfaces for the three different projection images and a resulted vessel-aimed OCT projection image is provided in Fig. 6.3.

6.3.2.2 2-D vessel segmentation

In the vessel-aimed OCT projection image, the blood vessels generally radially distribute around the NCO center. Gabor wavelets demonstrate some desirable characteristics: spatial frequency, spatial locality, and orientation selectivity. The nature of the Gabor wavelets makes them well suitable for the feature generation of the blood vessel detection. Recall that a Gabor wavelet $\psi_{\mu,\nu}(z)$ [39] can be defined as:

$$\psi_{\mu,\nu}(z) = \frac{||k_{\mu,\nu}||^2}{\sigma^2} e^{-\frac{||k_{\mu,\nu}||^2||z||^2}{2\sigma^2}} \left[e^{ik_{\mu,\nu}z} - e^{-\frac{\sigma^2}{2}} \right], \tag{6.1}$$

where $z = (x, y)$, $||\cdot||$ is the norm operator, μ and ν define the orientation and spatial frequency scale of the Gabor kernel, and σ is related to the standard derivation of the Gaussian window in the kernel and determines the ratio of the Gaussian window width to the wavelength. The wave vector $k_{\mu,\nu}$ is defined as

$$k_{\mu,\nu} = k_\nu e^{i\phi_\mu}, \tag{6.2}$$

where $k_\nu = \frac{k_{max}}{f^\nu}$ in which k_{max} is the maximum frequency and f^ν is the spatial frequency between kernels in the frequency domain. $\phi_\mu = \frac{\pi\mu}{n}$ in which n is the total number of orientations. Based on the vessel profiles, in our application, we choose $k_{max} = \frac{\pi}{2}$, $\sigma \in \{1, 2, 3\}$, f=$\sqrt{2}$, $\nu \in \{1, 2, 3\}$, n=18, and $\mu \in \{0, ..., 17\}$.

Additionally, to increase the signal and decrease the noise, three spatial frequency scale additions are applied between ν=2 and ν=3 in $\sigma \in \{1, 2, 3\}$. Together a Gabor wavelet family with 3 Gaussian scales, 3 spatial frequency scales, 3 spatial frequency scale additions, and 18 orientations is generated.

In order to suppress the false positive tendency near the NCO, the oriented templates are utilized along with the corresponding Gabor wavelets in the feature space. Specifically a pair of pre-defined templates is first created based on the previously segmented NCO location information and so-called NCO-based templates. The center of the template pair is that of the NCO and the center of each of them lies on the NCO boundary. The shapes of the templates are defined as:

$$\frac{\{x_1 - x_c - r_1\}^2}{W^2} + \frac{\{y_1 - y_c\}^2}{H^2} = 1, \tag{6.3}$$

and

$$\frac{\{x_2 - x_c + r_2\}^2}{W^2} + \frac{\{y_2 - y_c\}^2}{H^2} = 1, \tag{6.4}$$

where (x_c, y_c) is the NCO center, r_1 and r_2 are the distances of the center of each template to the center of NCO, and W and H are the maximum width and height of the templates which are defined based on prior knowledge of NCO profiles. Fig. 6.4.b

provides a schematic illustration of the Gabor wavelet responses and the NCO-based templates.

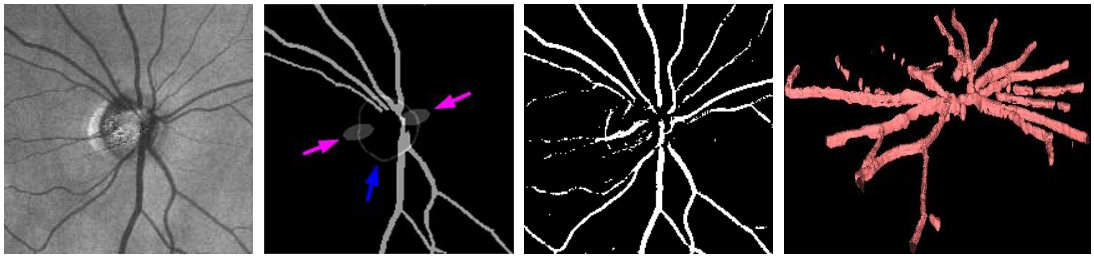

(a) (b) (c) (d)

Figure 6.4: Illustration of the OCT vessel segmentation. (a) Vessel-aimed OCT projection image. (b) A schematic illustration of the Gabor wavelet responses and the NCO-based templates oriented at 160 degrees. Blue arrow = NCO contour. Purple arrows = template pair centered on the NCO boundary. (c) 2-D vessel segmentation. (d) 3-D vessel segmentation.

The NCO-based templates rotate in the same orientations as the Gabor wavelets. Wherever they rotate, the average pixel value of the Gabor wavelet response in that orientation is assigned to those regions. The NCO-based templates could help suppress the false positive tendency from the NCO and at the same time does not affect the true positives of the blood vessels, based on the assumption that the blood vessels are not parallel with the NCO. In addition to the Gabor wavelet response, the pixel gray value from the vessel-aimed OCT projection image is also included in the feature space.

After the feature extraction, each feature is normalized to zero mean and unit variance. We then apply a supervised pixel-classification-based approach to identify

the blood vessels. More specifically, the method utilizes a one-time training phase. The training set includes 5 vessel-aimed OCT projection images. It has $200 \times 200 \times 5 = 200000$ training samples and each sample is labeled "vessel" or "non-vessel" with the help of experts as described in Section 6.4.

In the testing phase, each pixel in the test image is treated as a query sample and is classified by the trained k-NN classifier with $k = 31$. To save the running time, in this work, the searching of the nearest neighbor training samples for each query sample is implemented by searching the approximate nearest neighbor training samples with a tolerance of a small amount of error [48]. Based on the obtained k nearest neighbor training samples, each query sample (pixel) in the test image is assigned to a soft label, i.e. a posterior probability defined as $p_{vessel} = n/k$, where n is the number of the training samples labeled as "vessel" among the k nearest neighbor training samples. An example of the segmented 2-D OCT vesselness map is provided in Fig. 6.4.c.

6.3.2.3 3-D vessel segmentation

In order to perform the 3-D vessel segmentation [65], the flattened SD-OCT is first transformed to an isotropic volume. Surface 1 and 2 are also correspondingly transformed. As mentioned above, the blood vessels themselves in the SD-OCT volume of the ONH are not visible. What we measure in the 2-D vessel-aimed OCT projection image are the vessel silhouettes. The "true" vessels are located right above the vessel silhouettes [49]. We assume the vessels are approximately the three middle voxels between surface 1 and 2 in the z-axis of the SD-OCT volume. An initial binary

3-D vessel model is created by projecting the segmented 2-D vessel locations to the layer of the three middle voxels. A marching cube algorithm is applied to the initial model to construct a triangular mesh. The magnitude of the Gaussian derivative of the volumetric SD-OCT is combined with that of the vessel-aimed OCT projection image to create the cost image. The globally optimal surfaces of the 3-D vessels are achieved by solving a maximum flow problem on the constructed triangular-mesh-based graph from the combined cost image. An example of the 3-D OCT vessel segmentation result is shown in Fig. 6.4.d.

6.4 Experimental methods and results

Fifteen ONH-centered SD-OCT volumes from 15 subjects with glaucoma are acquired using a Cirrus^{TM} HD-OCT (Carl Zeiss Meditec) device. Each volume has the size of $200 \times 200 \times 1024$ voxels corresponding to $6 \times 6 \times 2$ mm^3. Of the 15 volumes, 5 of them are randomly selected as the training set and 10 of them the test set. Each pixel in the vessel-aimed OCT projection image is manually labeled as "vessel" or "non-vessel" with the help of experts. The small vessels by observation are excluded from the "vessel" category and labeled as "non-vessel".

The performance of the 2-D vessel segmentation is evaluated using ROC curves. Our present approach of the 2-D vessel segmentation is compared with Niemeijer's approach [50] in terms of AUC for the regions around the NCO ($\pm$15 pixels from the NCO boundary) and outside the NCO boundary.

Table 6.1 demonstrates the 2-D quantitative segmentation results by comparing the AUC of the region outside the NCO and the region around the NCO ($\pm$15 pixels

Table 6.1: AUC comparison of Niemeijer's previous and our present 2-D OCT vessel segmentation

AUC of the region around NCO		AUC of the region outside NCO	
Niemeijer's algor.	Our algor.	Niemeijer's algor.	Our algor.
0.72	0.81	0.81	0.84

from the NCO boundary) of the two algorithms. Our present algorithm gives a greater AUC in both regions, especially in the region around the NCO.

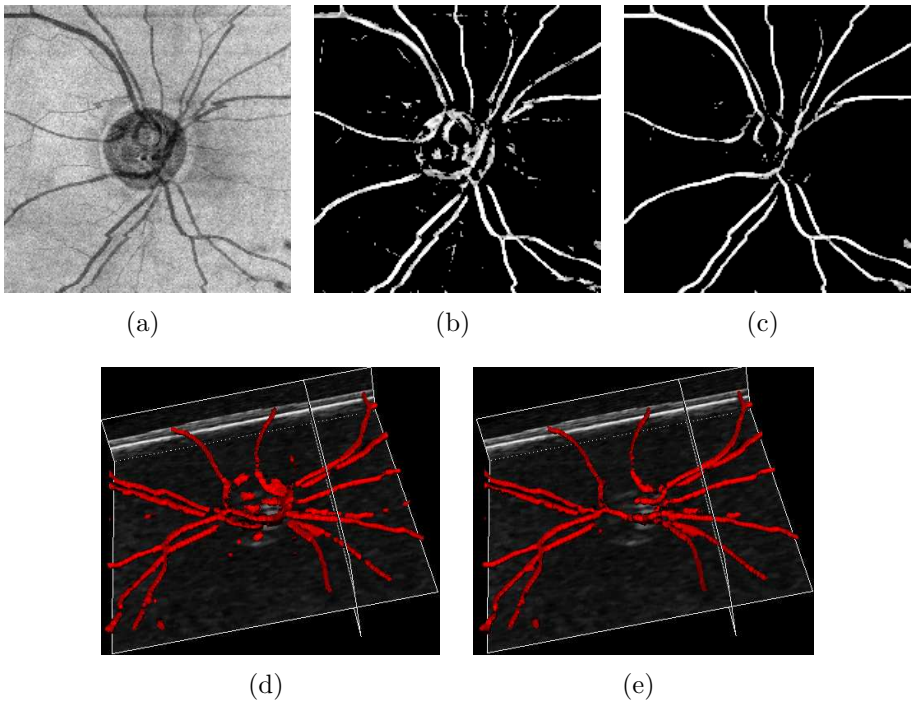

Figure 6.5: Comparison of Niemeijer's previous and our present OCT vessel segmentation. (a) Vessel-aimed OCT projection image. (b and c) Niemeijer's previous and our present 2-D OCT vessel segmentation. (d and e) Niemeijer's previous and our present 3-D OCT vessel segmentation. Especially note the improvement from our present approach around the NCO.

An example visual comparison of the 2-D and 3-D vessel segmentation between Niemeijer's previous and our present approach is illustrated in Fig. 6.5. Fig. 6.5.b and d show the results of the 2-D and 3-D segmentation from Niemeijer's previous approach and Fig. 6.5.c and e show that from our present approach, respectively. As can be seen, the clear false positives near the NCO exist in the previous approach. However, in the present approach, it is greatly suppressed and the vessels around the NCO are detected.

6.5 Discussion and conclusions

We developed an approach for automatically segmenting the retinal blood vessels by focusing on the region around the NCO in ONH-centered SD-OCT volumes. To our knowledge, this is the first such algorithm to segment the blood vessels by utilizing *a-priori* NCO segmentation information, along with rotated Gabor wavelets and corresponding rotated NCO-based templates to suppress the false positive tendency near the NCO. The result is promising considering the difficulty of the vessel segmentation in ONH-centered SD-OCT volumes. Compared with the closest previous work [50], the 2-D vessel segmentation results are greatly improved both visually and quantitatively, especially for the region around the NCO.

However, the accuracy of the 2-D vessel segmentation is still not perfect. Some of the potential error sources include the following. 1) As described above, when the large variations in the surfaces are present, intraretinal layer segmentation errors can occur. As the NCO-aimed OCT projection image are dependent on the layer segmentation, the errors can cause the "non-optimal" OCT projection image problem,

which can cause the NCO segmentation errors. 2) The NCO is simultaneously segmented with the optic cup on the NCO-aimed OCT projection image. Currently the unwrapped center from Cartesian coordinates to polar coordinates is simply taken as the center of the NCO-aimed OCT projection image. The center point must be within the optic cup for the transformation to be valid. However, in some images, that could be not true and thus there exists a "non-optimal" unwrapped center problem. Hence the NCO pre-segmentation errors can occur, which could cause the incorrect positions of the NCO templates and thus may not be able to efficiently suppress the false positives near the NCO. 3) The expert may not have always traced very small vessels they deemed "incomplete", whereas the algorithm would have found portions of these vessels, thus (incorrectly) causing the identification of these regions as false positives. 4) The relatively low visibility in the ONH center of SD-OCT volumes causes the difficulty of the vessel identification.

In summary, in this work, we develop a 2-D pixel-classification-based method for segmenting the vessels in SD-OCT volumes with a focus on the ability to better indicate the vessels in the region near the neural canal opening by incorporating the pre-identified NCO positional information to the vessel classification. Based on the 2-D vessel profiles, 3-D vessel segmentation is performed by a triangular-mesh-based graph search approach in SD-OCT volumes. Using ROC analysis, the 2-D vessel segmentation demonstrates an obvious improvement over the closest previous work [50].

However, as mentioned above, our OCT vessel segmentation is not perfect. To further enhance the performance, we develop a registered-fundus and a multimodal

vessel segmentation approach using additional information from fundus photographs to obtain better vessel profiles in SD-OCT volumes as presented in the next chapter (Chapter 7).

CHAPTER 7
MULTIMODAL AND REGISTERED-FUNDUS VESSEL SEGMENTATION IN SD-OCT VOLUMES AND COLOR FUNDUS IMAGES

7.1 Chapter abstract

Segmenting retinal vessels in optic nerve head (ONH) centered spectral-domain optical coherence tomography (SD-OCT) volumes is particularly challenging due to the projected neural canal opening (NCO) and relatively low visibility in the ONH center. Fundus photographs provide a relatively high vessel contrast in the region inside the NCO. We thus first develop an approach to obtain better vessel profiles from fundus images for the use in SD-OCT volumes by segmenting retinal vessels on original fundus images and registering the segmented vessel images to SD-OCT images (referred to as registered-fundus vessel segmentation approach). However, such approach has its limitations such as the segmentation difficulty from the projected NCO contour. We thus further develop a multimodal vessel segmentation approach utilizing the complementary information from both modalities, such as the 3-D retinal layer information, better NCO contrast from the 3-D SD-OCT modality, and better vessel contrast inside the NCO from fundus photographs, to help better segment vessels in SD-OCT images. In particular, in each SD-OCT volume, the algorithm pre-segments the NCO using a graph-theoretic approach. Oriented Gabor wavelets with oriented NCO-based templates are applied to generate OCT image features. After fundus-to-OCT registration, the fundus image features are computed using oriented Gabor wavelets with oriented NCO-based templates and additional Gaussian filter banks. The two feature spaces are then combined. A k-Nearest Neighbor (k-NN)

classifier is trained on 15 and tested on 19 randomly chosen independent image pairs of SD-OCT volumes and fundus images from 34 subjects with glaucoma. Based on the receiver operating characteristic (ROC) curve analysis, for all the 19 test images, the area under the curve (AUC) of two previous closest OCT-based vessel segmentation approaches (Niemeijer's and our OCT single modal approach), our present registered-fundus and multimodal approaches in the region inside the NCO are 0.64, 0.67, 0.85, and 0.86 respectively; in the region outside the NCO, are 0.84, 0.87, 0.90, and 0.92 respectively. The present registered-fundus and multimodal vessel segmentation approaches both perform significantly better than the two previous OCT-based approaches. The multimodal approach overall performs better than the other three single modal approaches.

7.2 Introduction

In Chapter 6, we presented a single modal approach for segmenting retinal vessels in ONH-centered SD-OCT volumes by incorporating the pre-segmented NCO positional information in the vessel classification process to help suppress the false positive tendency near the NCO boundary [52]. The performance of the algorithm demonstrated an obvious improvement over Niemeijer's previous OCT vessel segmentation approach [50]. However, the relatively low visibility in the ONH center remains a problem for vessel identification in some scans.

While only a few approaches have been reported for the segmentation of vessels in SD-OCT volumes [50,51], many vessel segmentation approaches performed on fundus photographs have been reported [43–45]. The blood vessels on fundus photographs

present a relatively high contrast in the region near and inside the NCO over SD-OCT images (Fig. 7.1). We thus first develop an approach to obtain vessel profiles from fundus images for the use in SD-OCT volumes by segmenting retinal vessels on original fundus images [45], registering the segmented fundus images to SD-OCT images [53], and using the transformed fundus vessels as OCT vessels. This approach is referred to as registered-fundus vessel segmentation approach. However, such approach presents some problems in some cases, for instance, the false positives or breaks near the region of the optic disc margin (partially corresponding to the NCO in SD-OCT scans).

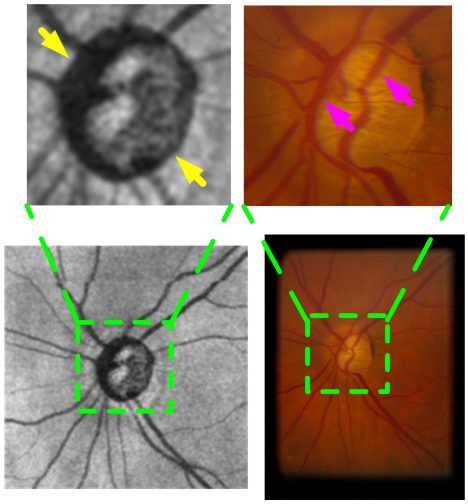

Figure 7.1: Illustration of the high visibility of the NCO in SD-OCT image and that of vessels on fundus image. Left column: vessel-oriented OCT projection image (bottom) (Section 7.3.2.1) with the zoomed ONH center (upper). Note that the high NCO contrast as indicated by the yellow arrows. Right column: fundus photograph (bottom) with the zoomed ONH center (upper). Note that the high vessel contrast as indicated by the purple arrows.

Note that the two modality images of SD-OCT volumes and color fundus pho-

tographs provide some complementary features, such as the 3-D retinal layer information and relatively high contrast of the NCO boundary in SD-OCT images and that of the blood vessels in the region near and inside the NCO on fundus photographs. Simultaneously segmenting the blood vessels in both modalities could take advantage of their complementary information. Thus, we further develop a multimodal pixel classification approach [58] simultaneously using the information from SD-OCT volumes and color fundus photographs to aid a better vessel segmentation for use in SD-OCT images.

7.3 Methods

An overview of our registered-fundus and multimodal vessel segmentation approaches is presented in Fig. 7.2.

In both approaches, we first segment the retinal vessels on original fundus photographs using a pixel-classification-based approach (Section 7.3.1). Once we have the vessel profiles on the original fundus photographs, we register the images in fundus modality to the OCT modality using a feature-point-based registration approach [53]. More specifically, in our first approach, we register the segmented fundus vessel image to the OCT modality and use the registered fundus vessels as the OCT vessels (Section 7.3.2.2). In our second approach, we register the original fundus images to the OCT modality using the same transformation and apply a multimodal vessel segmentation (Section 7.3.3) by incorporating the complementary information from SD-OCT volumes (e.g. the NCO positional information) and fundus photographs (e.g. better vessel contrast in the region inside the NCO). Fig. 7.3 provides a more

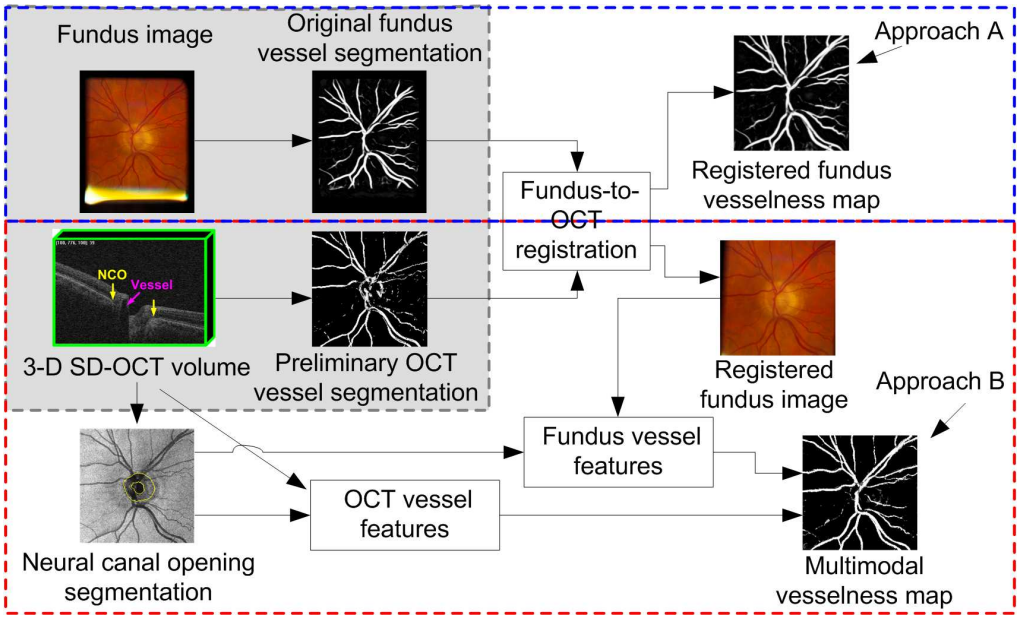

Figure 7.2: Overview of registered-fundus and multimodal vessel segmentation, where the dashed-blue-line and light-gray-background blocks indicate the registered-fundus vessel segmentation and the dashed-red-line and light-gray-background blocks indicate the multimodal vessel segmentation.

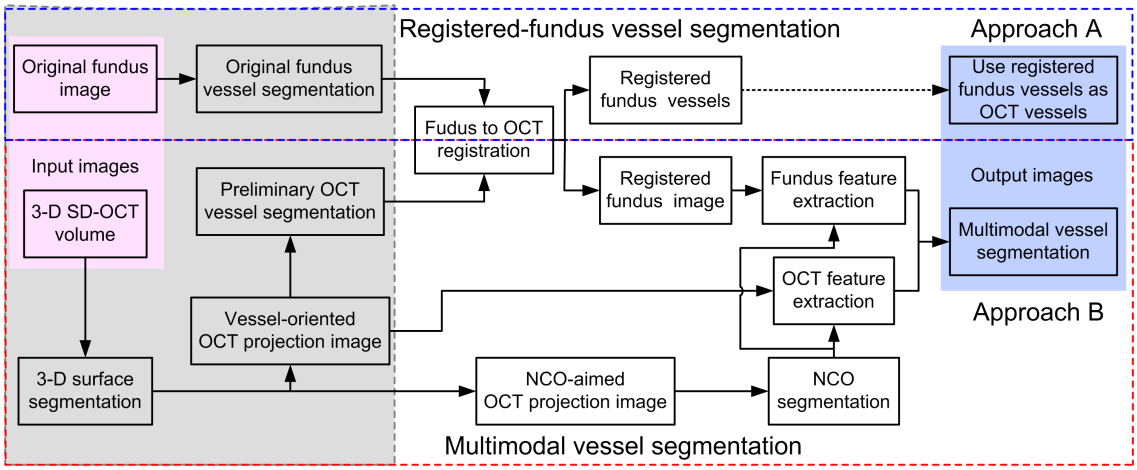

Figure 7.3: Flowchart of major steps of registered-fundus and multimodal vessel segmentation, where the dashed-blue-line and light-gray-background blocks indicate the registered-fundus vessel segmentation and the dashed-red-line and light-gray-background blocks indicate the multimodal vessel segmentation.

detailed overview of the major steps of both approaches.

7.3.1 Vessel segmentation in original fundus photographs

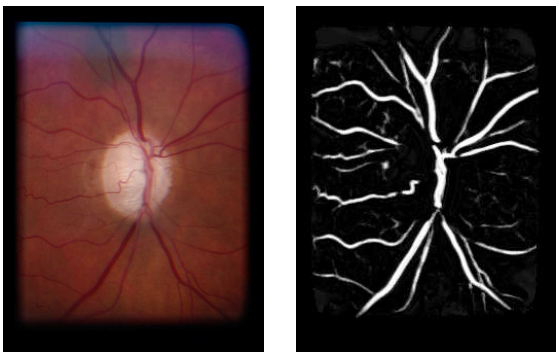

(a) (b)

Figure 7.4: Illustration of original fundus vessel segmentation. (a) Original color fundus image. (b) Segmented vesselness map of the original fundus image.

A supervised pixel-classification-based segmentation method is used to segment the blood vessels in the original fundus photographs [45]. The pixel features are extracted using Gaussian derivative filters. Each image L consists of Gaussian filter derivatives up to and including order 2 (i.e. L, L_x, L_y, L_{xx}, L_{xy}, L_{yy}) at scales σ equal to 1, 2, 4, 8, and 16 pixels. A k-NN classifier (k=31) is applied and each pixel in the projection image is assigned a soft label. Together they form a vesselness image. An example illustration of the original fundus photograph segmentation is shown in Fig. 7.4.

7.3.2 Registered-fundus vessel segmentation

7.3.2.1 Vessel-oriented OCT projection image creation

The fundus-to-OCT registration needs a reference image in the SD-OCT modality. Thus we create an OCT projection image at the NCO plane in the SD-OCT volume. More specifically, four intraretinal 3-D surfaces are simultaneously identified in the 3-D raw SD-OCT volumes using an optimal graph-theoretic multilayer segmentation algorithm. Based on a segmented surface, we then flatten the raw SD-OCT volumes (Fig. 7.5.b) [12, 28]. The four segmented surfaces are also flattened by applying the same transformation.

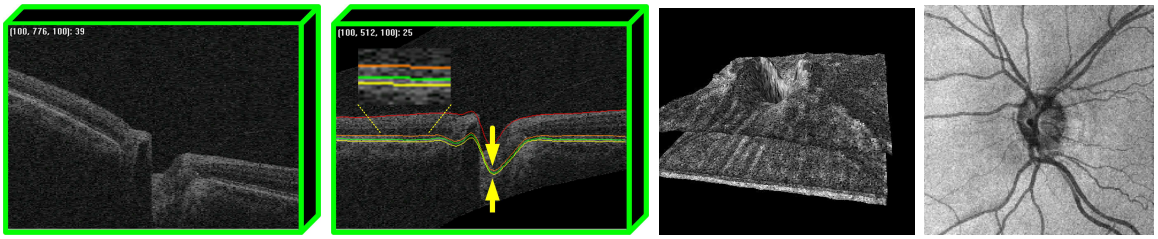

(a) (b) (c) (d)

Figure 7.5: Illustration of vessel-oriented OCT projection image creation. (a) Central slice of the raw SD-OCT volume. (b) Central slice of the flattened SD-OCT volume with four segmented retinal surfaces indicated. (c) 3-D visualization of segmented surfaces. (d) Vessel-oriented OCT projection image obtained from the layer indicated by the yellow arrows in (b).

After the flattening of the original 3-D SD-OCT volume, the projection image is obtained by computing the mean intensity values from a small number of slices surrounding the NCO plane, i.e., the thin layer between the segmented surface 2

(orange) and 4 (yellow) in the flattened OCT image, as indicated by the yellow arrows in Fig. 7.5.b and is referred to as the "vessel-oriented" OCT projection image as it is also used for the OCT vessel feature extraction. Fig. 7.5.d is an example of the resulted vessel-oriented OCT projection image.

7.3.2.2 Registered-fundus vessel segmentation

To register the segmented original fundus vessels to the vessel-oriented OCT projection image, we also segment the vessels on the vessel-oriented OCT projection image using Niemeijer's previous OCT vessel segmentation approach [50]. Note that although this preliminary approach presents some false positives around the NCO boundary in some images as described previously, it is good enough to provide feature points such as the vessel bifurcations in the region outside NCO for the registration.

The Random Sample Consensus (RANSAC) algorithm [66] is then applied to remove the outliers of the initial matching points finding by the Scale Invariant Feature Transformation (SIFT) detector [67]. An exhaustive search is utilized to find the best set of matching points. The original fundus vesselness map is registered to the vessel-oriented OCT projection image using an affine transformation and cropped to the same size as the vessel-oriented OCT projection image. Fig. 7.6 is an illustration of the registered-fundus vessel segmentation.

7.3.3 Multimodal retinal vessel segmentation

7.3.3.1 Overview

The multimodal approach utilizes features from both modalities of SD-OCT volumes and color fundus photographs for pixel classification to segment the vessels. In

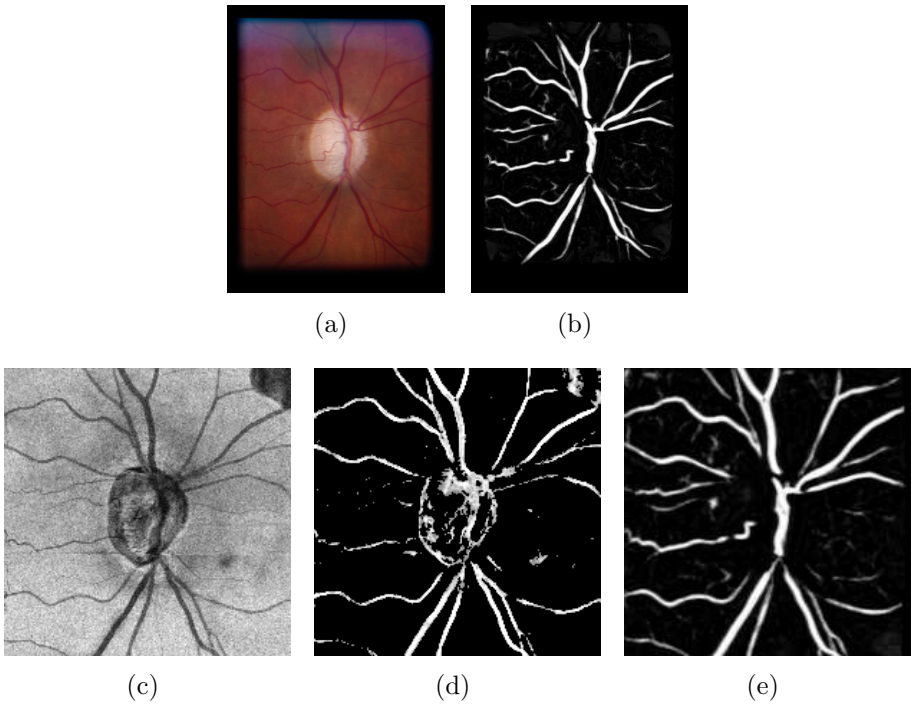

Figure 7.6: Illustration of registered-fundus vessel segmentation. (a) Original color fundus image. (b) Segmented vesselness map of the original fundus image. (c) Vessel-oriented OCT projection image. (d) Preliminary OCT vessel segmentation [50]. (e) Cropped fundus-to-OCT registered vessel image.

SD-OCT modality, to suppress the false positives near the NCO boundary, the algorithm first pre-segments the NCO using the approach presented in Chapter 4 [35,36]. Oriented Gabor wavelets rotated around the center of the NCO along with the corresponding oriented NCO-based templates are applied to extract OCT features (Section 7.3.3.3) [52] . To extract the fundus features, the fundus images are first registered to the vessel-oriented OCT projection images (using vessel information) in the same manner as registering the segmented fundus vessel images to the OCT modality (Section 7.3.2.2) and cropped to the same size as the vessel-oriented OCT projection images. Gabor wavelets with oriented NCO-based templates and an additional Gaus-

sian filter family with different Gaussian derivatives and scales are applied on the registered fundus images to extract the fundus features. A k-NN classifier is utilized to detect the retinal vessels by combining the complementary feature spaces of the two modalities as described in Section 7.3.3.5 [58]. The major steps of the multimodal vessel segmentation can be found in Fig. 7.3 and the further details are provided in the paragraphs below.

7.3.3.2 NCO pre-segmentation in SD-OCT volumes

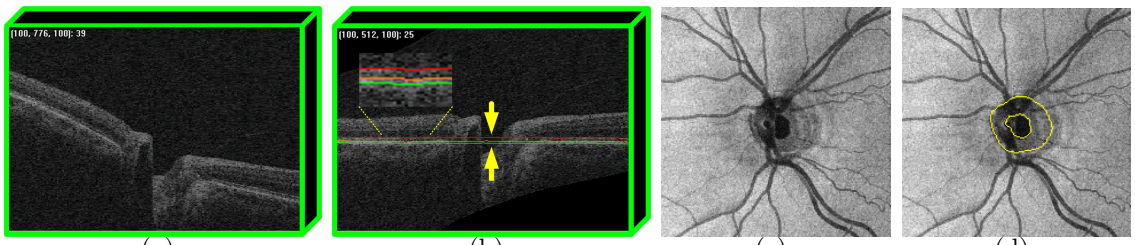

Figure 7.7: Illustration of NCO segmentation. (a) Central slice of the raw SD-OCT volume. (b) Central slice of the flattened SD-OCT volume with three radially interpolated surfaces. (c) NCO-aimed OCT projection image obtained from the layer indicated by the yellow arrows in b. (d) NCO (outer boundary) and optic cup (inner boundary) segmentation overlapping with the NCO-aimed projection image.

To incorporate the NCO information into the vessel classification process, the NCO is pre-segmented from a NCO-aimed OCT projection image using the approach as described in (Chapter 4) [35, 36]. Fig. 7.7 is an example illustration of the NCO segmentation. Having the NCO segmentation enables the projected position of this 3-D structure to be utilized in the computation of features for the classification.

7.3.3.3 Feature extraction in SD-OCT volumes

The pixel features in the SD-OCT image modality are generated from the vessel-oriented OCT projection images (Fig. 7.8.b) using a similar Gabor wavelet filter family as used in our single modal OCT vessel segmentation approach [52] (Chapter 6).

The Gabor wavelet parameters are chosen as follows: the Gaussian scale $\sigma \in \{1, 2\}$, spatial frequency scale $\nu \in \{1, ..., 6\}$, and orientation $\mu \in \{0, ..., 8\}$. Together, a Gabor wavelet family with 2 Gaussian scales, 6 spatial frequency scales, and 9 orientations is generated. To suppress the NCO false positive tendency, the NCO-based templates as described in Section 6.3.2.2 of Chapter 6 are also applied. The intensity value from the vessel-oriented OCT projection image is also included in the SD-OCT modality feature space.

7.3.3.4 Feature extraction on fundus photographs

The pixel features in the color fundus image modality are generated from the green channel of the registered fundus image as shown in Fig. 7.8.a because the green channel provides a relatively high vessel contrast. Oriented Gabor wavelets with NCO-based templates and additional Gaussian filter banks in x- and y-direction are applied for the feature extraction.

More specifically, oriented Gabor wavelets with NCO-templates at Gaussian scale of $\sigma = 2$, spatial frequency scales $\nu \in \{1, ..., 5\}$, and orientation $\mu \in \{0, ..., 8\}$ are created. Together, they come to a Gabor wavelet family with 1 Gaussian scale, 5 spatial frequency scales, and 9 orientations [52]. In addition, a Gaussian filter family

with the Gaussian derivatives with the orders of $N \in \{1, 2\}$ and 5 Gaussian scales at $\sigma \in \{1, 2, 4, 8, 16\}$ is also generated. The Gaussian derivatives are applied only in the x- and y-direction. The intensity value from the green channel of the transformed color fundus photograph is also included in the fundus modality feature space.

Table 7.1 is a summary of the pixel features from the SD-OCT and fundus images.

Table 7.1: Pixel features from the SD-OCT and fundus images

		OCT features	**Fundus features**
Oriented Gabor wavelets with NCO-templates	Frequency	$\nu \in \{1, ..., 6\}$	$\nu \in \{1, ..., 5\}$
	Gaussian scale	$\sigma \in \{1, 2\}$	$\sigma = 2$
	Orientation	$\mu \in \{0, ..., 8\}$	$\mu \in \{0, ..., 8\}$
Gaussian derivative filters	Gaussian scale	None	$\sigma \in \{1, 2, 4, 8, 16\}$
	Order	None	$N \in \{1, 2\}$
Original intensity		Included	Included

7.3.3.5 k-NN classification

After separately extracting the pixel features from the vessel-oriented OCT projection and registered fundus images, the feature spaces of the two modalities are combined. In other words, for each sample in the multimodal image space, the multimodal feature vectors include the features from both modalities and each feature vector is normalized to zero mean and unit variance.

We then apply a supervised pixel-classification-based approach to identify the blood vessels. More specifically, the method utilizes a one-time training phase. The training set includes 15 image pairs of vessel-oriented OCT projection images and corresponding registered fundus images. Totally $200 \times 200 \times 15 = 600000$ training

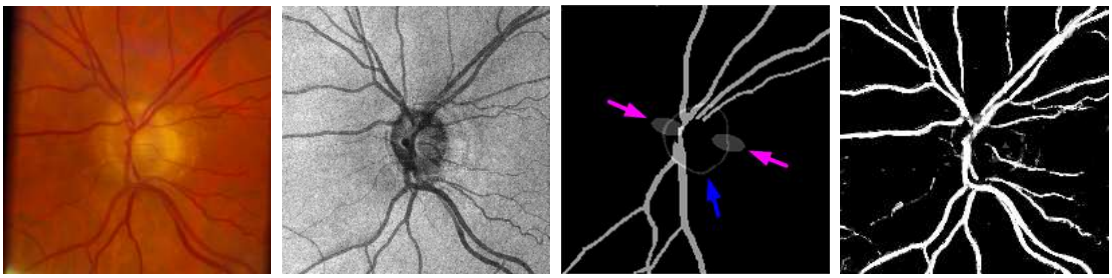

(a) (b) (c) (d)

Figure 7.8: Illustration of multimodal retinal vessel segmentation. (a) Registered fundus to OCT image. (b) Vessel-oriented OCT projection image. (c) A schematic illustration of the Gabor wavelet responses and the NCO-based templates oriented at 20 degrees. Blue arrow = NCO contour. Purple arrows = template pair centered on the NCO boundary. (d) Vessel segmentation from the multimodal approach.

samples are obtained and each sample is labeled "vessel" or "non-vessel" with the help of experts as described in Section 7.4. The random sampling is utilized to decrease the training samples and thus enhance the training speed.

In the testing phase, each pixel pair in the test image pair of the vessel-oriented OCT projection images and corresponding cropped fundus registered images is treated as a query sample and is classified by the trained k-NN classifier with $k = 31$. Each query sample (pixel pair) in the test image pair is assigned to a soft label, i.e. a posterior probability as described in Chapter 6. Fig. 7.8 is an example illustration of the multimodal blood vessel segmentation.

7.4 Data and experimental methods

The data is based on the dataset for the NCO segmentation used in Chapter 4 [36], which includes 34 independent deidentified ONH-centered SD-OCT scans (Cirrus^{TM} HD-OCT) and corresponding stereo color fundus photographs (Nidek 3Dx) image

pairs from 34 subjects with glaucoma. Fifteen image pairs are randomly chosen as the training set and the remaining nineteen pairs are used as the test set.

Each SD-OCT scan consists of 200 × 200 × 1024 voxels, corresponding to 6 × 6 × 2 mm^3. Each stereo color fundus photograph has 4096 × 4096 pixels. The NCO-aimed, vessel-oriented OCT projection images, and the cropped color fundus registered images have a size of 200 × 200 pixels. The pixel depth of the color fundus photograph is 3 × 8-bit in red, green, and blue channels.

Expert-assisted manual tracings with each pixel labeled as "vessel" or "non-vessel" are obtained based on the vessel-oriented OCT projection and cropped fundus registered images. When mis-alignments between the two images exist, the manual tracings favor the vessel information from the vessel-oriented OCT projection images in the region outside the NCO. In the region inside the NCO, the vessel tracings are the union of the vessel information from both images. The manual tracings are used as the reference standard for the validation of the vessel segmentation approaches.

The performance of the vessel segmentation approaches is evaluated based on the AUC of the ROC curves. The AUC comparison is performed based on non-parametric approach proposed by DeLong *et al.* [68] using the pROC package [69] for R and *p*-values less than 0.05 are considered significant.

7.5 Results

Table 7.2 and 7.3 demonstrate the quantitative results by comparing our two current approaches, i.e. the registered-fundus and multimodal approaches, with two closest previous approaches, i.e. Niemeijer's previous OCT [50] and our previous

Table 7.2: AUC comparison among Niemeijer's previous OCT, our previous single modal OCT, registered-fundus, and multimodal algorithms for the 16 automated-registration-based test eyes

Region	Inside NCO			
Modality	Single modal			Multimodal
Algorithm	Niemeijer's OCT	Our OCT [3]	Registered-fundus	Multi-modality
AUC	0.65	0.68	0.87	0.87
(Pairwise AUC test) [1]	($p < 0.05$)	($p < 0.05$)	($p > 0.05$)	
(Pairwise AUC test) [2]	($p < 0.05$)	($p < 0.05$)		
Region	Outside NCO			
Modality	Single modal			Multimodal
Algorithm	Niemeijer's OCT	Our OCT [3]	Registered-fundus	Multi-Modality
AUC	0.85	0.87	0.92	0.94
(Pairwise AUC test) [1]	($p < 0.05$)	($p < 0.05$)	($p < 0.05$)	
(Pairwise AUC test) [2]	($p < 0.05$)	($p < 0.05$)		

[1]: pairwise AUC test [68] performed between the multimodal and the three indicated single modal vessel segmentation approaches, respectively.

[2]: pairwise AUC test [68] performed between the registered-fundus and the two indicated OCT-based vessel segmentation approaches, respectively.

[3]: our OCT refers to our single modal OCT vessel segmentation approach (Chapter 6) [52].

single modal OCT (Chapter 6) [52] approaches. Note that in Table 7.2, three of the 19 test eyes are excluded to the statistical analysis because of the relative large automated registration errors due to the low vessel visibility and/or "non-optimal" OCT projection images such as from the motion artifact. However, Table 7.3 provides the AUC analysis results for all the 19 test eyes. In the three cases that the automated registration presents relative large errors, a manual registration is applied.

From Table 7.3, for the region inside the NCO, the AUC of Niemeijer's previous OCT, our previous single modal OCT, our current registered-fundus and multimodal approaches for the 19 test eyes are 0.64, 0.67, 0.85, and 0.86 respectively; for the

Table 7.3: AUC comparison among Niemeijer's previous OCT, our previous single modal OCT, registered-fundus, and multimodal algorithms for all the 19 test eyes

Region	Inside NCO			
Modality	Single modal			Multimodal
Algorithm	Niemeijer's OCT	Our OCT [3]	Registered-fundus	Multi-modality
AUC	0.64	0.67	0.85	0.86
(Pairwise AUC test) [1]	($p < 0.05$)	($p < 0.05$)	($p > 0.05$)	
(Pairwise AUC test) [2]	($p < 0.05$)	($p < 0.05$)		
Region	Outside NCO			
Modality	Single modal			Multimodal
Algorithm	Niemeijer's OCT	Our OCT [3]	Registered-fundus	Multi-Modality
AUC	0.84	0.87	0.90	0.92
(Pairwise AUC test) [1]	($p < 0.05$)	($p < 0.05$)	($p < 0.05$)	
(Pairwise AUC test) [2]	($p < 0.05$)	($p < 0.05$)		

[1]: pairwise AUC test [68] performed between the multimodal and the three indicated single modal vessel segmentation approaches, respectively.

[2]: pairwise AUC test [68] performed between the registered-fundus and the two indicated OCT-based vessel segmentation approaches, respectively.

[3]: our OCT refers to our single modal OCT vessel segmentation approach (Chapter 6) [52].

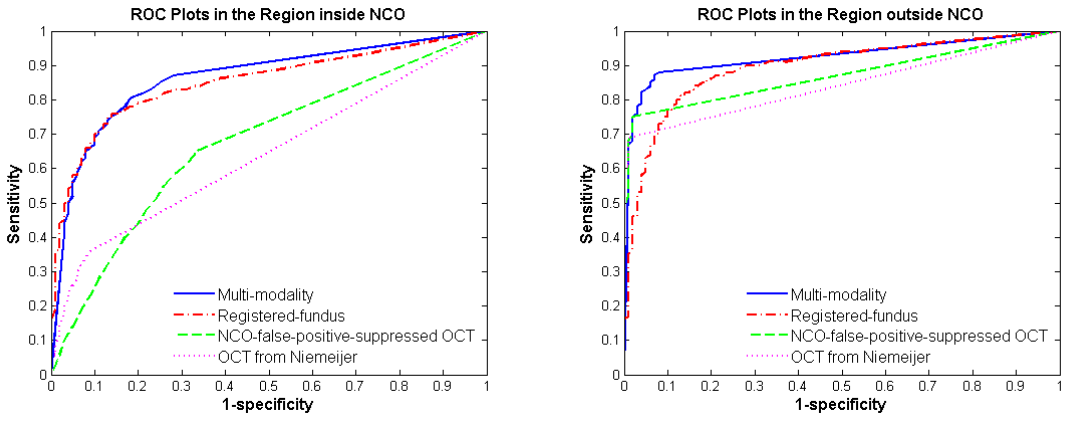

(a) (b)

Figure 7.9: ROC curves of four different vessel segmentation approaches for all the 19 test eyes. ROC curves in the region (a) inside the NCO and (b) outside the NCO.

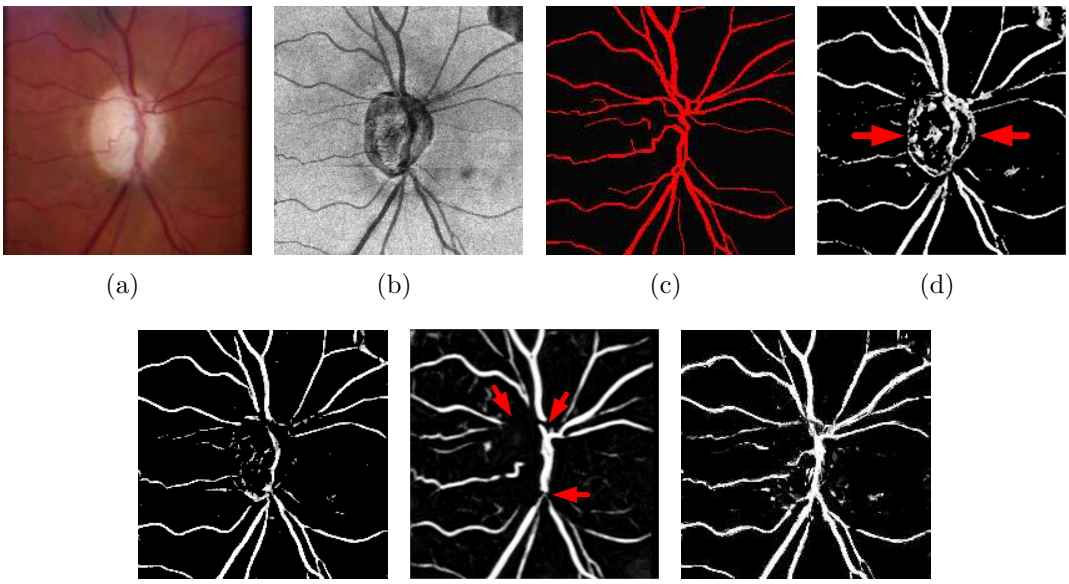

Figure 7.10: Example comparison of the four different vessel segmentation algorithms. (a) Cropped fundus registered image. (b) Vessel-oriented OCT projection image. (c) Ground truth. (d-g) Vessel segmentation from Niemeijer's previous OCT, our previous single modal OCT, registered-fundus, and multimodal approach respectively. The red arrows indicate the false positives or vessel breaks due to the presence of the optic disc/NCO boundary.

region outside the NCO, are 0.84, 0.87, 0.90, and 0.92 respectively. Based on the p-values of the AUC comparison, the two present fundus-related vessel segmentation approaches perform significantly better than the two previous OCT-based single modal approaches in both the region inside and outside the NCO. In the region outside the NCO, the multimodal approach performs significantly better than the registered-fundus approach and in the region inside the NCO, it presents a similar performance to the registered-fundus approach. The plots of ROC curves for the 19 test eyes are presented in Fig. 7.9.

Two sets of example visual comparison of the four different vessel segmentation

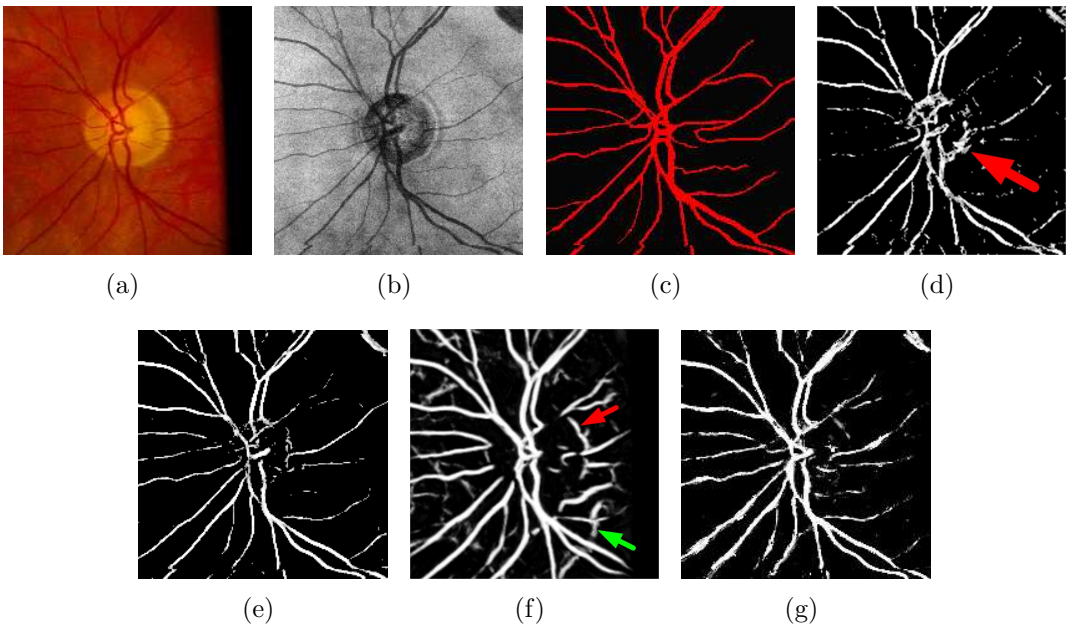

Figure 7.11: Example comparison of the four different vessel segmentation algorithms. (a) Cropped fundus registered image. (b) Vessel-oriented OCT projection image. (c) Ground truth. (d-g) Vessel segmentation from Niemeijer's previous OCT, our previous single modal OCT, registered-fundus, and multimodal approach respectively. The red arrows indicate the false positives or vessel breaks due to the presence of the optic disc/NCO boundary. The green arrow indicates the false positive from the choroidal vessels.

approaches are provided in Fig. 7.10 and 7.11 respectively. As can be seen, both the quantitative and qualitative results of the two present fundus-related approaches demonstrate a great improvement over the two previous single modal OCT-based approaches.

7.6 Discussion and conclusions

We present two novel retinal vessel segmentation approaches, i.e. the registered-fundus and the NCO false-positive-suppression-based multimodal vessel segmentation approach by utilizing the vessel information from fundus photographs with the aim to

obtain a better vessel identification in the SD-OCT volumes. The registered-fundus vessel segmentation segments the vessels from the original fundus photographs and then registers the segmented vessel images to the SD-OCT modality. The multimodal approach simultaneously segments retinal vessels using the complementary information from both SD-OCT volumes and color fundus images. The two fundus-related vessel segmentation approaches perform significantly better than two previous OCT-based single modal approaches in the regions both inside and outside the NCO.

The registered-fundus approach in general provides an accurate vessel segmentation due to the high vessel contrast on fundus photographs. However, it has certain typical limitations, for instance, the typical vessel breaks near the optic disc/NCO as indicated by the red arrows in Fig. 7.10.f and similar optic disc/NCO false positives to Niemeijer's OCT vessel segmentation approach as indicated by the red arrow in Fig. 7.11.f. In addition, it also presents typical false positives from choroidal vessels as indicated by the green arrow in Fig. 7.11.f. Such limitations are overcome by the multimodal approach for the following reasons. 1) The incorporation of the pre-segmented NCO positional information to both the OCT and fundus pixel features allows the suppression of the false positives near the NCO/optic disc. 2) As the fundus photographs are the projection of the structures in the ONH, the choroidal vessels may present on fundus photographs, although the visibility is relative low compared to the retinal vessels on fundus photographs. However, the vessel-oriented OCT projection images are taken from the layer around the RPE/BM plane in SD-OCT volumes, where the choroidal vessels are not visible. The incorporation of the OCT features could "relatively" suppress the responses from the choroidal vessels. In

addition, the choroidal vessels do not have the same tendency of radially distributed around the center of the NCO as the retinal vessels. The oriented Gabor wavelets could thus suppress their responses.

The presented multimodal algorithm overall performs better than the other three algorithms. However, this approach still has limitations. 1) As can be seen, some segmented vessels present breaks and some small vessels are missing. In this work, for computational efficiency, we only take 9 orientations for the Gabor wavelets. Use of more orientations may result in a higher accuracy. 2) The registration errors of the fundus-to-OCT could mis-guide the classification. For instance, when large misalignment of the two modality images occurs, the classifier may treat a non-overlapped vessel as two vessels. 3) The expert may not have always traced very small vessels they deemed "incomplete", whereas the algorithm would have found portions of these vessels, thus (incorrectly) causing the identification of these regions as false positives.

In conclusion, we present a novel registered-fundus and a novel multimodal vessel segmentation approach to help obtain better vessel profiles in the SD-OCT volumes. Overall, the two present fundus-related approaches perform better than two closest previous OCT-based vessel segmentation approaches. The multimodal approach performs better than all the three single modal vessel segmentation approaches of the registered-fundus and the two OCT-based approaches quantitatively and qualitatively.

CHAPTER 8
CONCLUSIONS AND FUTURE DIRECTIONS

8.1 Discussion and conclusions

In this Ph.D. project, overall, a multimodal 3-D scale-learning-based framework is developed to iteratively identify the neural canal opening (NCO) and retinal vessels in spectral-domain optical coherence tomography (SD-OCT) volumes by incorporating the pre-identified NCO locational information to the vessel classification and vessel positional information to the cost function of graph searching of the NCO based on their mutual positional relationship. Recall that four specific aims are included this project and we conclude this project based on the four aims in the following paragraphs.

Aim 1: In aim 1, a NCO segmentation approach using a graph theoretic approach with the application in SD-OCT volumes of human eyes is developed and validated. In most eyes, the algorithm parameters correlate well with the RS parameters from manual planimetry. However, a small discrepancy exists between the NCO and the clinical disc margin in some eyes, as expected. Based on the reproducibility analysis, the algorithm segmentation is robust across repeated visits.

Aim 2: In aim 2, a 3-D wavelet-transform-learning-based graph theoretic approach for segmenting the NCO by iteratively using the pre-identified NCO and vessel positional information (from aim 3 or 4) with the application in SD-OCT volumes of non-human primate eyes is developed and validated. The developed algorithm is validated by comparing the segmented 3-D NCO points with the manual delineation directly from the SD-OCT volumes. Both the quantitative and visual results

demonstrate a great agreement between the automated segmentation and the manual delineation.

Aim 3: In aim 3, a single modal classification approach for identifying retinal vessels in SD-OCT volumes by incorporating the pre-segmented NCO positional information to the vessel classification to suppress the NCO false positives is developed and validated. Compared to a closest previous work of OCT vessel segmentation approach without the incorporation of the NCO positional information, the algorithm presents an obvious improvement.

Aim 4: In aim 4, a NCO-false-positive-suppression-based multimodal concurrent classification and a registered-fundus approach for better identifying retinal vessels in SD-OCT volumes using additional fundus information are developed and validated. The multimodal approach classifies the vessels utilizing the combined complementary features from SD-OCT volumes and color fundus photographs, such as the 3-D retinal layer information, better NCO contrast from the 3-D SD-OCT modality, and better vessel contrast inside the NCO from fundus photographs. The registered-fundus approach segments vessels on original fundus images and registers the segmented vessels to SD-OCT modality. Based on the ROC analysis, the present registered-fundus and multimodal vessel segmentation approaches both perform significantly better than two previous closest OCT-based vessel segmentation approaches (including that from aim 3). The multimodal approach overall performs better than the registered-fundus and the other two OCT-based approaches.

Note that aim 1 presents an initial NCO segmentation using a graph theoretic approach based on the edge cost function. While aim 2 presents an enhanced 3-D

retinal layer and NCO segmentation approach using the lifting-scheme-based wavelet transform tuned by the genetic algorithm by specifically minimizing the distance of the segmented multiple layers and manual tracings at the RPE/BM complex and further extends the 3-D graph-based multiple layer segmentation with the use of scale-learning-based cost function.

Aim 3 presents a NCO false-positive-suppression-based single modal OCT vessel classification approach by incorporating the pre-segmented NCO positional information to the vessel classification. In aim 4, the NCO false-positive-suppression-based single modal OCT vessel classification is further extended to use the additional fundus vessel information. Especially note that the multimodal vessel segmentation approach provides a scheme to utilize the combined complementary features from SD-OCT volumes and color fundus photographs, such as the 3-D retinal layer information, better NCO contrast from the 3-D SD-OCT modality, and better vessel contrast inside the NCO from fundus photographs.

In addition, in aim 3, the pre-segmented NCO positional information is incorporated into the vessel classification for suppressing the false positive tendency near the NCO boundary. Such a technique is also applied on aim 4 of the multimodal vessel segmentation. While in aim 2, the pre-segmented vessel positional information is incorporated into the cost function of the graph searching of the NCO to enhance the NCO segmentation. Thus this project provides a scheme for iteratively identifying the structures having mutual positional relationship by incorporating each other's pre-identified positional information.

Although the initial NCO segmentation performed in human eyes is not able to

be evaluated based on the manual tracings directly from SD-OCT volumes, the repeatability analysis indicates the robustness of the algorithm across repeated visits. While the enhanced wavelet-transform-learning-based NCO segmentation is capable to directly compare to the manual delineation from SD-OCT volumes, both the quantitative and visual results demonstrate a great agreement between the automated segmentation and the manual tracings. Due to the constant anatomic structure and stable nature of the NCO, the robust segmentation of the 3-D NCO moves us towards being able to verify our core hypothesis motivating this study that the identification of the NCO will enable more reproducible and objective glaucomatous parameters than what is currently possible from manual planimetry alone.

8.2 Potential future directions

This section provides some potential future directions to help the management of glaucoma.

8.2.1 NCO-based volumetric parameters

As mentioned previously, the identification of the NCO in SD-OCT volumes could help produce a zero reference plane and thus provide a possibility to derive various optic nerve morphometric parameters based on the NCO reference plane. Here we propose two potential volumetric parameters - the "pre-NCO rim volume" and "post-NCO cup volume". Fig. 8.1 is an example illustration of the created NCO reference plane and proposed volumetric computation positions. The 2-D NCO position is obtained from the segmentation described in Chapter 4. The precise locations of the 3-D NCO points are determined by perpendicularly projecting the 2-D NCO

points onto the interpolated surface 3 (Section 4.5.2 of Chapter 4). A least-squares fit was used to fit a plane to the projected 3-D NCO points and this plane was then transformed into a horizontal plane - forming the desired NCO reference plane (Fig. 8.1.a and b). The same transformation was applied to the OCT volume and top internal limiting membrane (ILM) surface and they are thus re-flattened.

The pre-NCO rim volume and post-NCO cup volume were computed based on the horizontal NCO reference plane and the re-flattened top ILM surface. More specifically, the 2-D NCO points were perpendicularly projected to the top ILM surface from the reference plane to find the position where the NCO boundary crossed. The pre-NCO rim volume is the summation of the voxels under the top ILM surface and above the reference plane and the post-NCO cup volume is that above the top ILM surface and under the reference plane (Fig. 8.1.c).

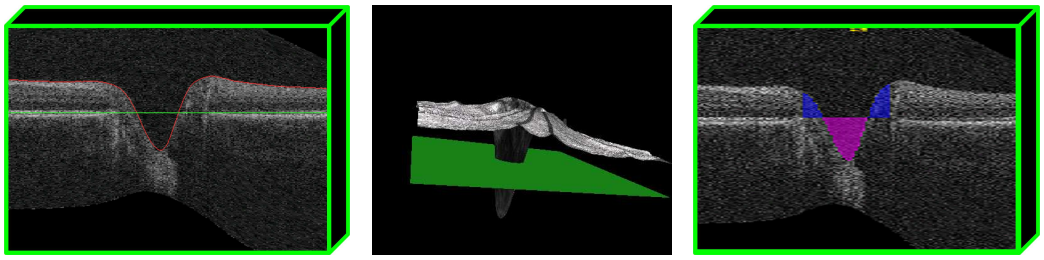

(a) (b) (c)

Figure 8.1: Example illustration of the NCO reference plane and the volumetric computation positions. (a) Reference plane (indicated by the green line) overlapping with a cross-sectional slice of OCT image. (b) 3-D rendering of the reference plane. (c) Pre-NCO rim volume (indicated by the blue color) and post-NCO cup volume (indicated by the magenta color).

Note that the proposed NCO reference plane and volumetric parameters are based on the flattened OCT volumes. Here we just want to address the potential derivation of various optic nerve head (ONH) volumetric parameters based on the identified NCO boundary. A more practical way may consider transforming the 3-D NCO points to the original "tilted" raw OCT space and compute the 3-D parameters in the original space. In addition, the "reference plane" may not necessarily be a flat surface. A fitted surface such as by the thin plate spline based on the 3-D NCO points may be more desirable.

8.2.2 Segmentation of anterior surface of lamina cribrosa

As mentioned in Chapter 2, laminar deformation results in a clinically deeper glaucoma cupping from the damage of the lamina cribrosa, scleral flange, and peripapillary scleral connective tissues. A potential future direction for helping the management of glaucoma is to deal with the deeper glaucoma cupping. An initial investigation could segment the anterior surface of lamina cribrosa (ASLC) in SD-OCT volumes using the graph theoretic approach. Fig. 8.2 illustrates a typical central ONH with the highlight of the NCO (yellow arrows), large blood vessel (pink arrow) inside the NCO, and the ASLC (green arrow) in the SD-OCT volume of a glaucomatous human eye. Note that the mutual positional relationship exists among the ASLC, NCO, and blood vessels. Thus the ASLC could be segmented by incorporating the detected NCO and blood vessel locational information to the graph search. More specifically, the lamina cribrosa typically locates in the region under and inside the NCO. The segmented NCO boundary could be used to confine a particular region of interest

(ROI) for the graph searching of the ASLC. As can be seen in Fig. 8.2, a large blood vessel crosses over with the lamina cribrosa, causing the difficulty of the ASLC segmentation. This is not non-typical in the ONH-centered SD-OCT scans because the poles of the lamina cribrosa are the pathway of the blood vessels exiting the eye. This problem could be remedied by incorporating the detected blood vessel positional information to the graph searching of the ASLC.

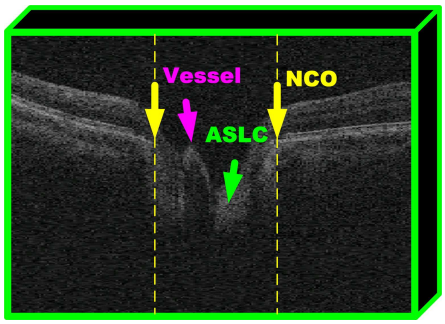

Figure 8.2: Illustration of typical central ONH with highlight of NCO (yellow arrows), large blood vessel inside NCO (pink arrow), and ASLC (green arrow).

Currently both the human and non-human primate SD-OCT volumes we have are acquired using the SD-OCT with the central wavelength at 800 nm range. The ASLC is only visible in a small amount of SD-OCT scans. However, the SD-OCT with higher wavelength centered at 1-1.1 μm could provide deeper penetration of the ONH and would be expected to provide better visibility of the laminar cribrosa. Thus the segmentation of ASLC is promising considering the capability of the high visibility of this structure in the longer wavelength SD-OCT scans.

REFERENCES

[1] S. Resnikoff, D. Pascolini, D. Etyaále, I. Kocur, R. Pararajasegaram, G. P. Pokharel, and S. P. Mariotti, "Global data on visual impairment in the year 2002," *Bulletin of the World Health Organization*, vol. 82, no. 11, pp. 844–851, 2004.

[2] A. J. Bellezza, C. J. Rintalan, H. W. Thompson, J. C. Downs, R. T. Hart, and C. F. Burgoyne, "Deformation of the lamina cribrosa and anterior scleral canal wall in early experimental glaucoma," *Invest. Ophthalmol. Vis. Sci.*, vol. 44, pp. 623–637, 2003.

[3] C. L. Schlamp, Y. Li, J. A. Dietz, K. T. Janssen, and R. W. Nickells, "Progressive ganglion cell loss and optic nerve degeneration in DBA/2J mice is variable and asymmetric," *BMC Neurosci.*, vol. 7, no. 66, 2006.

[4] N. G. Strouthidis, H. Yang, B. Fortune, J. C. Downs, and C. F. Burgoyne, "Detection of the optic nerve head neural canal opening within three-dimensional histomorphometric and spectral domain optical coherence tomography data sets," *Invest. Ophthalmol. Vis. Sci.*, vol. 50, no. 1, pp. 214–223, 2009.

[5] N. G. Strouthidis, H. Yang, J. C. Downs, and C. F. Burgoyne, "Comparison of clinical and three-dimensional histomorphometric optic disc margin anatomy," *Invest. Ophthalmol. Vis. Sci.*, vol. 50, no. 5, pp. 2165–2174, 2009.

[6] J. M. Tielsch, J. Katz, H. A. Quigley, N. R. Miller, and A. Sommer, "Intraobserver and interobserver agreement in measurement of optic disc characteristics," *Ophthalmology*, vol. 95, no. 3, pp. 350–356, 1998.

[7] Y. H. Kwon, M. Adix, M. B. Zimmerman, S. Piette, E. C. Greenlee, W. L. Alward, and M. D. Abràmoff, "Variance owing to observer, repeat imaging, and fundus camera type on cup-to-disc ratio estimates by stereo planimetry," *J. Glaucoma*, vol. 18, no. 4, pp. 305–310, 2009.

[8] W. Drexler and J. G. Fujimoto, "State-of-the-art retinal optical coherence tomography," *Progress Retinal Eye Res.*, vol. 27, no. 1, pp. 45–88, 2008.

[9] G. Quellec, K. Lee, M. Dolejsi, M. K. Garvin, M. D. Abràmoff, and M. Sonka, "Three-dimensional analysis of retinal layer texture: identification of fluid-filled regions in SD-OCT of the macula," *IEEE Trans. Med. Imag.*, vol. 29, no. 6, pp. 1321–1330, 2010.

[10] X. Wu and D. Z. Chen, "Optimal net surface problems with applications," in *Proc. of the 29th International Colloquium on Automata, Languages, and Programming (ICALP)*, ser. LNCS, vol. 2380. Springer-Verlag, 2002, pp. 1029–1042.

[11] K. Li, X. Wu, D. Z. Chen, and M. Sonka, "Optimal surface segmentation in volumetric images – a graph-theoretic approach," *IEEE Trans. Pattern Anal. Machine Intell.*, vol. 28, no. 1, pp. 119–134, 2006.

[12] M. K. Garvin, M. D. Abràmoff, X. Wu, S. R. Russell, T. L. Burns, and M. Sonka, "Automated 3-D intraretinal layer segmentation of macular spectral-domain optical coherence tomography images," *IEEE Trans. Med. Imag.*, vol. 28, no. 9, pp. 1436–1447, 2009.

[13] S. L. Polyak, *The retina*. Chicago: University of Chicago Press, 1941.

[14] R. Bock, J. Meier, L. G. Nyúl, J. Hornegger, and G. Michelson, "Glaucoma risk index: Automated glaucoma detection from color fundus images," *Medical Image Analysis*, vol. 14, pp. 471–481, 2010.

[15] F. D. Nielsen, L. Thrane, J. Black, K. Hsu, A. Bjarklev, and P. E. Andersen, "Swept-wavelength source for optical coherence tomography in the 1um range," in *Proc. of SPIE New Light Sources, Technologies, and Signal Postprocessing: Optical Coherence Tomography and Coherence Techniques II*, vol. 5861, 2005, p. 58610H.

[16] A. Unterhuber, B. Povaẑay, B. Hermann, and H. Sattmann, "In vivo retinal optical coherence tomography at 1040 nm - enhanced penetration into the choroid," *OPTICS EXPRESS*, vol. 13, no. 9, pp. 3252–3258, 2005.

[17] H. Yang, J. C. Downs, A. Bellezza, H. Thompson, and C. F. Burgoyne, "3-D histomorphometry of the normal and early glaucomatous monkey optic nerve head: prelaminar neural tissues and cupping," *Invest. Ophthalmol. Vis. Sci.*, vol. 48, no. 11, pp. 5068–5084, 2007.

[18] A. A. Vlachokosta, P. A. Asvestas, G. K. Matsopoulos, N. Uzunoglu, and T. G. Zeyen, "Preliminary study on the association of vessel diameter variation and glaucoma," in *Proc. of the 29th Annual International Conference of the IEEE EMBS*, 2007, pp. 888–891.

[19] A. Heijl, M. C. Leske, B. Bengtsson, L. Hyman, and M. Hussein, "Reduction of intraocular pressure and glaucoma progression: results from the early manifest glaucoma trial," *Arch. Ophthalmol.*, vol. 120, no. 10, pp. 1268–1279, 2002.

[20] B. Chauhan, T. McCormick, M. Nicolela, and R. LeBlanc, "Optic disc and visual field changes in a prospective longitudinal study of patients with glaucoma: comparison of scanning laser tomography with conventional perimetry and optic disc photography," *Arch. Ophthalmol.*, vol. 119, no. 10, pp. 1492–1499, 2001.

[21] X. Zhu, R. Rangayyan, and A. Ells, "Detection of the optic nerve head in fundus images of the retina using the hough transform for circles," *Digital Imaging*, vol. 23, no. 3, pp. 332–341, 2010.

[22] D. K. Wong, J. Liu, J. H. Lim, X. Jia, F. Yin, H. Li, and T. Y. Wong, "Level-set based automatic cup-to-disc ratio determination using retinal fundus images in ARGALI," in *Proc. of 30th Annual International IEEE Conference On Engineering in Medicine and Biology Society (EMBS 2008)*, 2008, pp. 2266–2269.

[23] H. Li and O. Chutatape, "Boundary detection of optic disk by a modified asm method," *Pattern Recognition*, vol. 36, no. 9, pp. 2093–2104, 2003.

[24] ——, "Automated feature extraction in color retinal images by a model based approach," *IEEE Trans. Biomed. Eng.*, vol. 51, no. 2, pp. 246–254, 2004.

[25] J. Xu, O. Chutatape, E. Sung, C. Zheng, and P. C. T. Kuan, "Optic disk feature extraction via modified deformable model technique for glaucoma analysis," *Pattern Recognition*, vol. 40, no. 7, pp. 2063–2076, 2007.

[26] M. D. Abràmoff, W. L. M. Alward, E. C. Greenlee, L. Shuba, C. Y. Kim, J. H. Fingert, and Y. H. Kwon, "Automated segmentation of the optic disc from stereo color photographs using physiologically plausible features," *Invest. Ophthalmol. Vis. Sci.*, vol. 48, no. 4, pp. 1665–1673, 2007.

[27] M. Merickel, M. D. Abràmoff, M. Sonka, and X. Wu, "Segmentation of the optic nerve head combining pixel classification and graph search," *Proc. of SPIE Medical Imaging: Image Processing*, vol. 6512, p. 651215, 2007.

[28] K. Lee, M. Niemeijer, M. Garvin, Y. Kwon, M. Sonka, and M. Abràmoff, "Segmentation of the optic disc in 3-D OCT scans of the optic nerve head," *IEEE Trans. Med. Imag.*, vol. 29, no. 1, pp. 159–168, 2010.

[29] M. D. Abràmoff, K. Lee, M. Niemeijer, W. L. M. Alward, E. Greenlee, M. Garvin, M. Sonka, and Y. H. Kwon, "Automated segmentation of the cup and rim from spectral domain OCT of the optic nerve head," *Invest. Ophthalmol. Vis. Sci.*, vol. 50, no. 12, pp. 5778–5784, 2009.

[30] Y. Y. Boykov and M. P. Jolly, "Interactive graph cuts for optimal boundary and region segmentation of objects in N-D images," in *Proc. of the Eighth IEEE International Conference on Computer Vision (ICCV)*, vol. 1. IEEE Computer Society, 2001, pp. 105–112.

[31] M. K. Garvin, M. D. Abràmoff, R. Kardon, S. R. Russell, X. Wu, and M. Sonka, "Intraretinal layer segmentation of macular optical coherence tomography images using optimal 3-D graph search," *IEEE Trans. Med. Imag.*, vol. 27, pp. 1495–1505, 2008.

[32] Y. Yin and M. Sonka, "Electric field theory based approach to search-direction line definition in image segmentation: Application to optimal femur-tibia cartilage segmentation in knee-joint 3-D MR," in *Proc. of SPIE Medical Imaging: Image Processing*, vol. 7623, 2010, p. 76230W.

[33] Q. Song, X. Wu, Y. Liu, M. Smith, J. Buatti, and M. Sonka, "Optimal graph search segmentation using arc-weighted graph for simultaneous surface detection of bladder and prostate," in *Proc. of Medical Image Computing and Computer-Assisted Intervention (MICCAI 2009), Part I*, ser. Lecture Notes in Computer Science, vol. 5762. Springer-Verlag, 2009, pp. 827–835.

[34] K. Li, X. Wu, D. Z. Chen, and M. Sonka, "Globally optimal segmentation of interacting surfaces with geometric constraints," *Proc. IEEE CS Conf. Computer Vision and Pattern Recognition (CVPR)*, vol. 1, pp. 394–399, 2004.

[35] Z. Hu, M. Niemeijer, K. Lee, M. D. Abràmoff, M. Sonka, and M. K. Garvin, "Automated segmentation of the optic disc margin in 3-D optical coherence tomography images using a graph-theoretic approach," *Proc. of SPIE Medical Imaging: Biomedical Applications in Molecular, Structural, and Functional Imaging*, vol. 7262, p. 72620U, 2009, oral presentation.

[36] Z. Hu, M. D. Abràmoff, Y. H. Kwon, K. Lee, and M. K. Garvin, "Automated segmentation of neural canal opening and optic cup in 3-D spectral optical coherence tomography volumes of the optic nerve head," *Invest. Ophthalmol. Vis. Sci.*, vol. 51, no. 11, pp. 5708–5717, 2010.

[37] S. R. Nirmala, S. Dandapat, and P. K. Bora, "Wavelet weighted blood vessel distortion measure for retinal images," *Biomedical Signal Processing and Control*, vol. 5, pp. 282–291, 2010.

[38] T. Cour, F. Bénézit, and J. Shi, "Spectral segmentation with multiscale graph decomposition," in *2005 IEEE Computer Society Conference on Computer Vision and Pattern Recognition (CVPR 2005)*, vol. 2, 2005, pp. 1124 –1131.

[39] C. Liu and H. Wechsler, "Gabor feature based classification using the enhanced fisher linear discriminant model for face recognition," *IEEE Trans. Pattern Anal. Machine Intell.*, vol. 11, no. 4, pp. 467–476, 2002.

[40] G. Quellec, M. Lamard, G. Cazuguel, B. Cochener, and C. Roux, "Adaptive non-separable wavelet transform via lifting and its application to content-based image retrieval," *IEEE Trans. Image. Process.*, vol. 19, no. 1, pp. 25–35, 2010.

[41] S. Chaudhuri, S. Chatterjee, N. Katz, M. Nelson, and M. Goldbaum, "Detection of blood vessels in retinal images using two-dimensional matched filters," *IEEE Trans. Med. Imag.*, vol. 8, no. 3, pp. 263–269, 1989.

[42] M. Martínez-Pérez, A. Hughes, A. Stanton, S. Thom, A. Bharath, and K. Parker, "Scale-space analysis for the characterisation of retinal blood vessels," *Proc. of Medical Image Computing and Computer-Assisted Intervention (MICCAI 1999)*, pp. 90–97, 1999.

[43] F. Zana and J. Klein, "Segmentation of vessel-like patterns using mathematical morphology and curvature evaluation," *IEEE Trans. Med. Imag.*, vol. 10, no. 7, pp. 1010–1019, 2001.

[44] X. Jiang and D. Mojon, "Adaptive local thresholding by verification-based multithreshold probing with application to vessel detection in retinal images," *IEEE Trans. Pattern Anal. Machine Intell.*, vol. 25, no. 1, pp. 131–137, 2003.

[45] M. Niemeijer, J. Staal, B. van Ginneken, M. Loog, and M. D. Abràmoff, "Comparative study of retinal vessel segmentation methods on a new publicly available database," in *Proc. of SPIE Medical Imaging: Image Processing*, vol. 5370, 2004, pp. 648–656.

[46] Y. Tolias and S. Panas, "A fuzzy vessel tracking algorithm for retinal images based on fuzzy clustering," *IEEE Trans. Med. Imag.*, vol. 17, pp. 263–273, 1998.

[47] M. Niemeijer, M. D. Abràmoff, and B. van Ginneken, "Image structure clustering for image quality verification of color retina images in diabetic retinopathy screening," *Medical Image Analysis*, vol. 10, pp. 888–898, 2006.

[48] S. Arya, D. Mount, N. Netanyahu, R. Silverman, and A. Wu, "An optimal algorithm for approximate nearest neighbor searching in fixed dimensions," *Journal of the ACM*, vol. 45, no. 6, pp. 891–923, 1998.

[49] H. Wehbe, M. Ruggeri, S. Jiao, G. Gregori, C. A. Puliafito, and W. Zhao, "Automatic retinal blood flow calculation using spectral domain optical coherence tomography," *Optics Express*, vol. 15, no. 23, pp. 15 193–15 206, 2007.

[50] M. Niemeijer, M. K. Garvin, B. van Ginneken, M. Sonka, and M. D. Abràmoff, "Vessel segmentation in 3D spectral OCT scans of the retina," in *Proc. of SPIE Medical Imaging: Image Processing*, vol. 6914, 2008, p. 69141R.

[51] J. Xu, D. A. Tolliver, H. Ishikawa, G. Wollstein, and J. S. Schuman, "3D OCT retinal vessel segmentation based on boosting learning," in *Proc. of the 11th World Congress on Medical Physics and Biomedical Engineering (IFMBE 2009)*, vol. 25. Springer-Verlag, 2009, pp. 244–251.

[52] Z. Hu, M. Niemeijer, M. D. Abràmoff, K. Lee, and M. K. Garvin, "Automated segmentation of 3-D spectral OCT retinal blood vessels by neural canal opening false positive suppression," in *Proc. of Medical Image Computing and Computer-Assisted Intervention (MICCAI 2010), Part III*, ser. Lecture Notes in Computer Science, vol. 6363. Springer-Verlag, 2010, pp. 33–40.

[53] M. Niemeijer, M. K. Garvin, B. van Ginneken, M. Sonka, and M. D. Abràmoff, "Registration of 3D spectral OCT volumes using 3D sift feature point matching," in *Proc. of SPIE Medical Imaging: Image Processing*, vol. 7259, 2009, p. 72591I.

[54] B. H. Menze, K. V. Leemput, D. Lashkari, M. Weber, N. Ayache, and P. Golland, "A generative model for brain tumor segmentation in multi-modal images," in *Proc. of Medical Image Computing and Computer-Assisted Intervention (MICCAI 2010), Part II*, ser. Lecture Notes in Computer Science, vol. 6362. Springer-Verlag, 2010, pp. 151–159.

[55] I. Naqa, D. Yang, A. Apte, D. Khullar, S. Mutic, J. Zheng, J. D. Bradley, P. Grigsby, and J. O. Deasy, "Concurrent multimodality image segmentation by active contours for radiotherapy treatment planning," *Med. Phys.*, vol. 34, no. 12, pp. 4738–4749, 2007.

[56] R. Chrástek, H. Niemann, L. Kubečka, J. Jan, V. Derhartunian, and G. Michelson, "Optic nerve head segmentation in multimodal retinal images," in *Proc. of SPIE Medical Imaging: Image Processing*, vol. 5747, 2005, p. 1604.

[57] Y. Li, N. Hutchings, R. W. Knighton, G. Gregori, B. J. Lujan, and J. G. Flanagan, "Ridge-branch-based blood vessel detection algorithm for multimodal retinal images," in *Proc. of SPIE Medical Imaging: Image Processing*, vol. 7259, 2009, p. 72594K.

[58] Z. Hu, M. Niemeijer, M. D. Abràmoff, and M. K. Garvin, "Automated multi-modality concurrent classification for segmenting vessels in 3-D spectral OCT and color fundus images," in *Proc. of SPIE Medical Imaging: Image Processing*, vol. 7962, 2011, p. 796204, oral presentation.

[59] Z. Hu, Y. H. Kwon, M. D. Abràmoff, K. Lee, and M. K. Garvin, "Repeatability of automated neural canal opening segmentation in SD-OCT images of optic nerve in glaucoma patients," in *Invest Ophthalmol. Vis. Sci.*, 2011, 52:ARVO E-Abstract 1310.

[60] Y. H. Kwon, Y. I. Kim, M. L. Pereira, P. R. Montague, M. B. Zimmerman, and W. L. Alward, "Rate of optic disc cup progression in treated primary open-angle glaucoma," *J. Glaucoma*, vol. 12, pp. 409–416, 2003.

[61] J. C. Downs, H. Yang, C. Girkin, L. Sakata, A. Bellezza, H. Thompson, and C. F. Burgoyne, "Three dimensional histomorphometry of the normal and early glaucomatous monkey optic nerve head: neural canal and subarachnoid space architecture," *Invest. Ophthalmol. Vis. Sci.*, vol. 48, pp. 3195–3208, 2007.

[62] E. Jones, P. Runkle, N. Dasgupta, L. Couchman, and L. Carin, "Genetic algorithm wavelet design for signal classification," *IEEE Trans. Pattern Anal. Machine Intell.*, vol. 23, no. 8, pp. 890–895, 2001.

[63] D. Goldberg, *Genetic algorithms in search, optimization and machine learning.* Boston, MA: Kluwer Academic Publishers, 1989.

[64] Z. Hu, M. Niemeijer, K. Lee, M. D. Abràmoff, M. Sonka, and M. K. Garvin, "Automated segmentation of the optic canal in 3D spectral-domain OCT of the optic nerve head (ONH) using retinal vessel suppression," in *Invest Ophthalmol. Vis. Sci.*, 2009, 50:ARVO E-Abstract 3334.

[65] K. Lee, M. D. Abràmoff, M. Niemeijer, M. K. Garvin, and M. Sonka, "3-D segmentation of retinal blood vessels in spectral-domain OCT volumes of the optic nerve head," in *Proc. of SPIE Medical Imaging: Biomedical Applications in Molecular, Structural, and Functional Imaging*, vol. 7626, 2010, p. 76260V.

[66] M. A. Fischler and R. C. Bolles, "Random sample consensus: a paradigm for model fitting with applications to image analysis and automated cartography," *Commun. Assoc. Comp. Mach.*, vol. 24, pp. 381–95, 1981.

[67] D. G. Lowe, "Distinctive image features from scale-invariant keypoints," *Int. J. Comput. Vision*, vol. 60, no. 2, pp. 99–110, 2004.

[68] E. R. DeLong, D. M. DeLong, and D. L. Clarke-Pearson, "Comparing the areas under two or more correlated receiver operating characteristic curves: a non-parametric approach," *Biometrics*, vol. 44, pp. 837–845, 1988.

[69] X. Robin, N. Turck, A. Hainard, N. Tiberti, F. Lisacek, J. Sanchez, and M. Muller, "pROC: an open-source package for R and S+ to analyze and compare ROC curves," *BMC Bioinformatics*, vol. 12, p. 77, 2011.